INTERNATIONAL JOURNAL OF
IJCOE
COASTAL, OFFSHORE & ENVIRONMENTAL ENGINEERING

Volume 4 | Issue 4 | Nov 2019

www.ijcoe.org **info@ijcoe.org**

www.ijcoe.org

International Journal of Coastal, Offshore and Environmental Engineering (IJCOE)

Vol. 4 / Issue. 4 / Nov 2019

16

International Journal of Coastal, Offshore & Environmental Engineering

Since 2015

ISSN: 2980-8731 (online)

Volume 4 | Issue 4 | Nov 2019

IJCOE

Editor-in-Chief: Prof. Hamid S.Bahai

International Journal of
Coastal, Offshore
& Environmental
Engineering
ISSN: 2980-8731 (online)
Since 2015

In The Name of God

Message from the Editor-in-Chief

The IJCOE journal office was established in 2015,and its first issue was published in 2016. TheIJCOE covers a wide range of research in thefields of oceanography & ocean technology, aswell as marine industries & marine engineering.The editorial board of IJCOE consists of nearly130 of the greatest scientists and researchersfrom over 30 countries worldwide, and thejournal's review board comprises 1,000 membersfrom all five continents. The membership andapplication process for joining the editorial andreview boards of this journal is ongoing. IJCOE isa research-academic quarterly journal that haspublication and distribution permissions fromthe Press Organization and permission topublish scientific-research articles from theMinistry of Science, Research, and Technology(MSRT) with an "A" rating. It also holds a "Q1"rating from the ISC institute with an impactfactor (IF) of approximately 0.43 and isconsidered a "core journal" (prestigious andoutstanding journal). IJCOE is an open-accessjournal and allows the download and receipt ofaccepted articles in full text for free. It respectsand adheres to copyright and COPE regulations.The journal's office operates 24/7, providingservices to researchers. In addition to publishinga regular quarterly journal, IJCOE has 16 specialissues on specific topics in preparation. It alsoprovides conditions for publishing specializedbooks, references, and handbooks. Moreover, itis ready to cooperate with the secretariats ofreputable international conferences to publishtheir selected and outstanding articles. IJCOEevaluates, appraises, and publishes books,articles, and the scientific achievements andfindings of esteemed researchers and scientistsworldwide who are innovating and conductingin-depth research in the "important and strategicfield of the maritime technology & Oceanengineering." It welcomes any form of jointcooperation with universities, research institutes,and related research centers at the national,regional, and international levels, and extends ahand for collaboration.

Classification of Editorial Board in IJCOE

- Editor-in-Chief
- Director-in-Chief
- Deputy Editor
- Executive Managers
- English Text Editor
- Technical Editor
- International Editorial Board
- National Editorial Board
- Editorial Board Associate
- Editorial Board Assistant
- Guest Editorial Board
- Advisory Board
- Administrative Coordinator
- Honorary Board Member
- Methodology Advisor

Author Benefits

- Open Access
- Rapid Publication
- Thorough Peer-Review
- No Copyright Constraints
- Coverage by Leading Indexing Services
- Discounts On Article Processing Charges (APC)
- No Space Constraints, No restriction on the maximum length of the papers, number of figures or colors

Aims of IJCOE

Hydrodynamics

Marine equipment

Structural mechanics

Ocean environmental predictions

Stochastic calculations Experimental

Automatic Control of Marine Systems

Scope of IJCOE

Marine Hazards

Ocean Acoustics

Naval Architecture

Ocean Engineering

Coastal Engineering

Marine Meteorology

Marine Earth Sciences

Underwater Technology

Marine Renewable Energy

Polar & Arctic Engineering

Marine Renewable Energy

Marine Geography & Geodesy

Marine Environmental Engineering

Automatic Control of Marine Systems

Hydro Physics & Physical Oceanography

Type of papers

- Case Studies
- Book Reviews
- Review Article
- Letters to the Editor
- Methodology Papers
- Editorials and Commentaries
- Response or Rejoinder Papers
- Perspective or Opinion Papers
- Conceptual or Theoretical Papers
- Meta-Analysis and Systematic Reviews
- Short Communications or Brief Reports
- Research Articles (Original Research Papers)

Scientific Research Journal

Ministry of Science, Research And Technology (MSRT)

Jurnal Ranking 2023: A

Ministry Of Science, Research And Technology (ISC)

Citation Impact 2022: 0.429

Quartile 2022 : Q1

Core Collection

IJCOE is a Member of

We Respect the Science CIVILICA	Google Scholar	Jouroscope
COPE 20TH ANNIVERSARY 1997-2017 cc BY NC SA	ISC	JREF.IR Journals Reference
DOAJ DIRECTORY OF OPEN ACCESS JOURNALS	ISSN INTERNATIONAL STANDARD SERIAL NUMBER INTERNATIONAL CENTRE	Researcher.Life
doi Crossref EScience Press mEDRA	iThenticate	magiran
OPEN ACCESS	pistotn	RG ResearchGate
Regional Information Center for Science and Technology RICEST	ScienceGate	Scilit
SID	website.informer.com	WEBrate

Cantact Us

Office 1 | Research Institute of Meteorology and Atmospheric Science

Address | Tehran, Shahid Kharrazi Highway, Pajoohesh Blvd, Research Institute of Meteorology and Atmospheric Science, Sand and Dust Storm International Research Center (SDS-IRC), No. 13, 1st floor.

Phone | +982144787652

Postal code | 13611-14977

website | www.rimac.ac.ir

Office 2 | Iranian National Institute for Oceanography and Atmospheric Science

Address | Tehran, Dr. Fatemi Gharbi St., Shahid Etemadzade St., No. 3, third floor.

Phone | +982166944873

Postal code | 13389 – 14118

website | www.inio.ac.ir

Email | Info@ijcoe.org

Website | www.ijcoe.org

Follow Us

www.ijcoe.org

INTERNATIONAL JOURNAL OF
IJCOE
COASTAL, OFFSHORE & ENVIRONMENTAL ENGINEERING

Volume & Issue:

Volume 4, Issue 4, November 2019

Number of Articles: 6

Content

INTERNATIONAL JOURNAL OF
COASTAL & OFFSHORE ENGINEERING

IJCOE Vol.4/No. 4/ Winter 2019 (1-8)

Available online at: http://ijcoe.org/browse.php?a_code=A-10-233-1&sid=1&slc_lang=en

Numerical Validation of Experimental Tests Conducted on a Fixed Offshore Oscillating Water Column

Milad Zabihi[1], Said Mazaheri[2*], Masoud Montazeri Namin[3]

[1] *Ph.D student, Iranian National Institute for Oceanography and Atmospheric Science; milad.zabihi@inio.ac.ir*
[2*] *A/Professor, Iranian National Institute for Oceanography and Atmospheric Science; said.mazaheri@inio.ac.ir*
[3] *Assistant Professor, University of Tehran; mnamin@ut.ac.ir*

ARTICLE INFO

Article History:
Received: 18 Sep. 2018
Accepted: 16 Feb. 2019

Keywords:
OWC
Numerical Simulation
Wave Energy
CFD
Experimental

ABSTRACT

Supplying world future energy is tied with renewable energies and wave energy is one of the biggest resources of renewable energy which is somehow untapped. Oscillating Water Column (OWC), one of the most familiar devices in harnessing wave energy, is still not being properly commercialized due to the complicated hydrodynamic behavior. Offshore OWCs are exposed to higher wave energy; however, the researches on this kind of OWCs is limited. Hence, in this paper, a fully nonlinear two phase flow model of a fixed offshore OWC is developed using Ansys Fluent. Unlike the previous studies, the developed numerical model has the merit of being validated against a relatively large scale physical model (1:15). The results of the model are compared by those obtained in experimental campaign conducted by the authors. Results of both free surface elevation and air pressure in the OWC chamber are compared. Generally, the results showed an admissible accordance between numerical and experimental model. Some discrepancies could be detected in the free surface elevation in the chamber especially for short wave period. This can be attributed to the increase of nonlinear effects in the chamber by increase of wave steepness. The developed model can be applied for further researches on OWCs such as optimization or improving OWC performance.

1. Introduction

Undoubtedly, supplying increasing energy demand is one of the biggest challenges in today's world. On the other hand, energies based on carbon emission will be finished soon in addition to their destructive impacts on our environment. Hence, renewable energy resources such as wind, solar, tidal and wave are non-pollutant appropriate options for replacement. Among different renewable energy resources, wave energy is an untapped resource which has the merit of relatively high energy density [1]. Of the numerous devices developed for harnessing wave energy [2], one that particularly stands out is Oscillating Water Column (OWC). An OWC consists of a partially submerged compartment which is open to sea at the bottom. Incident wave interaction with the compartment induces water fluctuation inside the chamber. The water fluctuation causes the air pressure in the chamber to be compressed or depressurized. Air flow generated by this mechanism can drive a turbine installed to the chamber and then using a generator electricity will be produced.

The OWCs can be constructed nearshore or offshore [3]. Offshore OWCs which are exposed to higher wave energy [4] and consequently result in higher energy capture. A lot of numerical and experimental researches have been conducted on OWCs in recent years. Numerical models developed for assessing the OWC performance can be classified into two main groups. The first are those studies based on potential flow theory which include the works done by [5]–[8]. Evans [5] considered the free surface fluctuation in the chamber as a rigid piston which is almost a sound assumption particularly for the cases with large ratios of wavelength to chamber width. Then, [6]–[9] upgraded the rigid piston model by introducing periodic surface pressure distribution and considering free surface curvature. Later, researchers used boundary element method to solve rigid piston model or models based on surface pressure distribution [10], [11]. Although computational cost for potential flow theory is not high, it has demerits such as having no capability in taking nonlinear interaction in to account. Hence, applying CFD approaches based on solving Navier-Stokes equation for considering nonlinear interactions such as wave breaking or sloshing in the chamber is the second approach toward numerical simulation of OWCs. Given the ongoing progress in CFD models and computers' process ability, it seems that CFD is the most appropriate tool for modeling WECs such as OWCs. A number of efforts have been performed to model OWCs using numerical wave tank (NWT) and applying Navier-Stokes equation. Iturrioz et al. [12] used Open Foam incompressible two phase flow to model OWC-wave interaction. Vyzikas et al. [13] and Simonetti et al. [14], [15] also applied Open Foam and validated their two dimensional incompressible model against their experimental data. Reef3D was another code developed for OWC simulation by Kamath et al. [16]. They validated their model against bottom standing OWC experiments conducted by Morris Thomas et al. [17].

Lou et al. [18] performed a nonlinear analysis on the efficiency of fixed OWC for fully nonlinear waves using Ansys Fluent. The key result of that research was a substantial decrease in the hydrodynamic efficiency of the OWC device with increasing wave height. Anbarsooz et al. [19] conducted such a similar study and evaluated steep wave effects on the performance of a fixed OWC using Ansys Fluent.

Very recently, Elhanafi et al. [20]–[23] did a thorough job on both bottom fixed and bottom detached OWCs. They used Star-CCM+ to develop their CFD models. They evaluated energy balance in offshore [24] and onshore OWCs [25] and investigated the effects of asymmetric back and forth walls on efficiency of the offshore OWCs [20].

Although a lot of studies have been conducted on OWCs, there are steps toward commercializing the device perhaps due to the complicated hydrodynamic behavior of an OWC. Numerical models are great tools to bridge this gap as they need much less budget. The literature review indicates that a huge part of the previous studies is devoted to onshore or shore-based OWCs and less work has been done on offshore OWCs. Hence the aim of this paper is to validate the fully nonlinear model for an offshore OWC-wave interaction. Without validation it is impossible to assess the model accuracy and suitability. Unfortunately, accessibility to experimental data in the current issue is hard due to the limited experimental tests. Therefore, for validation of the current model, experimental tests performed by the authors have been used. It should be mentioned that the tests have the advantage of being relatively large scale experiments (Scale 1:15).

The rest of the paper can be summarized as follows; in section 2 a description of the experimental tests which have been used for validation is presented. Section 3 is devoted to numerical simulation where governing equations, boundary conditions and all relevant numerical settings are presented. Section 4 compares the results obtained by numerical procedure with those measured in experimental campaign. Section 5 is a brief summary of the current research which ends up with concluding remarks.

2. Description of the Experiments

Experimental tests were carried out at National Iranian Marine Laboratory (NIMALA), Tehran, Iran. The Laboratory is equipped with a towing tank of 400 m length, 6 m width and 4 m depth. The wave generator system which is a piston type wave maker can be set up to produce both regular and irregular waves. The regular wave height can reach to 50 cm height and 3 s period. The system is capable of generating different types of irregular wave spectra bounded to significant wave height 40 cm and peak period 3 s. At the end of the tank there is a dissipating beach to prevent reflection from the end wall of the tank. Moreover, Due to the long length of the wave tank interference of the reflected wave and incident wave is not a challenge so that the obtained results showed accurate incident wave generation. As stated before, 1:15 scale of a fixed offshore OWC was built using plexiglass material. The thickness of the material used for building OWC was 1cm except for the front wall which was 1.4 cm to decrease the risk of front wall distortion due to the wave action. To keep OWC in its position and to prevent any wave induced movement, a steel holding frame was designed which is shown in Figure 1. As can be seen, the OWC is placed exactly in the middle of the tank in order to minimize the side wall effects.

Figure 1. 3D view of holding frame for keeping OWC in its position [26]

Length, width and height of the OWC is shown in Figure 2. Further details about how OWC device dimensions were determined can be found in Ref. [27]. There are several ways for simulating Power Take Off (PTO) and its relevant damping; however, in this paper, as can be seen in Figure 2, slot shaped aperture is used to simulate PTO damping. For the test series used for validation, slot size (S=0.5 cm) was used. This value was selected according to previous results which showed that aperture ratio (the ratio of slot area to the chamber roof area) of 0.6 to 0.7% performs optimal.

Water depth (d=4 m) and front wall draft (Dr=20 cm) were also kept constant for validation tests. The wave tank longitudinal section is shown in Figure 3. Figure 3 also indicates the locations of the instruments such as Wave Gauges (WG) and Pressure Sensors (PS) installed in the chamber and along the wave tank. All data acquisition processes were performed at 50 Hz. Regular wave was introduced into the wave maker with constant wave height of H=15 cm and three different wave periods including T=1.8, 2 and 2.2 sec.

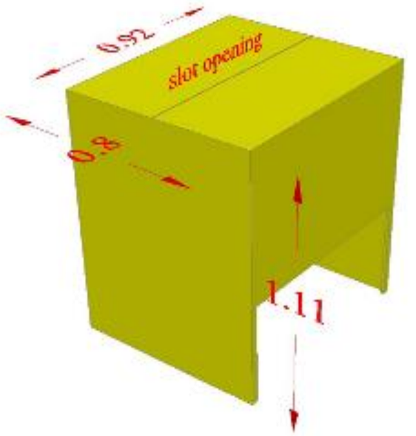

Figure 2. Dimensions of the physical model (meter) [27]

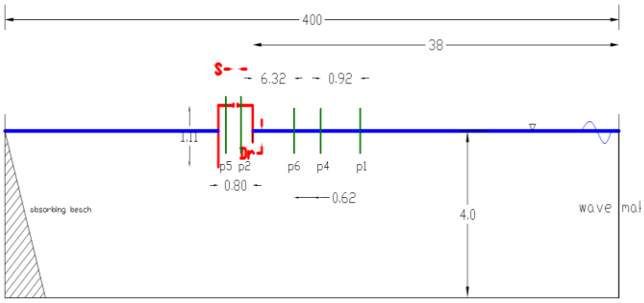

Figure 3. The Locations of the wave gauges and pressure sensors (Not to scale)

3. Numerical Simulation

3.1. Governing Equations

Fully nonlinear model based on Reynolds Averaged Navier Stokes (RANS) equation accompanied by Volume of Fluid (VOF) surface capturing method are the governing equations. Fluent solves Navier-Stokes and Continuity equation. Navier-Stokes equations in three dimensional coordination are as follows;

$$\frac{\partial u}{\partial t}+u\frac{\partial u}{\partial x}+v\frac{\partial u}{\partial y}+w\frac{\partial u}{\partial z}= -\frac{1}{\rho}\frac{\partial p}{\partial x}+g_x+\upsilon\left(\frac{\partial^2 u}{\partial x^2}+\frac{\partial^2 u}{\partial y^2}+\frac{\partial^2 u}{\partial z^2}\right) \tag{1}$$

$$\frac{\partial v}{\partial t}+u\frac{\partial v}{\partial x}+v\frac{\partial v}{\partial y}+w\frac{\partial v}{\partial z}= -\frac{1}{\rho}\frac{\partial p}{\partial y}+g_y+\upsilon\left(\frac{\partial^2 v}{\partial x^2}+\frac{\partial^2 v}{\partial y^2}+\frac{\partial^2 v}{\partial z^2}\right) \tag{2}$$

$$\frac{\partial w}{\partial t}+u\frac{\partial w}{\partial x}+v\frac{\partial w}{\partial y}+w\frac{\partial w}{\partial z}= -\frac{1}{\rho}\frac{\partial p}{\partial z}+g_z+\upsilon\left(\frac{\partial^2 w}{\partial x^2}+\frac{\partial^2 w}{\partial y^2}+\frac{\partial^2 w}{\partial z^2}\right) \tag{3}$$

where, u, v and w are components of velocity field in x, y and z direction, respectively. P is the pressure and ρ is density. υ is the kinematic viscosity and g_x, g_y and g_z are the gravitational acceleration components. However, assuming z is in gravity direction, g_x and g_y are equal to zero and g_z will be equal to $-g$.

Eq. (4) presents the continuity equation and Eq. (5) shows the continuity equation for incompressible flow.

$$\frac{\partial}{\partial x}(\rho u)+\frac{\partial}{\partial y}(\rho v)+\frac{\partial}{\partial z}(\rho w)+\frac{\partial \rho}{\partial t}=0 \tag{4}$$

$$\frac{\partial u}{\partial x}+\frac{\partial v}{\partial y}+\frac{\partial w}{\partial z}=0 \tag{5}$$

All parameters have been introduced following the Navier-Stokes equation.

As in this study it is focused on wave generation and its interaction with OWC, consequently free surface capture is an indispensable part of this study. Hence, for free surface tracking VoF method has been used. Hirt [28] developed the VOF method to solve the two-phase problem. The VOF formulation is based on the fact that two or more phases are immiscible. In each control volume, sum of the volume fraction of all phases is unit (Eq. (6)). If the qth fluid volume fraction is recognized as α_q, then depending on α_q value the following three conditions are possible: $\alpha_q=0$ shows that the volume is empty of qth fluid, $\alpha_q=1$ shows that the volume is full of qth fluid and any other value between 0 and 1 shows the interface. The volume fraction is as follows;

$$\sum_{q=1}^{n}\alpha_q=1 \tag{6}$$

$$\frac{\partial}{\partial t}(\alpha_q)+\nabla.(\alpha_q\overrightarrow{v_q})=0 \tag{7}$$

where $\vec{v}_q$ is velocity vector.

3.2. Computational Fluid Domain and Boundary Conditions

The most important part of wave structure hydrodynamic study is to generate accurate waves. Simulation of a Numerical Wave Tank (NWT) is explained in this section (See Figure 4). The fluid domain of the numerical wave tank is of 50 meter length equal to approximately 8L (L= wavelength). One wave length at the far end of the NWT is devoted to damping zone to prevent unwanted reflection from outlet boundary.

For numerical wave generation, one may simulate wave paddle as a moving boundary and introduce the motion of the wave to the wave paddle. As this method involves dynamic mesh and needs remeshing in each time step, it may need much more efforts. However, Ansys Fluent has the capability to generate waves with a built-in function via velocity inlet wave boundary condition. No slip wall boundary condition is assigned to the bottom of the NWT. Other NWT boundary conditions include applying atmospheric pressure to the boundary which is above still water level and assigning an outlet condition to the NWT right hand boundary (See Figure 4).

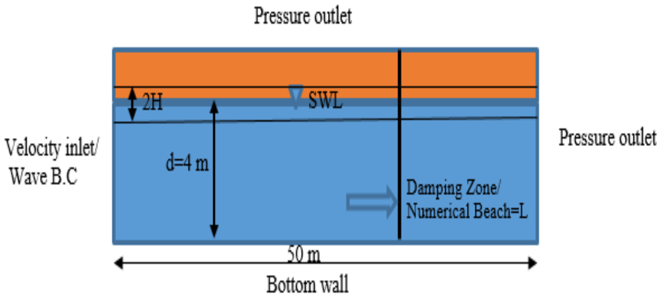

Figure 4. Schematic of the numerical wave tank

To capture wave propagation accurately, 3 types of mesh discretization has been applied for NWT developing. They are presented in Table 1. It should be noted that x is in the wave propagation direction while z is in the wave height direction. "H" stands for wave height and a zone equal to 2H has been refined for tracking wave height (Figure 4). Outside the wave propagation zone (2H), the grids are coarser. For grids in z direction, bias growth rate 1.2 was used meaning that each cell is 1.2 times bigger than its neighbor cell in z direction. This procedure was replicated for damping zone to help the wave dissipation more.

Time step size T/1000 to T/400 (T is wave period) leads to proper results according to previous studies recommendations [29]. Ansys Fluent allows any manipulation in time step size during simulation. Considering this feature, no significant change in wave generation results was observed by applying different time step sizes (in the aforementioned range). Hence, time step T/400 was selected for the following simulations.

Table 1. Three different mesh types discretization

Mesh Type	Delta x	Delta z
1	L/20	H/10
2	L/30	H/15
3	L/40	H/20

3.3. Numerical Settings in Ansys Fluent and NWT Result

For solving the governing aforementioned equations, the following numerical settings were applied. Considering pressure based solver, PISO scheme was applied for decoupling pressure velocity coupling. The spatial derivatives in the momentum equations were discretized using a second order upwind scheme and also a second order implicit formulation was applied for the time-derivatives. For VOF schemes, fluent presents two scheme called Modified-Hric and Compressive. According to Ansys Fluent user guide, Compressive scheme captures free surface more accurate. Hence, Compressive scheme was applied in this paper. The pressure interpolation method was based on PRESTO (PRE Staggering Option) scheme which is a widely used scheme for free surface modeling and wave generation models. The two equation turbulence model of k-w SST was applied to close the RANS equation.

The result of simulated wave propagation for a case with 15cm wave height and 2s period was compared against what was obtained from stokes second order wave theory (Figure 5). It should be mentioned that t/T is a dimensionless parameter showing the ratio of simulation time to the incident wave period. Although all of the tested mesh types yielded good results, the results showed that Mesh type 3 yields more accurate wave height with less than 0.04% error. Hence, Mesh type 3 is selected for the wave-OWC interaction in the following section.

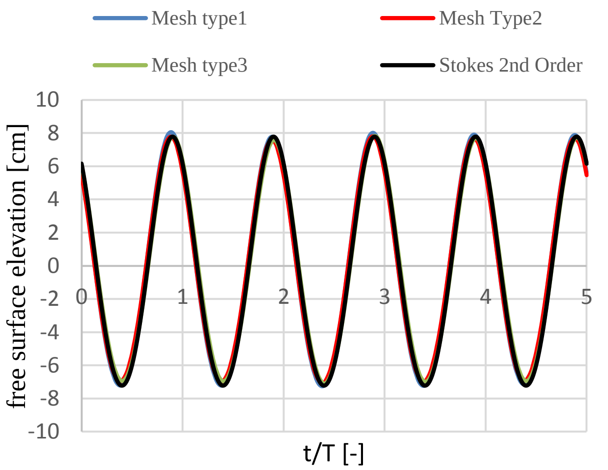

Figure 5. free surface elevation against nondimensional time; comparing three different discretization and Stokes 2nd order theory

4. Numerical Validation for an Offshore OWC

4.1. Model set up

In this section, the NWT model simulated in the previous section was developed for OWC-wave interaction. It is worth mentioning that all previous numerical settings were applied for this section. The mesh used for OWC-wave interaction is shown in Figure 6. The free surface mesh type was the same as mesh type 3.

The OWC position was according to Figure 1. However it should be noted that for reducing simulation run, half width of the OWC structure was considered by applying symmetry boundary condition. Moreover, in laboratory the distance between the OWC model and side walls was 2.54 but in the current numerical model this was decreased to 1m for lowering the computation time.

The mesh size around the OWC structure was 0.01m and it was considered to be 0.0025m in the slot aperture. NWT in y direction was divided to six elements.

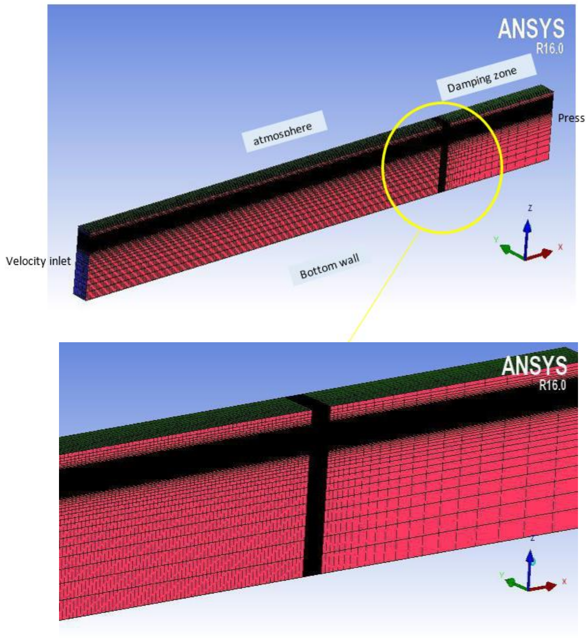

Figure 6. Mesh and boundary conditions used for OWC wave interaction; mesh refinement in free surface area and OWC position

4.2. Comparing numerical and experimental results

In this section the numerical results are compared with those observed in experiments. Wave height was kept constant at H=15 cm and three different values were considered for wave period (T=1.8, 2 and 2.2 s).

In the first step, the results are presented for free surface elevation outside the chamber (See Figure 7-9). It should be noted that the results are presented for 5 wave cycles. The numerical results are in good agreement for the three probes located outside the chamber ensuring there is no unwanted reflection in numerical domain regardless of reducing the numerical tank width and length relative to experimental wave tank.

To evaluate the performance of numerical wave dissipation, the result of free surface elevation at the far end of the tank; that is to say x=50m, is presented in Figure 10. As it is clear, water depth fluctuation at simulation time greater than 2s is around 0.5cm which is a negligible value ensuring appropriate function of the dissipation zone.

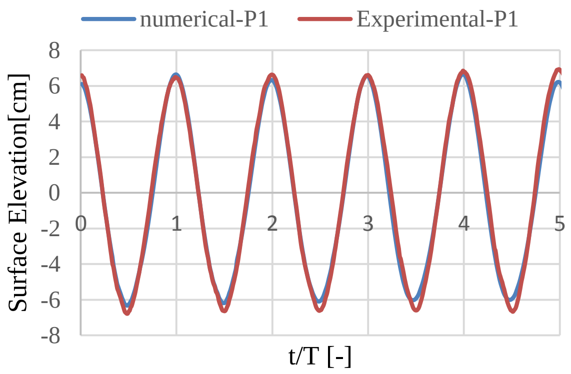

Figure 7. Free surface elevation at probe 1; numerical values versus experimental measurements (H=15 cm, T=2 s)

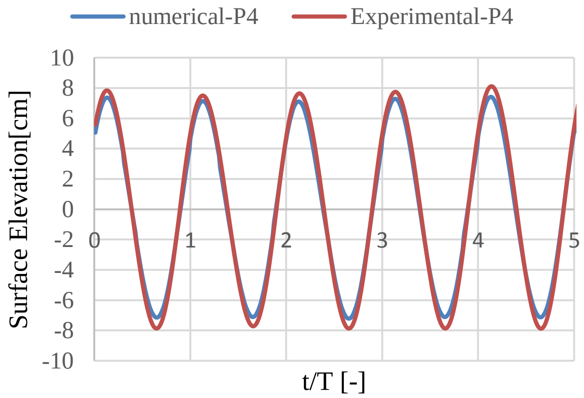

Figure 8. Free surface elevation at probe 4; numerical values versus experimental measurements (H=15 cm, T=2 s)

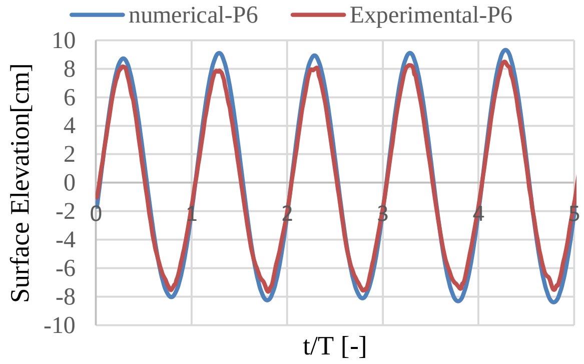

Figure 9. Free surface elevation at probe 6; numerical values versus experimental measurements (H=15 cm, T=2 s)

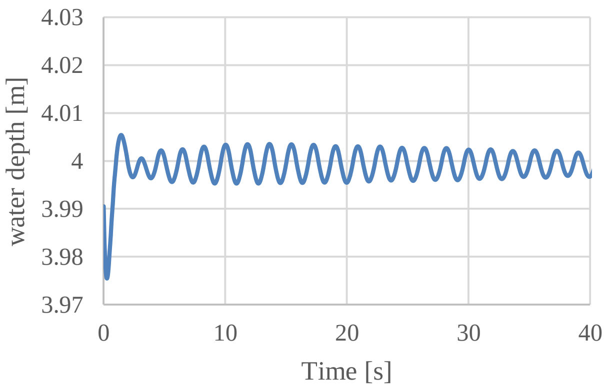

Figure 10. Numerical free surface elevation at x=50m

The numerical results corresponding to probes inside the chamber (P2 and P5) were compared with experimental measurements through Figure 11-12. Unlike the outside probes, for inside probes (P2 and P5) nonlinear interaction is more visible. Although there are some discrepancies especially for P2 at wave troughs, the numerical model could capture the nonlinearity in a good way.

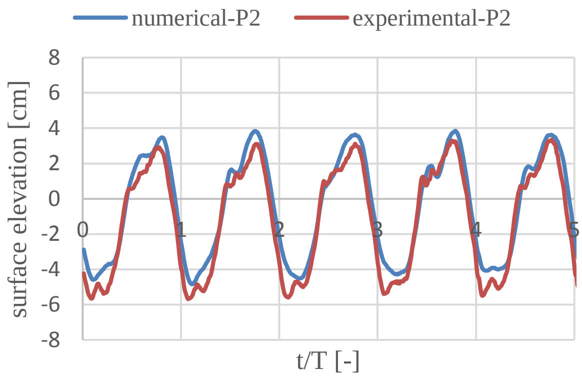

Figure 11. Free surface elevation at probe 2; numerical values versus experimental measurements (H=15 cm, T=2 s)

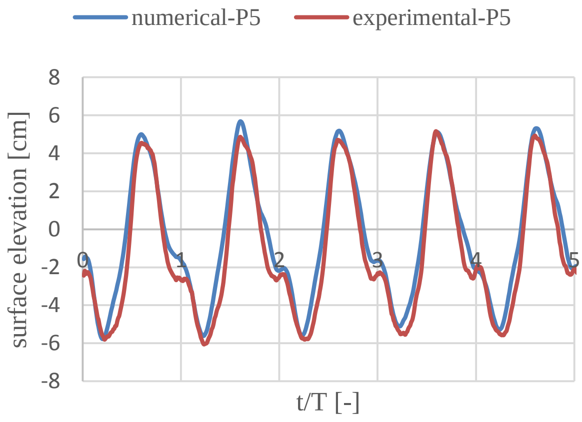

Figure 12. Free surface elevation at probe 5; numerical values versus experimental measurements (H=15 cm, T=2 s)

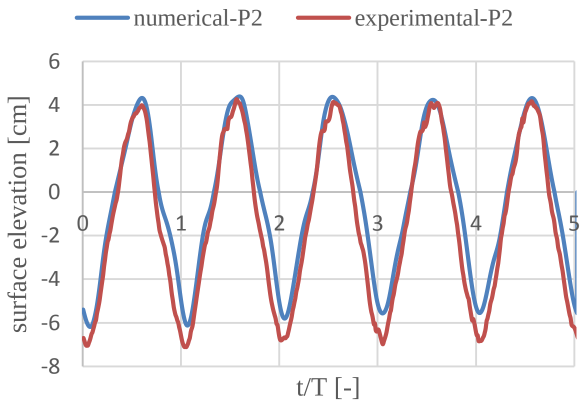

Figure 13. Free surface elevation at probe 2; numerical values versus experimental measurements (H=15 cm, T=2.2 s)

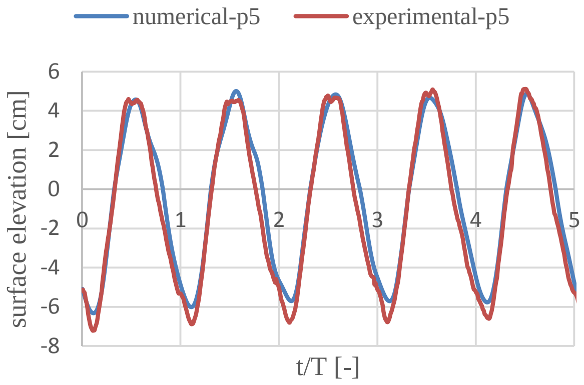

Figure 14. Free surface elevation at probe 5; numerical values versus experimental measurements (H=15 cm, T=2.2 s)

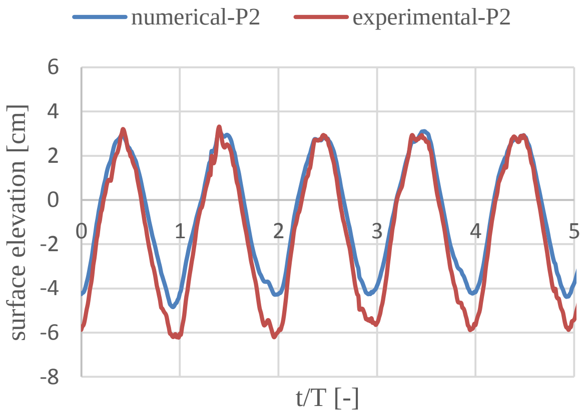

Figure 15. Free surface elevation at probe 2; numerical values versus experimental measurements (H=15 cm, T=1.8 s)

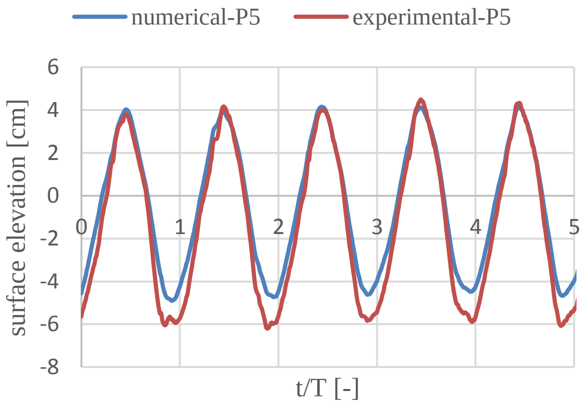

Figure 16. Free surface elevation at probe 5; numerical values versus experimental measurements (H=15 cm, T=1.8 s)

The aforementioned procedure was replicated for T=2.2s and T=1.8s. For abridgment, the results of the waves outside the chamber are not presented for T=1.8s and T=2.2s and just the inner chamber fluctuations are presented through Figure 13-16. As it is obvious, the results are in better agreement with experimental measurements for T=2.2s rather than T=1.8. This can be attributed to the higher wave steepness caused by lower wave period which consequently resulted in higher nonlinearity. Considering authors visual observation, this nonlinear interaction is mainly caused by sloshing phenomenon. In fact, short period waves entering OWC may reflect from the chamber rear wall and interact with incoming wave at a location in the middle of the chamber. This will prevent free surface elevation in the chamber to have a piston shape fluctuation.

Chamber air pressure was another parameter evaluated in this paper as it is crucial to determine the chamber pressure to assess the OWC efficiency. The results of air pressure are presented in Figure 17 and 18. Admissible agreement can be detected between numerical results and experimental measurements. Although there are discrepancies in minimum and maximum pressure occurred in the chamber, the general pattern was captured by developed numerical model.

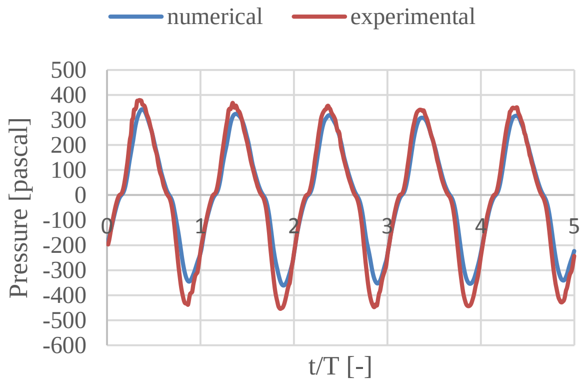

Figure 17. Chamber air pressure (T=1.8 s)

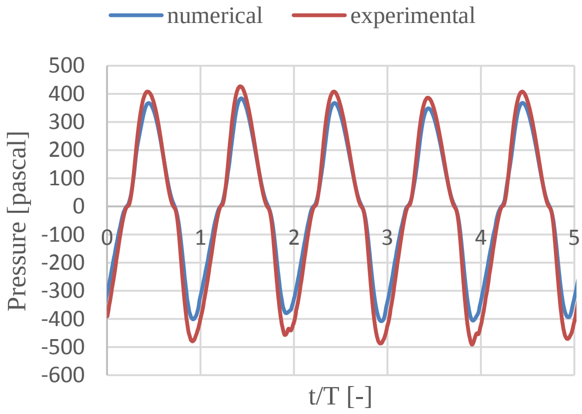

Figure. 18 Chamber air pressure (T=2.2 s)

5. Summary and Conclusions

OWC is one of the wave energy devices even attained full scale prototype but not fully commercialized yet. Surely, its performance should be optimized prior to commercializing the device and this needs further numerical and experimental researches. In this paper, a numerical model was developed using Ansys Fluent based on fully nonlinear two phase flow model. The free surface fluctuation outside and inside the chamber as well as air pressure inside that were compared with experimental results obtained by the authors, very recently. Generally, numerical results showed good accordance with experimental data especially for long waves (T=2 and 2.2 s) when the ratio of wave length to chamber length was large enough to act as a piston type oscillation. For short period wave; highly steep wave, some discrepancies between numerical and experimental results were observed inside the chamber. The developed model can be employed for further analyzes such as optimization of the OWC performance.

6. References

1- Khan, N., Kalair, A., Abas, N. and Haider, A., (2017), *Review of ocean tidal, wave and thermal energy technologies*, Renewable and Sustainable Energy Reviews. Vol.72, p.590–604. https://doi.org/10.1016/j.rser.2017.01.079

2- López, I., Andreu, J., Ceballos, S., Martínez de Alegría, I. and Kortabarria, I., (2013), *Review of wave energy technologies and the necessary power-equipment*. Renewable and Sustainable Energy Reviews, Vol.27, p.413–434. https://doi.org/10.1016/J.RSER.2013.07.009

3- Falcão, A.F.O. and Henriques, J.C.C., (2016), *Oscillating-water-column wave energy converters and air turbines: A review*. Renewable Energy, Vol.85, p.1391–1424. https://doi.org/10.1016/J.RENENE.2015.07.086

4- Ashlin, S.J., Sundar, V. and Sannasiraj, S.A., (2016), *Effects of bottom profile of an oscillating water column device on its hydrodynamic characteristics*. Renewable Energy, Elsevier. Vol. 96, p.341–353.

5- Evans, D. V., (1978), *The oscillating water column wave energy device*. Journal Inst Maths Applics, Vol. 22, p.423–433.

6- Falcão, A.F. de O. and Sarmento, A., (1980), *Wave generation by a periodic surface pressure and its application in wave-energy extraction*. 15th International Congress of Theoritical and Applied Mechanics,.

7- Falnes, J. and McIver, P., (1985), *Surface wave interactions with systems of oscillating bodies and pressure distributions*. Applied Ocean Research, Vol.7 (4), p.225–234. https://doi.org/10.1016/0141-1187(85)90029-X

8- Sarmento, A.J.N.A. and De Falcao, A.F.O., (1985), *Wave generation by an oscillating surface-pressure and its applications in wave energy extraction*. Journal of Fluid Mechanics, Vol.150, p.467–485. https://doi.org/10.1017/S0022112085000234

9- Evans, D., (1982), *Wave power absorption by systems of oscillating surface pressure distributions*. Journal of Fluid Mechanics, Vol.114, p.481–499.

10- Brito-Melo, A., Sarmento, A.J.N. a., Clement, A.H. and Delhommeau, G., (1999), *A 3D boundary element code for the analysis of OWC wave-power plants*. Proceedings of the 1999 Ninth International Offshore and Polar Engineering Conference (Volume 1), Brest, France, 30 May - 4 June 1999, Vol.I, p.188–195.

11- Delauré, Y. and Lewis, A., (2003), *3D* *hydrodynamic modelling of fixed oscillating water column wave power plant by a boundary element methods*. Ocean Engineering, Vol.30, p.309–330. https://doi.org/10.1016/S0029-8018(02)00032-X

12- Iturrioz, A., Guanche, R., Lara, J.L., Vidal, C. and Losada, I.J., (2015), *Validation of OpenFOAM® for Oscillating Water Column three-dimensional modeling*. Ocean Engineering, Vol.107, p.222–236. https://doi.org/10.1016/j.oceaneng.2015.07.051

13- Vyzikas, T., Deshoulières, S., Giroux, O., Barton, M. and Greaves, D., (2017), *Numerical study of fixed Oscillating Water Column with RANS-type two-phase CFD model*. Renewable Energy, Vol.102, p.294–305. https://doi.org/10.1016/j.renene.2016.10.044

14- Simonetti, I., Cappietti, L., Elsafti, H. and Oumeraci, H., (2017), *Optimization of the geometry and the turbine induced damping for fixed detached and asymmetric OWC devices: A numerical study*. Energy, Elsevier B.V. Vol.139, p.1197–1209. https://doi.org/10.1016/j.energy.2017.08.033

15- Simonetti, I., Cappietti, L., Elsafti, H. and Oumeraci, H., (2018), *Evaluation of air compressibility effects on the performance of fixed OWC wave energy converters using CFD modelling*. Renewable Energy, Elsevier B.V. Vol.119, p.741–753. https://doi.org/10.1016/j.renene.2017.12.027

16- Kamath, A., Bihs, H. and Arntsen, Ø.A., (2015), *Numerical investigations of the hydrodynamics of an oscillating water column device*. Ocean Engineering, Vol.102, p.40–50. https://doi.org/10.1016/j.oceaneng.2015.04.043

17- Morris-Thomas, M.T., Irvin, R.J. and Thiagarajan, K.P., (2007), *An Investigation Into the Hydrodynamic Efficiency of an Oscillating Water Column*. Journal of Offshore Mechanics and Arctic Engineering, Vol.129(4), p.273. https://doi.org/10.1115/1.2426992

18- Luo, Y., Nader, J.-R., Cooper, P. and Zhu, S.-P., (2014), *Nonlinear 2D analysis of the efficiency of fixed Oscillating Water Column wave energy converters*. Renewable Energy, Vol.64, p.255–265. https://doi.org/10.1016/J.RENENE.2013.11.007

19- Anbarsooz, M., Faramarzi, A. and Ghasemi, A., (2016), *A numerical study on the performance of fixed oscillating water column wave energy converter at steep waves*. ASME 2016 Power Conference Collocated with the ASME 2016 10th International Conference on Energy Sustainability and the ASME 2016 14th International Conference on Fuel Cell Science, Engineering and Technology.

20- Elhanafi, A., Fleming, A., Macfarlane, G. and Leong, Z., (2017), *Underwater geometrical impact on the hydrodynamic performance of an offshore oscillating water column–wave energy converter*. Renewable Energy, Elsevier Ltd. Vol.105, p.209–231. https://doi.org/10.1016/j.renene.2016.12.039

21- Elhanafi, A., Macfarlane, G., Fleming, A. and Leong, Z., (2017), *Investigations on 3D effects and correlation between wave height and lip submergence of an offshore stationary OWC wave energy converter*. Applied Ocean Research, Elsevier B.V. Vol.64, p.203–216. https://doi.org/10.1016/j.apor.2017.03.002

22- Elhanafi, A., Macfarlane, G., Fleming, A. and Leong, Z., (2017), *Scaling and air compressibility effects on a three-dimensional offshore stationary OWC wave energy converter*. Applied Energy, Elsevier Ltd. Vol.189, p.1–20. https://doi.org/10.1016/j.apenergy.2016.11.095

23- Elhanafi, A. and Kim, C.J., (2018), Experimental and numerical investigation on wave height and power take–off damping effects on the hydrodynamic performance of an offshore–stationary OWC wave energy converter. Renewable Energy, Vol.125, p.518–528. https://doi.org/10.1016/j.renene.2018.02.131

24- Elhanafi, A., Fleming, A., Macfarlane, G. and Leong, Z., (2017), Numerical hydrodynamic analysis of an offshore stationary–floating oscillating water column–wave energy converter using CFD. International Journal of Naval Architecture and Ocean Engineering, Elsevier Ltd. Vol.9(1), p.77–99. https://doi.org/10.1016/j.ijnaoe.2016.08.002

25- Elhanafi, A., Fleming, A., Macfarlane, G. and Leong, Z., (2016), Numerical energy balance analysis for an onshore oscillating water column--wave energy converter. Energy, Elsevier. Vol.116, p.539–557.

26- Zabihi, M., Mazaheri, S. and Namin, M.M., (2018), Experimental Study of Wave Spectrum Type Impact on Inner Chamber Fluctuation , Pressure and Reflection of OWC Device. INTERNATIONAL JOURNAL OF COASTAL AND OFFSHORE ENGINEERING, Vol.2(3), p.19–27.

27- Zabihi, M., Mazaheri, S. and Montazeri, M.M., (2019), *Experimental hydrodynamic investigation of a fixed o ff shore Oscillating Water Column device*. Applied Ocean Research, Vol.85, p.20–33. https://doi.org/10.1016/j.apor.2019.01.036

28- Hirt, C.W. and Nichols, B.D., (1981), *Volume of fluid (VOF) method for the dynamics of free boundaries*. Journal of Computational Physics, Elsevier. Vol.39(1), p.201–225.

29- Elhanafi, A., Fleming, A., Leong, Z. and Macfarlane, G., (2017), *Effect of RANS-based turbulence models on nonlinear wave generation in a two-phase numerical wave tank*. Progress in Computational Fluid Dynamics, an International Journal, Inderscience Publishers (IEL). Vol.17(3), p.141–158.

INTERNATIONAL JOURNAL OF
COASTAL & OFFSHORE ENGINEERING

IJCOE Vol.4/No. 4/ Winter 2019 (9-16)

Available online at: http://ijcoe.org/browse.php?a_code=A-10-215-2&sid=1&slc_lang=en

Study of Internal Waves in the Persian Gulf Using Field Data and Satellite Images

Akbar Rashidi Ebrahim Hesari *1, Sajad Andi2, Hossein Farjami3

*1 *Assistant Professor, Department of Marine Physics, Tarbiat Modarres University, Nour, Iran; akbar.rashidi@modares.ac.ir*

2 *Master Student of Physical Oceanography, Tarbiat Modarres University, Nour, Iran; s.andi@modares.ac.ir*

3 *Faculty Member of Iranian National Institute for Oceanography and Atmospheric Science, Tehran, Iran; h_farjami@inio.ac.ir*

ARTICLE INFO

Article History:
Received: 5 Feb. 2019
Accepted: 24 Feb. 2019

Keywords:
Internal Wave
Persian Gulf
Satellite Images
Field Data
Landsat and SAR Imagery

ABSTRACT

In this research, density, temperature and salinity fields were investigated in different seasons using observational data of ROPME Marine Cruise in the Persian Gulf (PG). Based on in-situ measurements, areas with density stratification were identified. Having analyzed Landsat and SAR satellite images, internal waves (IW) were detected in different regions of the Persian Gulf and more frequently in the eastern part of the PG related to seawater stratification. Based on analysis of satellite images, it is shown that the length of internal waves crest detected in the north-eastern part of Al-Zhahirah (Qatar) was more than 120 km; while it's in range of 5 to 20 km in the south and east of Larak Island, 15 to 40 km in the north-east of Abu Musa Island, and 3 to 65 km in the south-east and south of Hondurabi Island. Moreover, IWs with shorter crest's wide were recognized near Lavan, Siri, Farur, Halul, Khark Islands and Bandar Lengeh, as well. In addition, studying satellite images in the above mentioned areas for a longer time period from 2000 to 2017 showed that IWs mostly occur in the eastern part of the PG in summer and disappear in other seasons.

1. Introduction

Nowadays, the seas and the oceans have important effects on human life and consideration of those effects is a main subject of research in marine environments. Humans exploit the ocean and marine resources and use coasts, extensively. Coastal and offshore constructions are increasingly developed to exploit marine resources including oil and gas resources. On the other hand, seas are considered as one of the best transportation routes in the world. In addition, the oceans play a significant role in the formation of atmospheric systems, climatic changes, rainfall formation, storms, and so on. Although, coastal zones comprise a limited area of the earth's surface, the importance of those areas is far greater than their size. The beaches are places for habitation, recreation, boating, fishing, diving, etc. Therefore, recognizing the processes associated with oceans, seas, and especially coastal waters, such as waves, wind, flow, etc., are of great importance [1].

The processes are affected by physical factors; therefore, to understand the processes and their impacts on human life is necessary to understand the effective and dominant physical processes in such regions [2]. Understanding the physical processes in marine environment helps in better awareness of the resources available to develop and conserve the sustainability of marine environment. For example, temperature and salinity, along with pressure, are important physical properties affecting the seawater density, which play an important role in controlling the dynamics and thermodynamic behavior of seawater and oceanic waters [3]. Heat flux, evaporation, rain, river flow, freezing and melting of sea ice are main factors affecting the temperature and salinity distribution in the oceans. Temperature and salinity changes also directly affect the water density. The distribution of density in the water column in oceans also directly affects the horizontal gradient of pressure as well as oceanic currents. Therefore, the distributions of temperature, salinity and density in the oceans are of great importance [1]. As these physical characteristics are changed temporally and spatially, it is important to study these changes.

Since water covers nearly 70% of the earth's surface, global climatic changes are dependent on the exchange of matter and energy between the atmosphere and hydrosphere. Increasing concerns about the global threat of climate change has increased interests in research and development of renewable energy technologies. The ocean provides a vast source of potential energy resources, and investment in ocean energy is growing as a renewable energy technology. Research on the conversion of thermal energy of the ocean, and waves, tidal and wind energy in the seas and oceans has led to the development of new technologies and, in some cases, commercial development. As it is noted, one of those energy sources is the energy obtained from the oceans and seas. It is hoped that these new energy sources will help reduce the global threats of climate change caused by the use of fossil fuels [4].

The Persian Gulf is a waterbody that runs along the Oman Sea and located between Iran and the Arabian Peninsula. The length of the Persian Gulf from the Strait of Hormuz to its last point in the west is about 990 km and its maximum width is 370 km, which form a semi-enclosed basin that is located between the geographic latitudes 24˚N and 30˚N and geographic longitudes 48˚E and 56˚E [5].

There are no marine ridges in the Strait of Hormuz, and water depth reaches up to 2000 meters only about 200 km far from the Strait of Hormuz toward the Oman Sea. The maximum width of the Persian Gulf is 290 km. The deepest point of the Persian Gulf is 93 m that is located at 15 km distance from Greater Tunb and the Shallowest point with a depth of 10 to 30 m is located in in the western part [6]. The Persian Gulf in the Middle East is considered as a major way to connect Europe, Africa, South Asia and Southeast Asia. It has the most privileged strategic and political status in this region, and establishment of several military bases in neighboring countries of the Persian Gulf shows its military and strategic importance [7].

The internal waves are produced at the interface between two fluids of different densities, which the difference in density is due to the difference in water temperature and salinity at various depths [8]. In other words, similar to different waves are formed in the sea surface, some waves may be formed inside the sea and between different layers with different densities called internal waves [9]. Previous studies conducted on the internal waves have shown that tidal flows are the most important factor in producing these waves [10].

Internal waves created by ship movement were identified by Ekman for the first time in 1904. These waves with wavelengths ranging from a few meters to tens of kilometers, the frequency of a few minutes to several hours and a range of few meters to tens of meters can cause environmental changes such as nutrient mixing, fluctuation in the distribution of biomass and suspended materials in water column [11]. Internal waves can strongly affect the processes in the ocean. The movements caused by internal waves play an important role in the oceanic surface processes. They can move more than a few hundred kilometers, causing mass transmission and impulses. Generally, the formation of internal waves is associated with a significant shear vertically, followed by the processes such as turbulence and mixing. For this reason, the mechanism for the formation, development, and propagation of internal waves is always focused by marine science researchers [12].

These waves may also influence the sound velocity distribution in horizontal and vertical directions, so it is required to investigate such waves specially for submarine navigation. It seems to be essential to conduct research on the internal waves regarding the marine transportation, coastal engineering, aquatic organism movements (as it is important for the fishery), oil projects and offshore platforms [13, 14].

Research on the internal sea waves and turbulence began about a century ago. Jackson (2007) studied the internal waves detection using the Moderate Resolution Imaging Spectroradiometer (MODIS) sensor. In this study, internal waves were studied in 15 regions around the world, including the southern China Sea, the Gulf of California, the Sulu Sea, etc. [15]. Harris and Decker (2017) evaluated the internal waves on the basis of field measurements at Port Susan and Puget Sound. In this study, the data were collected from 2003 and 2005 using CTD, ADCP and visual observation recordes [16]. In another study, Eqtesadi and Bidokhti (2004) studied the role of internal waves in marine water stratification.

In addition to experimental simulation and field study in the Persian Gulf, this study examines the theory of

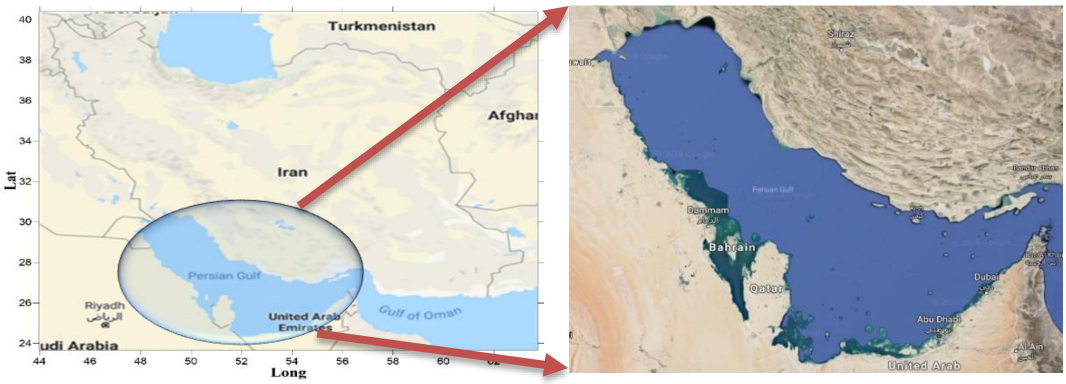

Figure 1. Geographical Location of Persian Gulf

the normal modes of internal waves, which both methods are compared and interpreted [17]. Deldar and Heidari (2017) conducted a study in Iran regarding the identification of internal waves in the Persian Gulf [18].

Generally, measuring the water temperature, or applying salinity sensors, flowmeter and acoustic devices were used to identify the internal waves in the previous studies (e.g., Zhou et al., 1991). Today, satellites are used to detect internal waves, given that internal waves are propagated in a large-scale environment (e.g., Small and Martin, 2001).

2. Materials and Methods

In previous works, the mechanism of formation of the internal waves that is associated with topographic effects, and the formation of these waves due to the movement of tidal currents over the sea bottom friction, oceanic ridges and continental shelf fractures were studied by field measurements, numerical models and satellite images in different oceanic regions. Accordingly, the main objective of this study was to detect internal waves using Landsat 7, Landsat 8, ASTER satellite images and SAR images in the Persian Gulf.

Based on field measurements by marine patrol projects conducted by Regional Organization for the Protection of the Marine Environment (ROPME) and PG-GOOS in the Persian Gulf, the formation of density stratification is evident in most parts of the Persian Gulf, especially in the warm seasons [19].

In this study, the data from marine patrols and associated marine organizations including the Iranian National Institute for Oceanography and Atmospheric Science in 2000, 2001, 2012 and 2013 was used to identify the internal waves formed by stratification of the water column. The location of the measurement stations in those marine patrols, including ROPME, is shown in Figure 3.

To investigate the water stratification, vertical cross-sectional distribution profiles of physical parameters such as salinity, temperature and Sigma-t have been plotted in different seasons using the Grapher software. In the next step, existing field data were analyzed and the areas with density stratification were identified. Then, the satellite images were obtained, which were captured at the same time (in 2000, 2001, 2012, and 2013). Afterward, Internal waves were detected by performing required corrections.

The SNAP and ArcMap software were used to make the corrections to detect internal waves. To find out the permanent or seasonal nature of the internal waves in the Persian Gulf, the satellite images from the five years in all seasons were analyzed and processed after primary processing using appropriate filters by the SNAP and ArcMap software.

In this study, Landsat 7, 8 and Sentinel-1 SAR images captured from 2000 to 2017 were used to detect internal waves in the Persian Gulf. Landsat 8 is the eighth satellite in the Landsat Satellites Program, and is the seventh satellite successfully launched on February 11, 2013 (Landsat 6 was not successfully launched). The satellite has two sensors, one is the operational land imaging sensor and the other is thermal infrared sensor. It also has 11 bands [20]. In this study, bands 4 to 6 were used to detect internal waves in the desired range. The SAR is a radar imaging system extracting a two-dimensional image of a target in both Range and Azimuth directions. As SAR images extract the radial cross section profile of surface or volumetric elements within the microwave wavelengths, they can be a good source for the detection of scattering centers [21]. The C frequency band in SAR radar images was also used to detect internal waves.

Due to the lack of annual field data for the Persian Gulf, Landsat 7, 8, ASTER and SAR images were used for the years without field data, then the internal waves were detected using SNAP and ArcMap software.

3. Results and Discussion

In the present study, by examining a series of physical parameters measured by ROPME and PG-GOOS marine patrols, such as salinity, temperature and sigma t, it was found that internal waves occur in the Persian Gulf during warm seasons. Sea water temperature and salinity changes with depth during the warm seasons, which causes water stratification and form thermocline. It is expected that this stratification will produces internal waves. Also, the satellite images were verified by measured field data. Based on the analysis of satellite images using SNAP and ArcMap software, the crest of internal waves was identified in these areas. These waves are observed mostly in the eastern and central parts of the Persian Gulf.

The incident zones of the internal waves, along with the RAPME patrol stations in 2000 and 2001, and the PG-GOOS patrol in 2012 and 2013, were presented below (Figure 2). It can be shown by investigating the internal waves using the satellite images in the warm season.

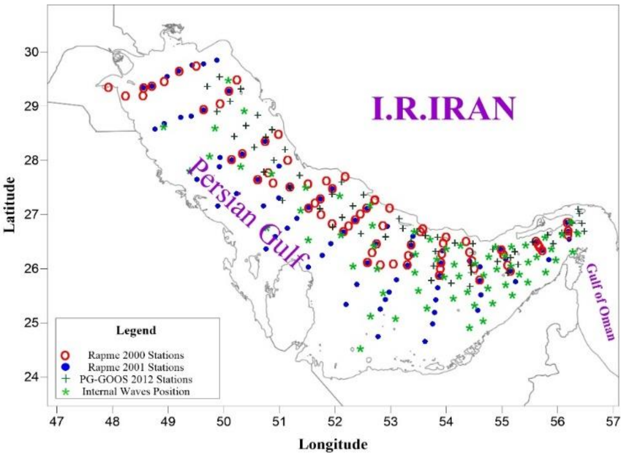

Figure 2. The position of the field measuring stations and the position of the internal waves in the Persian Gulf

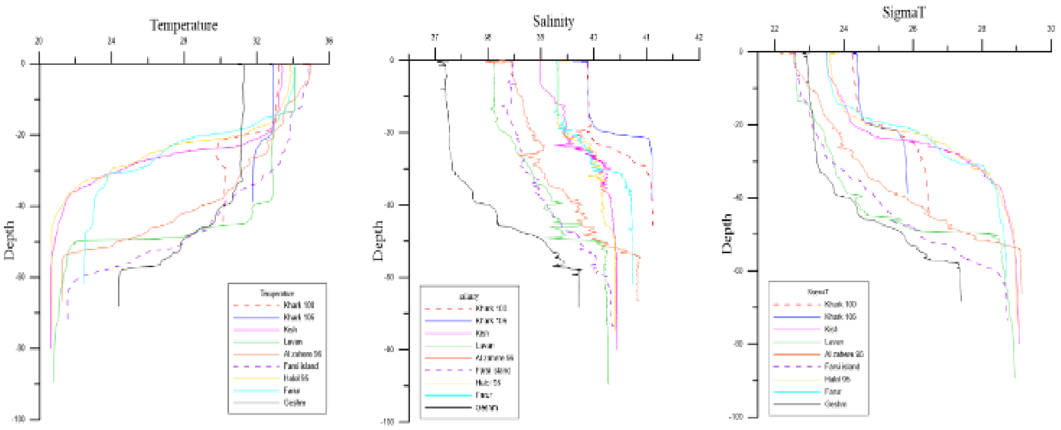

Figure 3. The changes in temperature, salinity and sigma t with depths in different regions of the Persian Gulf during one year in 2000

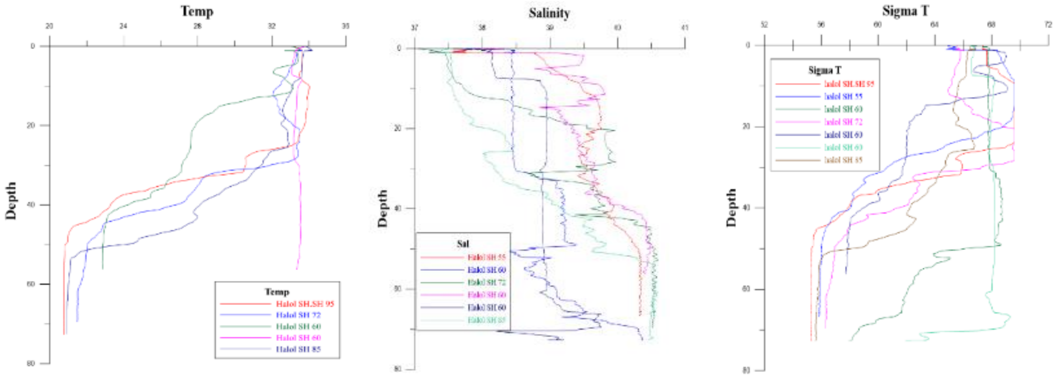

Figure 4. Diagrams of the variations in temperature, salinity and sigma t around Al-Zahereh in 2000

The changes in temperature, salinity and sigma t diagrams in the Persian Gulf were analyzed using the data from ROPME during one year in 2000 (Figure 3). According to these diagrams, it is found that the changes in temperature and salinity were not significant in the cold seasons. On the contrary, the changes in temperature and salinity in warm seasons were high in most areas, indicating the stratification of the water column in such areas.

The vertical diagrams of the physical parameters show that there are high changes in temperature, salinity, and sigma t in the warm seasons, resulting in high stratification variations, which form thermocline in the warm seasons when the internal waves are formed based on the stratification in water column.

All possible areas were investigated using satellite images and compared with field data, some of which are presented here. Figure 4 shows the temperature, salinity and sigma t changes in 2000 around the Al-Zahereh. According to the temperature diagram, the temperature strongly changes around the Al-Zahereh at a depth of 20 to 40 meters (decreased from 31°C to 21°C), but no significant changes can be seen in in salinity. The changes in sigma t were also observed at a depth of 20 to 45 meters. These variations indicate that the stratification and thermocline occur in the basin due to the strong changes in temperature and sigma t.

As a result, stratification is more evident in water bodies of this region based on temperature and sigma t changes. Therefore, according to the field data, internal waves are expected to occur around the Al-Zahereh, as it easily can be seen on the satellite images.The image recorded by Landsat 7 on 15/04/2003, shows the internal waves around the Al-Zahereh (Figure 5). The waves begin to spread at a distance of 55 km from the north-east of Al-Zahereh, and progressed to the northern parts of the city. The direction of these waves are towards the north and west. This image was captured at the same time when the field data were measured. Therefore, it can be concluded that the main cause of the internal waves in this region is the effect of water column stratification.

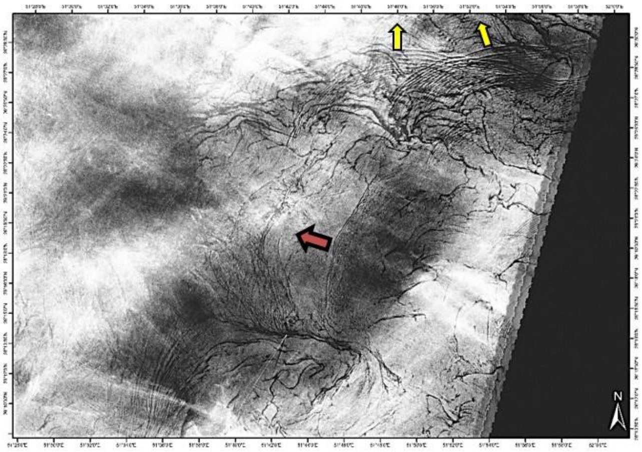

Figure 5. Landsat 7 image, internal waves around the Al-Zahereh on 15 April 2003

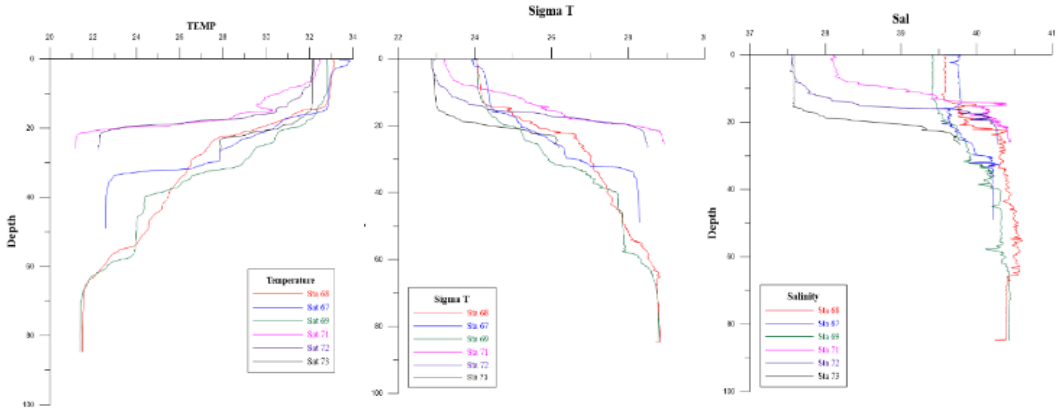

Figure 6. Diagrams of temperature, salinity and sigma t variations with depth around Abu Musa Island in 2001

The temperature, salinity and sigma t variations with respect to the water depth around the Abu Musa Island in 2001 are illustrated in Figure 6. There are strong changes in temperature at depths between 15 and 40 m, as well as strong changes in sigma t at depths between 18 and 35 m indicating that water stratification and thermocline occurred in this basin due to the strong changes in temperature and sigma t. Salinity changes are negligible as the depth is changed, therefore it has lower effect on stratification than temperature and salinity (sigma-T). Accordingly, internal waves are expected to occur around the Abu Musa Island, as it can be seen in satellite images.

Figure 7 shows the internal waves around the Abu Musa Island captured by ASTER in the summer of 2001. These waves propagate to the west and south-west. There are two internal wave packages that are located at 15 km distance from northeast and 20 km distance from the northwest of the island. According to the temperature and salinity diagrams, their variations are high in this area and stratification occurs. As expected, the internal waves are due to the water column stratification in this region.

The diagrams of temperature, salinity and sigma t variations with respect to the water depth around the Hondurabi Island in 2013 are presented in Figure 8. There are strong changes in temperature at depths between 35 and 60 m, as well as strong changes in sigma t at depths between 35 and 50 m indicating that water stratification and thermocline occurred in this basin due to the strong changes in temperature and sigma t. Salinity has lower effect on stratification than temperature and salinity (sigma-T), because it changes slightly by changes in the water depth. Accordingly, internal waves are expected to occur around the

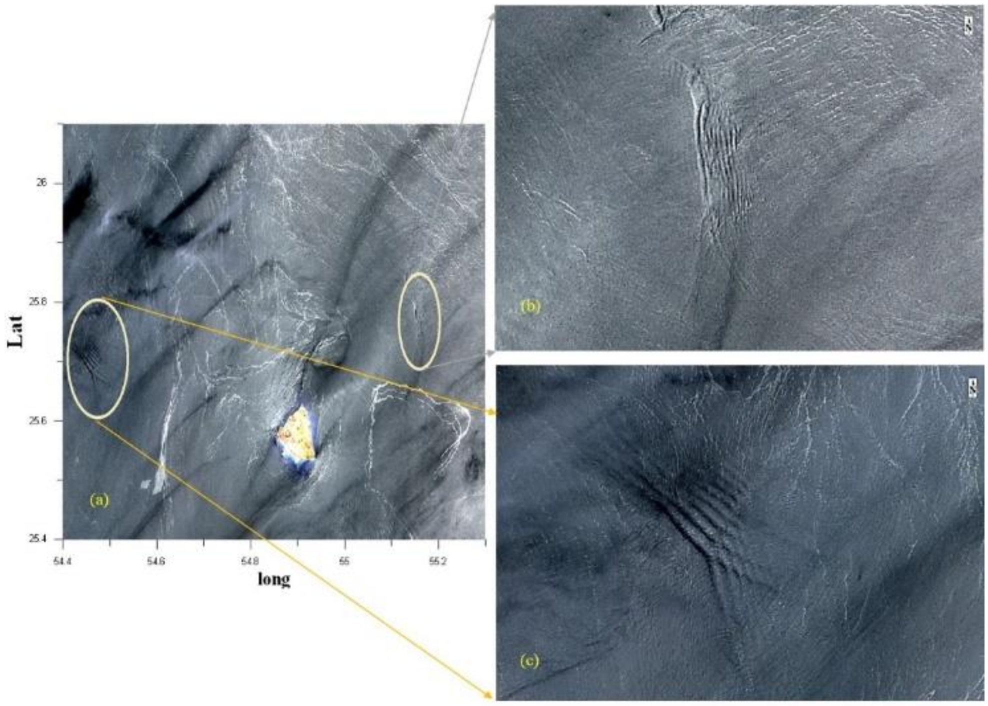

Figure 7. ASTER image recorded on 13 May 2001, (a) An overall view of Abu Musa Island and areas around it; (b) Internal waves at 15 km distance from the northeast of Abu Musa Island; (c) Internal waves at 20 km distance from the west of Abu- Musa Island

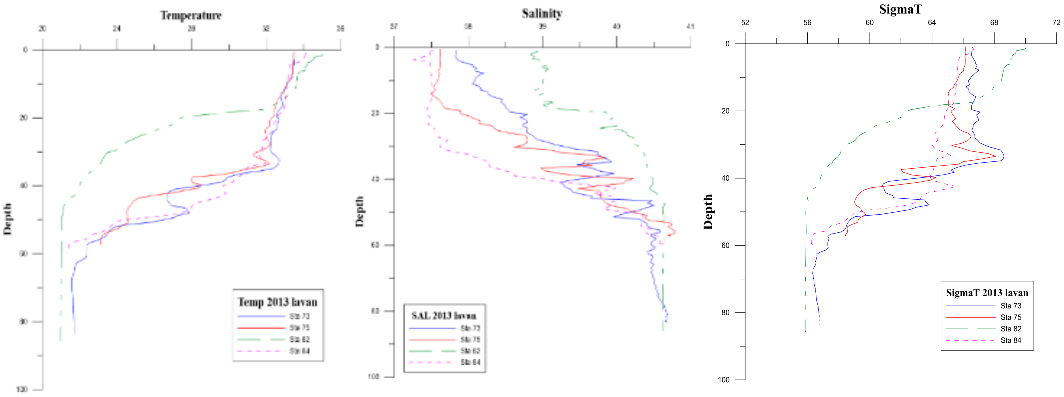

Figure 8. Diagrams of temperature, salinity and sigma-T variations with depth around Hondurabi Island in 2013

Hondurabi Island, as it can also be seen in satellite images recorded in the warm season of 2013.

The image recorded by Landsat 8 on 23 June 2013, shows the internal waves at a distance of 46 to 60 km from south of Hondurabi Island (Figure 9). This waves package propagates toward the southeast and western. According to the temperature and salinity diagrams, their variations are high in this area which result in water column stratification. As expected, the internal waves occurred due to the water stratification in this region.

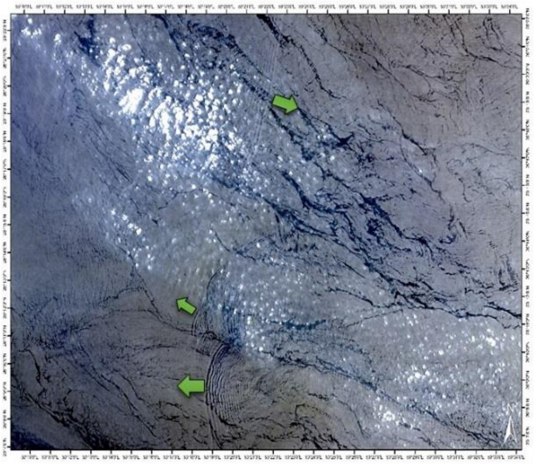

Figure 9. Landsat 8 image showing internal waves around the Hondurabi Island on 23 June 2013

Also, water column stratification is not expected to occurs in the cold season due to the lower temperature and low changes in water salinity and sigma t. To evaluate this hypothesis, field data recorded in the Das Island was analyzed. Figure 10 shows temperature, salinity and sigma t changes in the cold season of 2012. The results showed that water column stratification do not occurs in these area in the cold season. Therefore, water internal waves are not expected to occur in the region during the cold season, which can be clearly seen by analyzing the satellite images in the cold season of 2012.

The location of Das Island is shown in the image recorded by ASTER on 2 October 2012 (Figure 11). Analysis of the satellite images showed that internal waves do not occur around Das Island in the cold season. According to the temperature, salinity and sigma-T diagrams, the variations of these parameters are low in this area and there is no stratification in the water column. As expected, the internal waves also do not occur due to lack of stratification in this region in the cold season.

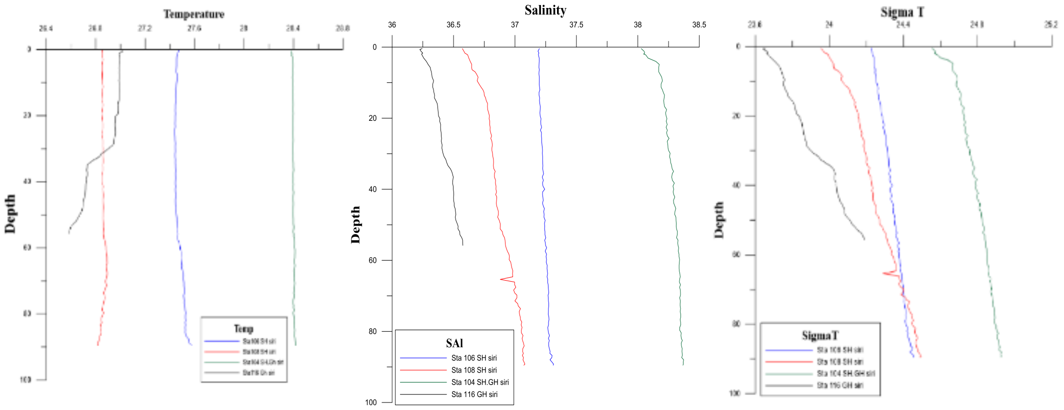

Figure 10. Temperature, salinity and sigma-T variations around Das Island in the cold season of 2012

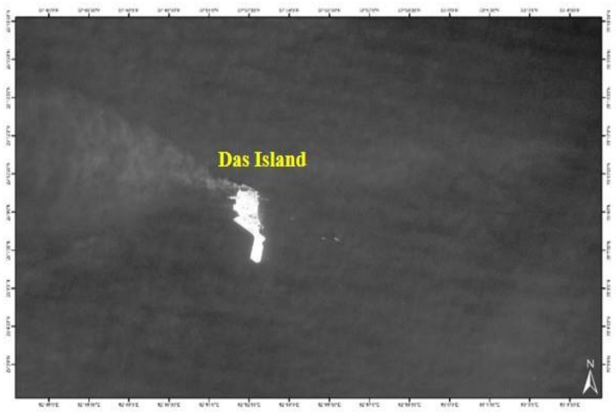

Figure 11. ASTER image showing internal waves around Das Island on 10 October 2012

In this study, due to the lack of field data from 2000 to 2017, Landsat, ASTER and SAR images were used for the years that field data were not available to determine the existence of internal waves in different areas of the Persian Gulf, as well as the continuity of these waves in the warm season. Then, the internal waves were detected using SNAP and ArcMap software. Figure 12 shows Landsat satellite images for the years 2002 and 2014. It shows how the waves may be generated. Figure (12a) shows the internal waves at a distance of 12 km from north of the Farur Islands in 2014 and Figure (12b) shows the internal waves at a distance of 6.5 km from west of Larak Island in 2002 that their direction is toward the northwest.

The internal waves were detected based on the satellite images from Landsat and SAR in 2000 and 2017. Figure (13c) is the sentinel-1 image recorded on 20 August 2015 showing the internal waves in the northwest of Farsi Island, and Figure (13d) is the SAR satellite image of Sentinel-1 recorded on 29 March 2015 showing the formation of internal waves at a distance of 35 km from the east of Khark Island (Figure 13).

The internal waves were not considerable based on the Landsat, ASTER and SAR images in the studied area

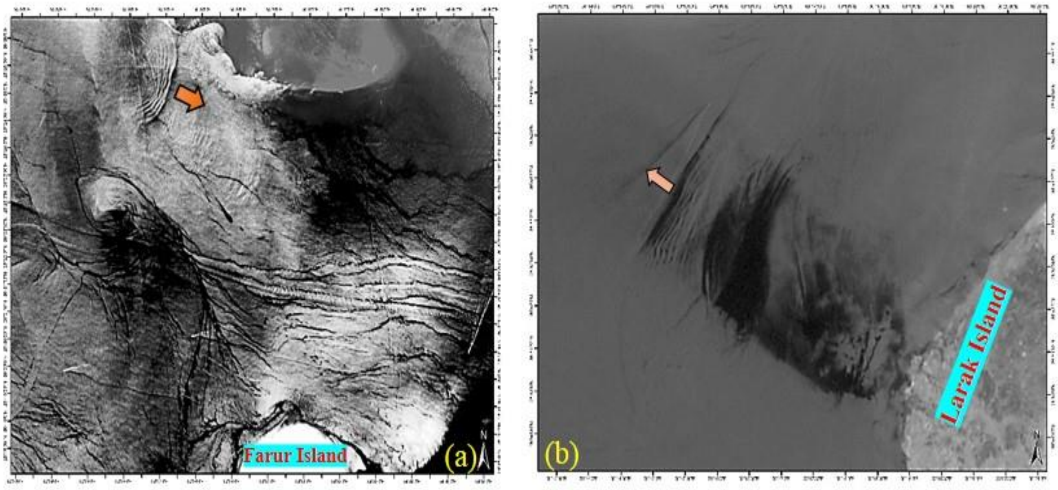

Figure 12. Landsat image showing the internal waves, (a) the internal waves around Farur Islands recorded on 07 April 2014; (b) the internal waves around the Larak Island on 25 May 2002.

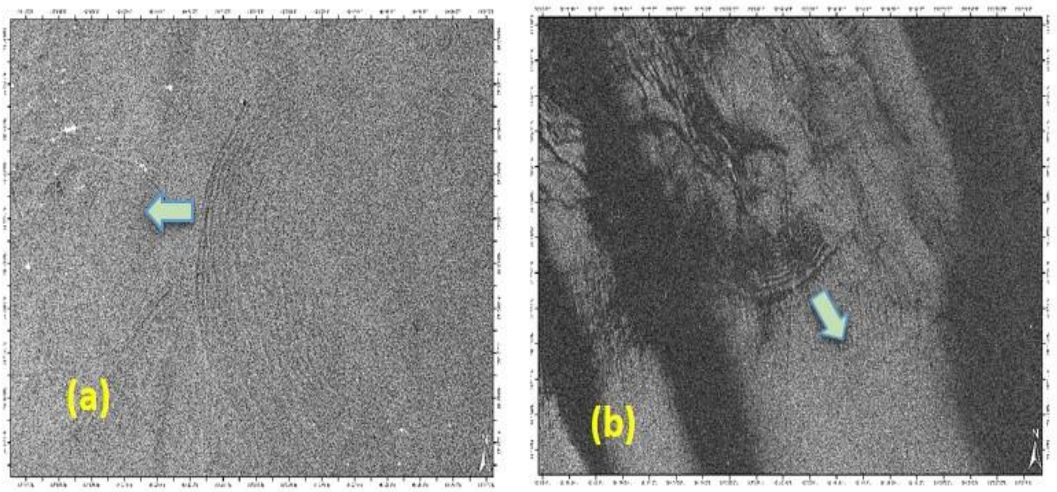

Figure 13. SAR Satellite images of Sentinel-1 showing the internal waves, (a) the internal waves around Farsi Island recorded on 20 August 2015; (b) the internal waves around the Khark Island on 29 March 2015.

during the cold seasons. Thus, it can be concluded that the internal waves occurring in different parts of the Persian Gulf are not permanent and occur only in the warm season during summer, when strong changes in temperature, salinity, and density in the vertical direction lead to the stratification of water column. Therefore, the occurrence of internal waves in different regions of the Persian Gulf can be considered as seasonal phenomenon that is corresponded to the water column stratification.

4. Conclusions

In this study, water temperature, salinity and density were studied in different seasons of the year based on the field data from marine patrols in the Persian Gulf. In addition, Landsat, ASTER and Sentinel-1 (SAR) images were analyzed by SNAP and ArcMap software to detect the occurrence of internal waves in the Persian Gulf. Internal waves were detected during warm season according to the satellite images. Based on the analysis of satellite images, the length of the crest of the internal waves detected in the north-eastern part of the city of Al-Zahereh (Qatar) were more than 120 km; the south and southwest of Khark Island were about 100 km, the north-west of Abu Musa Island 3 to 35 km; and south and southwest of Hondurabi Island was estimated as 20 to 65 km.

In conclusion, internal waves in the Persian Gulf appear to be observed at relatively high density (frequency) in the warm seasons, corresponding to the stratification of the sea water column. Finally, other factors, such as the movement of tidal currents over the sea bottom with variable slope, do not play a significant role in the formation of internal waves.

5. References

1- Stewart, R.H., (2008), *Introduction to Physical Oceanography,* Department of Oceanography Texas A & M University, USA, 2008 Edition: 345 p.

2- Simpson, J.H. and Sharples, J., (2012), *An Introduction to the Physical and Biological Oceanography of Shelf Seas*, Cambridge University Press, Cambridge: 424 p.

3- Chand, S., Aung, T. and Rao, S., (2004), *Physical properties of southern Fiji waters,* The South Pacific Journal of Natural and Applied Sciences, Vol.22(1), p.57-61.

4- Pelc, R. and Fujita, R.M., (2002), *Renewable energy from the ocean,* Marine Policy, Vol.26(6), p.471-479.

5- Emery, K.O., (1956), *Sediments and water of the Persian Gulf,* AAPG Bull 40, p.2354-2383.

6- Layeghi, B., Ghader, S., Aliakbari Bidokhti, A. and Azadi, M., (2016). *Sensitivity testing of WRF model simulations to physical parameters in the Persian Gulf and Oman Sea during the Summer Monsoon. Iranian journal of Geophysics*, Vol.11(1), p.1-19 (in Persian)

7- Reynolds, R.M., (1993), *Physical Oceanography of the Persian Gulf, Strait of Hormuz, and the Gulf of Oman-Results from the Mt. Mitchell Expedition*, Marine Pollution Bulletin, Vol.27, p.35–59.

8- Filonov, A.E. and Trasvina, A., (2000), *Internal Waves on the Continental Shelf of the Gulf of Tehuantepec, Mexico*, Estuarine, Coastal and Shelf Science Vol.50(4), p.531–548.

9- Pond, S. and Pickard, G.L., (1983), *Introductory Dynamical Oceanography*, Butterworth and Heineman Ltd, 328 p.

10- Thorpe, S.A., (2005), *The turbulent ocean*, Cambridge University Press, 230 p.

11- Holbrook, W.S. and Fer, I., (2005), *Ocean internal wave spectra inferred from seismic reflection transects*, Geophysical Research Letters, Vol.32(15), p.1-4.

12- Lavrova, O. and Mityagina, M., (2017), *Satellite Survey of Internal Waves in the Black and Caspian Seas*, Journal of Remote Sensing, Vol.9(9), p.1-27.

13- Duda, T.F. and Preisig, J.C., (1999), *A modeling study of acoustic propagation through moving shallow-water solitary wave packets*, IEEE Journal of Oceanic Engineering, Vol.24(1), p.16–32.

14- Belov, A.I., Zhuravlev, V.A. and Serebryanyi, A.N., (2006), *Sound Field Variations Caused by Intense Internal Waves in a Shallow Sea with a Weak Thermocline*, Acoustical Physics, Vol.52(2), p.132–137.

15- Jackson, C., (2007), *Internal wave detection using the moderate resolution imaging spectroradiometer (MODIS)*, Journal of Geophysical Research: Oceans, Vol.112(11), p.1-13.

16- Harris, J.C. and Decker, L., (2017), *Intermittent large amplitude internal waves observed in Port Susan, Puget Sound*, Estuarine, Coastal and Shelf Science, Vol.194, p.143-149.

17- Eghtesadi, SH., Aliakbari Bidokhti, A. and Zarganjfard, P., (2003), *Normal modes of internal waves for creating layered structures in the ocean (Persian Gulf)*, Scientific and technical journal of Iranian Meteorological Organization, Vol.50, p.7-28. (in Persian)

18- Deldar, H. and Heydari, A., (2017), *Identification of Internal Waves in the Persian Gulf*, First International Conference on Oceanography of Western Asia, 8-9 November, Tehran, Iran. (in Persian)

19- Majidi Nik, M., (2013), *Changes in physical parameters, stratification and stability of the water column in the Persian Gulf*, M.Sc. thesis, Tarbiat Modares University. (in Persian)

20- USGS., (2013), *Landsat Data Continuity Mission*, Yale University, Yale Guide to Landsat 8 Image Processing.

21- Cumming, I.G. and Wong, F.H., (2005), *Digital Processing of Synthetic Aperture Radar Data: Algorithms and Implementation,* Artech House, London.

INTERNATIONAL JOURNAL OF
COASTAL & OFFSHORE ENGINEERING

IJCOE Vol.4/No. 4/ Winter 2019 (17-23)

Available online at: http://ijcoe.org/browse.php?a_code=A-10-169-1&sid=1&slc_lang=en

Reliability Analysis of Subsea Pipeline against Upheaval Buckling

Abdolrahim Taheri[1*], Mahdi Tasdighi[2], Mohammad Bagher Faraji[2]

[1] *Assistant Professor, Department of Offshore Structural Engineering, Petroleum University of Technology, Iran; rahim.taheri@put.ac.ir*
[2] *MSc Student, Department of Offshore Structural Engineering, Petroleum University of Technology, Iran*

ARTICLE INFO

Article History:
Received: 6 Sep. 2018
Accepted: 6 Mar. 2019

Keywords:
Upheaval Buckling
Reliability
Subsea Pipeline

ABSTRACT

The importance of oil transportation in the maritime industry has increased in recent years due to increased oil and gas production. According to technical and financial aspects, on hydrocarbon transfer methods, the pipelines are the best option for the transfer of oil and gas in the maritime industry. High temperature and high pressure in the pipeline can lead to the buckling. Buckling can either be in the direction of vertical (upheaval) and horizontally (lateral). The uncertainty in the buckling parameters of the pipeline increases error in the uplift and the effective axial compressive force calculation. The existence of these errors in the pipeline design is costly for the project. So reducing the errors can be very important. This paper presents the reliability analyses for studying and quantifying the variation of the reliability index (β) with the main parameters involved during the upheaval buckling of submarine buried pipes caused by high temperature and pressure conditions (HTHP). In this paper, uncertainty is considered in the geometric parameters of the pipeline. PDF and reliability index (β) can be determined by FORM and other. FORM, FOSM and sampling methods are three main methods which are used to account the PDF and reliability index (β). This research shows that among these three methods, for a fixed state, the sampling method has the lowest beta and the highest probability of buckle, which has a higher accuracy than the other methods. For soil cover with a thickness of more than 1000, it is worth noting that by increasing the thickness of the soil cover, more force is required for the upheaval buckling in the pipeline.

1. Introduction

Offshore pipelines are used for some targets in the development of submarine hydrocarbon resources. Submarine Pipelines as one of the most effective tools for transporting hydrocarbon productions from the well to the terminals/the platform located on the shore are considered [1,2]. Nowadays, pipelines go deeper and cover a wide range of miles. As offshore industries go for deeper resources, so pipelines should be checked to resistance against new loads in subsea condition [3]. Due to the high uncertainty in the new environment and also in the operating conditions of the pipelines, need to use of methods based on reliability greatly increases.

To measure the reliability of a system, the system first breaks down into components, and the reliability of the system is expressed in terms of the reliability of its components. To calculate the reliability of each component based on available statistical data, a model for the failure rate is selected and its parameters are estimated based on available data. Reliability evaluation methods, considering the uncertainty in the geometric parameters of the structure as well as the environmental conditions, show the probability of failure of the structure under special loading conditions. Uncertainties affecting the health of marine structures, such as drought structures, exist both in loading and in the strength of structural components and fittings. Resistance of marine structures should provide health and safety of the structure in different loading conditions.

Buckling as one of the ultimate limit state failure modes, affect son the maintenance costs. Normally, buckling can be occurred in two modes: Global and Local. Local buckling occurs due to the out-of-roundness and global buckling happens due to high temperature/ high pressure gradient along subsea pipelines. Based on the buckle plane, global buckling can be occurred in horizontal and vertical direction which are called lateral and upheaval buckling, respectively [4, 5]. Furthermore, lateral and upheaval buckling occur for on-bottom and buried pipelines, respectively.

If a pipeline is not free to expand in the operation, restrained axial deformation results in an axial compressive force in the pipeline. The pipeline usually is not perfectly straight with some out of straightness (OOS), and the imperfections are typically due to the pipeline being laid over irregularities in the seabed profile. When the lateral restraint of a trenched pipeline exceeds the vertical restraint force against vertical displacements created by the pipeline submerged weight, the pipeline bending stiffness, and the covered soil resistance, the pipeline tends to move upward, and considerable uplift movement may occur. This phenomenon is called upheaval buckling [6, 7, 8], which is a failure mode that has to be taken into account in the design of buried and trenched pipelines. The pipeline moves upward due to upheaval buckling, leading to possibly unacceptable local plastic deformations or collapse or vulnerability to fishing gear and other third-party activities. The upheaval buckling of a pipeline has been known for a long time as a problem of land pipelines, and it has become one of the primary concerns in submarine pipeline design [9].

The DNV-OS-F101 [10] gives criteria and recommendations on concept development, design, construction, operation, and abandonment of submarine pipeline systems and The DNV-RP-F110 [11] is the common industry recommended practice for designing submarine pipeline against global buckling. The DNV uses the mean values of soil uplift resistance and driving force (i.e., on effective axial load) in the design process as a deterministic method. The variability in soil resistance and force is reduced by applying the load factor (γ_{UF}) on driving force. The appropriate values for partial safety factors (γ_{UR}, γ_{UF}) should be used in the design phase to increase the safety and the factors depend on the accuracy of field measurements and the targeted safety class. This conventional deterministic method is simple and straightforward but does not take into account the variability in appropriate manner. Thus the methodology does not explicitly consider the effect of variability in backfill stiffness or operational conditions in the safety assessment against upheaval buckling. These aspects can be examined by probabilistic approach consideration the variability in the inputs and assessing their effects on the overall upheaval buckling behavior.

On the other hand, in a probabilistic approach, the input parameters and loading are treated as continuous random variables and the performance of the structure resulting from different failure criteria is expressed in probabilistic framework as probability of failure (P_f) and/or reliability index (β) [12].

Al-Sharif et al. [14] in a paper with topic “Structural Reliability Assessment of the Oman India Pipeline” investigated the effect of variability in soil backfill stiffness and operation conditions on the performance of the pipeline upheaval behavior. And its result was useful to better understand the performance of offshore pipeline and probabilistic upheaval buckling assessment.

In this paper, the effect of variability in pipe properties that contains thickness, diameter and elastic modulus of the pipeline are investigated.

2. Case Study

The considered steel pipeline has a diameter (D) of 0.816m (32.12 in.), thickness of 0.0242 m and a length of 40 m. The buckling length could be influenced by the imperfection height; thus, it was decided to consider the length of 40 m. Poisson’s ratio (ϑ) of the pipe was considered equal to 0.3and the coefficient of thermal expansion (α_t) was equal to11.5×10^{-6}°C^{-1}. The distribution of undrained shear strengths was determined to be lognormal using the field data. Residual tension during installation was not considered in this study. The reasons for neglecting the residual tension are that those axial forces are generally associated with a high degree of uncertainty and their influence is very case-specific [13].Pipeline Submerged Weight in Operation Condition is equal to 4273(N/m). Table1 presents the general parameters of pipelines.

Table 1. The properties of the pipeline [13]

Characteristic	Value
Pipeline outside diameter	0.816 [*m*]
Steel pipeline wall thickness	0.0242 [*m*]
Steel pipeline density	7850 [kg/m^3]
Modulus of elasticity	210 [*GPa*]
Poisson’s ratio	0.3
Thermal expansion coefficient	11.5×10^{-6}°C^{-1}
Pipeline submerged weight in operation condition	4293 [*N/m*]
Maximum water depth	85 [*m*]
Seawater density	1023 [kg/m^3]
Difference Between Operating and Installation Temperature	75 [*c*]
Local Incidental Pressure During Operations	10.8493 [*MPa*]

Table 2. Uncertainties of parameters with their relevant mean and C.O.V [13]

Row	Parameter	Distribution Type	Mean	C.O.V
1	Young’s modulus	Log-normal	210×10^9	0.05
2	Pipeline wall thickness	Normal	0.024	0.05
3	Pipeline diameter	Normal	0.6156	0.05

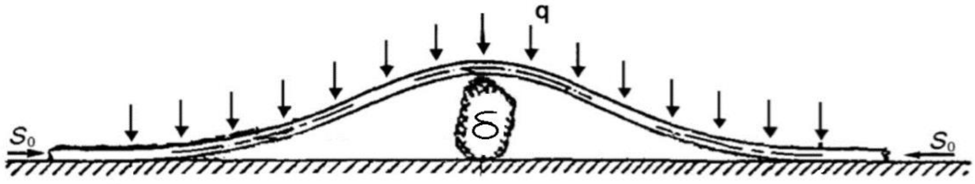

Figure 1. Schematic diagram of buried offshore pipeline profile [9]

3. Analytical Solution of Upheaval Buckling

Upheaval buckling is caused by an increase in effective compressive axial force in buried pipelines lying on an uneven seabed, due to pressure and temperature in the operating condition. The upheaval buckling phenomena is related to the following factors [9]:

- The geometry, weight, and material properties of the pipeline.
- Operational pressure and temperature.
- Seabed profile and environmental characteristics.
- Cover and soil properties.

The vertical imperfections in pipelines are defined as as-trenched out of straightness, which are associated with upheaval buckling from the following sources:

- Imperfections of foundation (seabed), such as bounder, seabed profile, pipeline crossing locations, and the like. Depending on the shape of the foundation, the pipeline may follow the shape of the foundation.
- Pipeline imperfections introduced during the installation process by, for example, the reeling process or poor lineup during the welding process. The pipeline imperfection can be described in terms of its height and length, which may be determined by survey in the construction phase.
- Pipeline imperfections in the trench after the laying and trenching operation, such as variations in trencher performance or stop and start of the plough.

The driving force for triggering the pipeline upheaval buckling is the compressive axial force in the restrained pipeline due to the increase of temperature, the increase of internal pressure, and the residual tension left by laying pipe. The effective axial compressive force of fully constrained pipelines can be expressed as:

$$S_0 = F_{residual} - (1 - 2\nu)(\Delta P_i)A_i - EA_S\,\alpha(\Delta T_i)(1)$$

Where in Eq.(1)S_0stands for effective axial compressive force, (compressive, –; tension, +), ΔP_i stands for difference of internal pressure relative to laying condition Since the internal pressure during installation normally is zero, this is identical to the operating internal pressure, ΔT_i stands for difference between operating temperature and installation temperature, A_i stands for Internal bore area of the pipe, A_S stand for cross-sectional area of the pipe, $F_{residual}$ stands for residual lay tension, ν stands for Poisson's ratio, E stands for Young's modulus and α stands for thermal expansion coefficient.

Figure 1 illustrates the profile of pipeline with a vertical imperfection under axial and vertical loads. This is a typical configuration for pipeline crossing. The horizontal distance is denoted by x, measured from the left pipeline touchdown point. The height of the pipeline is denoted by w, measured upward from seabed. The height of the vertical imperfection is denoted by δ, the total pipeline span length is 2L. Only half of the system is considered, due to symmetry.

The pipeline is idealized as an elastic beam that carries an effective axial force $S_0$and has flexural rigidity EI. It follows from elementary beam-column theory that the downward load q(x) per unit length required to maintain the pipeline in equilibrium condition is [9]:

$$EI\,\frac{d^4w}{dx^4} - S_0\,\frac{d^2w}{dx^2} = -q \qquad (2)$$

For the deflection shape of an elastic pipeline with no internal axial tension but with a bending stiffness of EI placed over an object with height of δ_f and loaded with a pipeline submerged weight per unit length, wS, Eq.(3) gives the span length as [9]:

$$L_0 = \left[\frac{72 \times EI \times \delta_f}{w_S}\right]^{1/4} \qquad (3)$$

The analytical solution also gives the pipeline profile by following equation [9]:

$$w(x) = \delta_f \times \left(\frac{x}{L_0}\right)^3 \times \left(4 - \frac{3x}{L_0}\right) \qquad (4)$$

3. Reliability Assessment

A reliability assessment accounts for the inevitable variability in pipe properties (geometry and material strength) which is the result of the normal perturbations in manufacturing processes used to produce the pipe. Variability in pipe properties produces uncertainty in respect of collapse resistance, which can be addressed and managed through the reliability assessment.

The collapse pressure limit state depend on the pipe dimensions (diameter, ovality and wall thickness), and material strength properties (stress-strain curve in the hoop and axial directions). Therefore, it is necessary to develop appropriate probability density functions (PDFs) which characterize the expected statistical variations in these geometric and material properties, for use in a reliability analysis.

In the present context, Reliability is defined as the probability that an individual length of pipe will not collapse due to a combination of external pressure and bending loads during construction or operation. Reliability is equal to the probability of failure subtracted from unity [14].

4. Analysis Methodology

For the problem under consideration, the probability of failure is equal to the probability that the load effect, exceeds the collapse resistance, R (or probability that R-L≤0).This is described mathematically by P (g ≤ 0), where g is the limit state function of a set of random parameters X that influence L and R, and we are therefore interested in evaluating the probability P (g ≤ 0) where:

$$g = g(x) \tag{5}$$

This probability is equal to the probability of occurrence of all combinations of the parameters X that lead to g≤0. These combinations can be visualized as the domain in the n-dimensional space of X variables (where n is the number of variables in the set X) on one side of the function g≤0. Thus the failure probability is expressed by:

$$P_f = P(g \leq 0) = \int_{g(x)\leq 0} \{f_x(X)dx\} \tag{6}$$

Where f(X) is the multivariate density function for the random vector X.

The limit state function g(X), is so defined so that:

$$g(x) = \begin{cases} > 0 & safe\ state \\ = 0 & limit\ state \\ < 0 & failure\ state \end{cases}$$

Since the basic random variables am modeled by continuous probability functions and the failure probabilities are small, it is preferable to apply the analytical first and second order reliability methods (FORM and SORM). These methods are very efficient and accurate for small failure probability problems, FORM is of particular interest when the limit state function is relatively simple (i.e. expressed analytically).

In general, numerical solution is necessary by one of two classes of methods: (i) Monte Carlo simulation and (ii) Reliability Methods.

The Monte Carlo simulation method is conceptually simple. It is based on numerical sampling where a set of x values are simulated from the corresponding probability distributions. These values are substituted in the function g(x) and the value of g is compared to zero. The process is repeated a large number of times and count is kept of the ratio between the number of trials that lead to g ≤ 0 and the total number of trials. The ratio is used as an estimate of the desired probability value.

Reliability methods, which is developed in connection with structural reliability, provides approximate solutions for general probability integrals of the type in Eq.(6) over domains with smooth boundaries. The approximations involve a transformation of all parameter distributions into independent normal variables and the replacement of the function g(X) by an approximate one. This allows the use of a special case for which an analytical solution for Eq.(6) exists. Of the two basic methods available, SORM provides a more accurate approximation than FORM because the function g(X) is approximated by a second order Taylor series expansion as opposed to a first order expansion used in FORM. It is also possible to increase the accuracy of SORM results by using a simulation procedure which by virtue of the SORM analysis can be done very efficiently.

Each of the above approaches has advantages and disadvantages. The Monte Carlo method is conceptually simple and can easily deal with parameter dependencies, distribution truncations and discrete random parameters. The main disadvantage is that in most practical cases a very large number of simulations (tens to hundreds of thousands, or even more for small probabilities) are needed and this tends to pose restrictions on the number of analyses that can be carried out, However, it must be noted here that there am some recent developments in this method which may result in enhancement in efficiency.

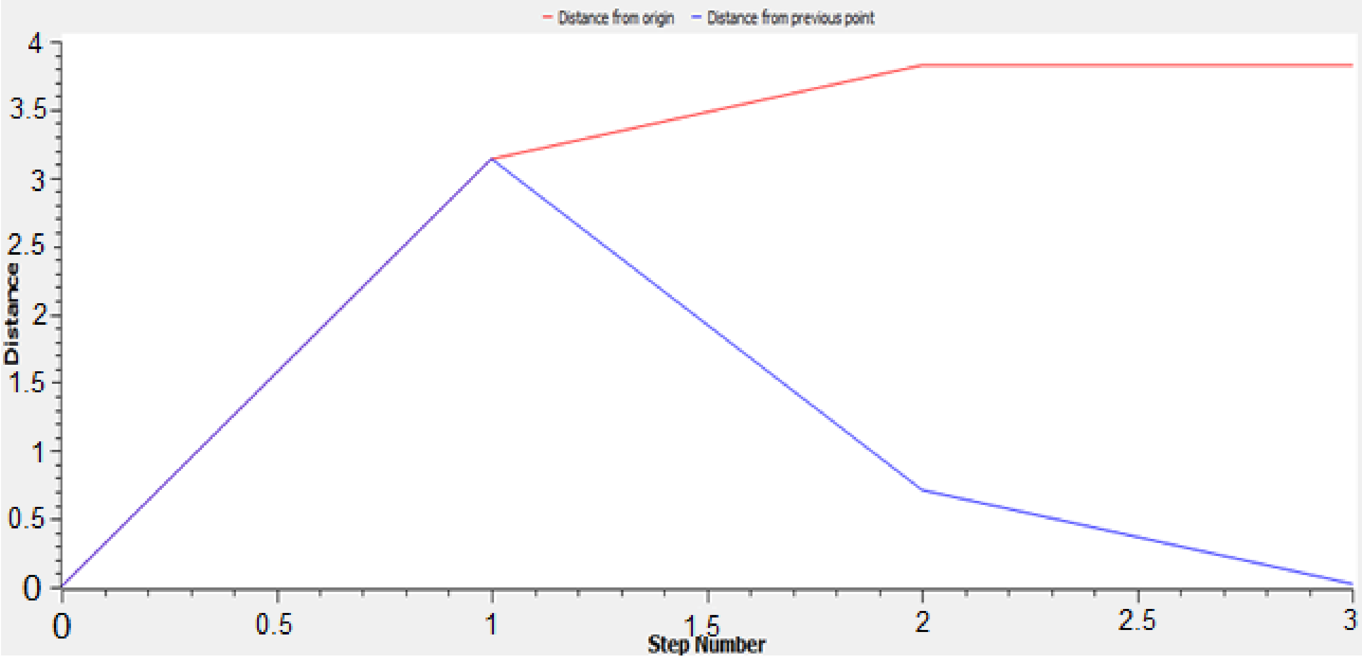

Figure 2. PDF method

FORM and SORM have the advantage of being very efficient. Results can usually be obtained in a fraction of the time required for a Monte Carlo simulation. In addition the analysis provides, as a by-product a measure of the sensitivity, within the overall probability of failure to the different input variable parameters and their distributions. These methods have also been shown to provide sufficiently accurate solutions for small probabilities in a wide range of practical problems. Their disadvantage is that they use iterative numerical procedures which am not guaranteed to converge and occasionally cases may be encountered for which solutions cannot be found [14].

The reliability analyses have been computed by linking the buckling model to the reliability analysis software RT. The reliabilities have been calculated by use of FORM, SORM and the Monte Carlo method.

5. Results and Discussion

This paper presents the reliability analyses for studying and quantifying the variation of the reliability index (β) with the main parameters involved during the upheaval buckling of submarine buried pipes caused by high pressure and temperature conditions (HPHT).

In order to assess the effect of geometric specification's pipeline on upheaval bucking of subsea pipelines using DNV recommended model(Eq.(2)), the downward load q(x) per unit length required to maintain the pipeline in equilibrium condition is calculated for uncertainties of parameters that shown in Table 2.

Snap buckling generally occurs with a jump of vertical movement of pipeline because the driving force is sufficient to overcome all resistive forces when the pipeline is first put into operation. Upheaval creep is a phenomenon in which a buried pipeline progressively moves upward through backfill material due to driving forces by cyclic thermal loads of heat-up and cool down.

The distributions of the uplift motion are obtained by using Eq.(4)(vertical slip model),which involves lognormal distributed random parameters.

The results of the reliability evaluations for uncertainties of parameters assumed in the analysis are presented in Table 2. Uncertainties which are considered for reliability assessment are described in Table 2. The ratio of distance to step number for pipeline with introduced uncertainties in FORM method for soil cover equal to 1000(mm) is shown in Figure 2.

CDF and PDF diagram represents the uncertainty characteristics of the considered parameters. These graphs are constant for all methods of calculating the probability of failure.

Reliability methods as a mathematical tool, are used for determining probability of failure (POF) in some special conditions by considering uncertainties in both load and resistance parameters [15]. The uncertainties can be divided to epistemic and aleatoric [16].

P_f and reliability index (β) can be calculate by FORM and other methods [17]. In this research used 3 methods. FORM, FOSM, sampling are 3 main method for P_f and reliability index (β) determination. Table 3 shows theβ in different methods.

Figure 3 indicated 3 curves of PDF, CDF and COV in sampling method that shown in one graph.

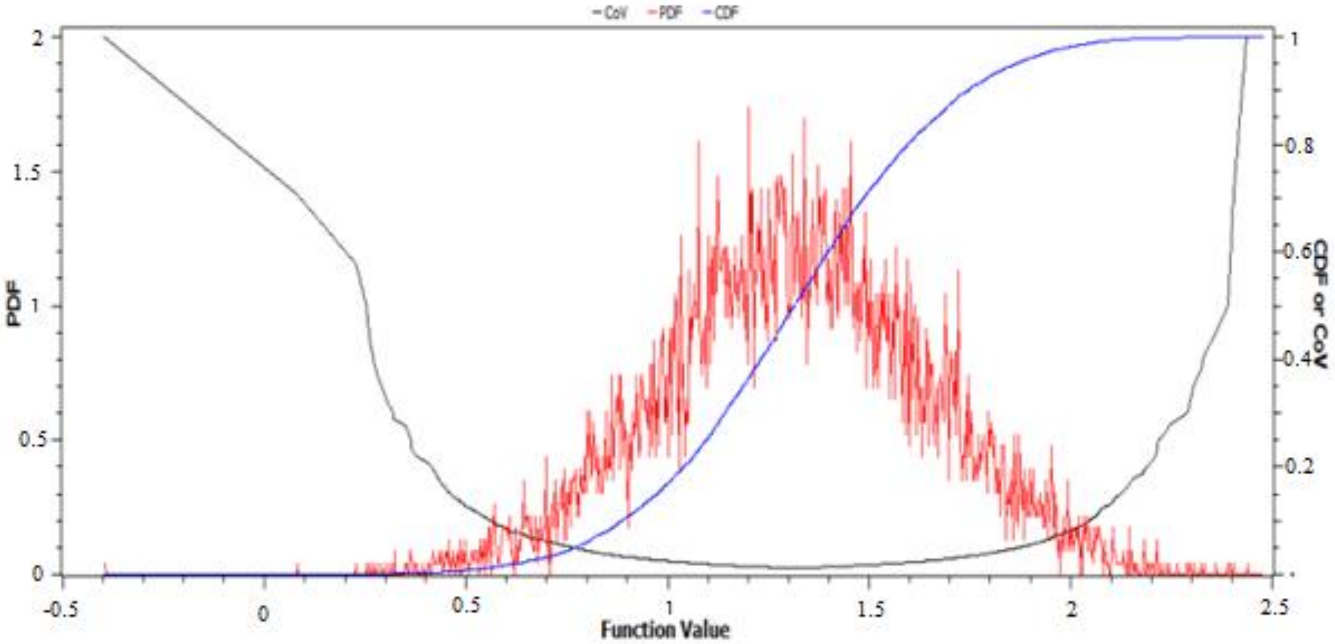

Figure 3. PDF, CDF and COV in sampling method

Table 3. β in FORM, FOSM, Sampling methods

Row	Methods	Soil Cover(mm)	β
1	FORM	800	-1.62
2	FORM	1000	3.826
3	FORM	1200	1.099
4	FORM	1400	1.583
5	FOSM	800	-1.64
6	FOSM	1000	3.915
7	FOSM	1200	1.107
8	FOSM	1400	1.59
9	Sampling	800	-0.92
10	Sampling	1000	3.54
11	Sampling	1200	0.93
12	Sampling	1400	1.348

In this paper, in order to evaluate the effect of soil cover as one of the ways of preventing buckling, the probability of failure of the South Pars Gas Field pipeline is investigated. Figure 4 demonstrates the probability of failure and the reliability index (β). As shown in the figure, the reliability index (β) movement of the sinus passes through and does not follow the linear relationship.

The submarine pipeline has an upheaval buckling if the vertical load on the pipeline is less than the force exerted inside the pipeline due to high pressure and high load. In Figure 5, the amount of load required to defeat the pipeline is certain.

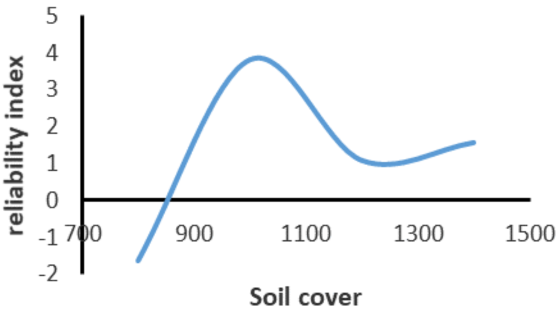

Figure 4. The effect of soil cover on reliability index (β) parameter

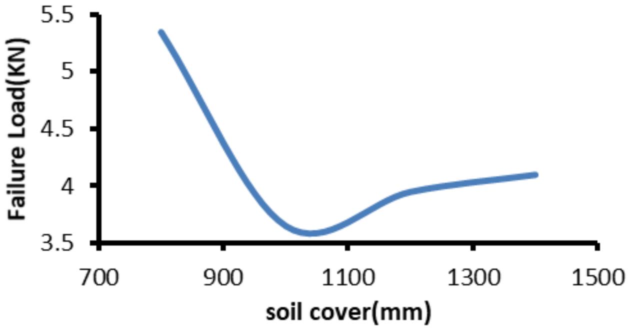

Figure 5. Load required to defeat the pipeline

According to Figure 5, it is concluded that before reaching the soil cover to 1000(mm) for the direct upheaval buckling of the pipeline, the trajectory of the pipeline is descending, and after passing through this amount, the Uptrend is, or in other words, for soil cover with a thickness of more than 1000, it is worth noting that by increasing the thickness of the soil cover, more force is required for the upheaval buckling in the pipeline.

6. Conclusions

The reliability index (β) movement of the sinus passes through and does not follow the linear relationship.

For soil cover with a thickness of more than 1000, it is worth noting that by increasing the thickness of the soil cover, more force is required for the upheaval buckling in the pipeline.

Sampling method due to several samplings has more accurate values offers and in the Sampling method, we have less β than another.

In order to calculate the failure of the pipeline due to upheaval buckling, three methods were used. Among these three methods, for a fixed condition, the sampling method was the lowest beta and the highest probability, which has a higher accuracy than the other available methods. And the least precision is also related to the FOSM method. It is also worth noting that the results are very close together and provide approximate estimates with respect to the approximation.

7. List of Symbols

E	Modulus of elasticity [GPa]
S_0	Effective axial compressive force, (compressive, –; tension, +)
Δp_i	Difference of internal pressure relative to laying condition.
ΔT_i	Difference between operating temperature and installation temperature
A_i	Internal bore area of the pipe
A_s	Cross-sectional area of the pipe
ϑ	Poisson’s ratio
α	Thermal expansion coefficient
$F_{residual}$	Residual lay tension
x	Horizontal distance
w_s	Pipeline submerged weight per unit length
δ	Height of the vertical imperfection
q	Downward load per unit length
L_0	Span length
P_f	Probability of failure
F_x	multivariate density function

8. References

1- Rezazadeh, K., Zhu, L., Bai, Y., and Zhang, L., (2010), *Fatigue Analysis of Multi-Spanning Subsea Pipeline*, 29th International Conference on Ocean, Offshore and Arctic Engineering, Vol.5, Parts A and B, p.805–812.

2- Karampour, H. and Albermani, F., (2014), *Experimental and numerical investigations of buckle interaction in subsea pipelines*, Eng.Struct.66, p.81–88.

3- Mustaffa, Z., (2011), *System Reliability Assessment of Offshore Pipelines*,PhD thesis, University of Delft.

4- Bai, Q. and Bai, Y.,(2014),*10 -Lateral Buckling and Pipeline Walking, in Subsea Pipeline Design, Analysis , and Installation*, Q. Bai and Y. Bai, Eds. Boston: Gulf Professional Publishing, p. 221–253.

5- Karampour, H., Albermani,F. and Gross, J., (2013),*On lateral and upheaval buckling of subsea pipelines*, Eng.Struct.52, p.317–330.

6- Guijt, J., (1990), *Upheaval buckling of offshore pipelines: overview and introduction*, Offshore Technology Conference, p. 573–580.

7- Liu, R., Wang, W.G., Yan, S.W. and Wu, X.L., (2012), *Engineering measures for preventingupheaval buckling of buried submarine pipelines.* Appl. Math. Mech. 33, p.781–796.

8- Wang, Z., Huachen, Z., Liu, H. and Bu, Y., (2015), *Static and dynamic analysis on upheavalbuckling of unburied subsea pipelines*, Ocean. Eng. 104, p.249–256.

9- Bai, Q. and Bai, Y., (2014),*11 - Upheaval Buckling, in Subsea Pipeline Design, Analysis, and Installation*, Q. Bai and Y. Bai, Eds. Boston: Gulf Professional Publishing, p.255–280.

10- Det Norske Veritas, (2013), *Submarine Pipeline Systems, DNV-OS-F101.*

11- Det Norske Veritas, (2013), *Global Buckling of Submarine Pipelines, Structural Design due to High Temperature/High Pressure*, DNV-RP-F110.

12- Rajeev, P., Robert, D.J., Thusyanthan, I. and Kodikara, J., (2013),Reliability analysis of upheaval bucking of offshore pipelines, Australian Geomechanics Journal, Vol.48, p.137-148.

13- Taheri, A., Shabani, M.H. and Daghigh, M., (2018), *Investigation of the Effect of Local Buckling and VIV Fatigue on FailureProbability of Subsea Pipelines in Iranian South Pars Gas Field*,ijmt, Vol.9, p.23-32.

14- Al-Sharif, A.M. and Preston, R., (1996), *Structural Reliability Assessment of the Oman India Pipeline*, OTC 8210, p.569-578.

15-Van den Abeele, F., Boël, F. and VandenBerghe, J.F., (2014), *Structural Reliability of Free Spanning Pipelines*, Vol.3: Materials and Joining; Risk and Reliability

16- BOMEL Limited, (2001), *Probabilistic Methods: Uses and Abuses in Structural Integrity, in Probabilistic methods: Uses and abuses in structural integrity*, no. 398/2001.

17- Kroese,D.P. and Rubinstein,R.Y., (2017) *Simulation and the Monte Carlo method*, Third ed.,John Wiley & Sons, Inc, Hoboken, New Jersey.

INTERNATIONAL JOURNAL OF
COASTAL & OFFSHORE ENGINEERING
IJCOE Vol.4/No. 4/ Winter 2019 (25-35)

Available online at: http://ijcoe.org/browse.php?a_code=A-10-92-1&sid=1&slc_lang=en

Optimized SMA Dampers in Vibration Control of Jacket-type Offshore Structures (Regular Waves)

Mohammad Reza Ghasemi[1*], Naser Shabakhty[2], Mohammad Hadi Enferadi[3]

[1*] *Professor, Department of Civil Engineering, University of Sistan and Baluchestan, Zahedan, Iran; mrghasemi@eng.usb.ac.ir*
[2] *Assistant Professor, School of Civil Engineering, Iran University of Science & Technology, Tehran, Iran, P.O.B. 16765-63; shabakhty@iust.ac.ir*
[3] *PhD Student, University of Sistan and Baluchestan, Zahedan, Iran; menferadi@pgs.usb.ac.ir*

ARTICLE INFO

Article History:
Received: 6 Dec. 2018
Accepted: 10 Mar. 2019

Keywords:
Vibration Control
Steel Jacket Platforms
Shape Memory Alloys (SMA)
Idealized Constitutive Model.

ABSTRACT

Undesired oscillations of jacket platform may influence the structural functionality and sometimes fatigue occurs. The main objective of this research is to control wave-induced vibrations of fixed jacket platforms with the use of optimized shape memory alloys dampers. To model the hysteretic behavior of SMA elements and performing dynamic analysis an efficient isothermal idealized constitutive model is developed in this research and direct integration time history analysis is carried out. Dynamic responses of multi-degree of freedom system of jacket platform, with 90 m height and equipped with SMA dampers, is estimated and compared with the bare jacket. Furthermore, an optimization algorithm such as Ideal Gas Molecules Movements (IGMM) is implemented in this research to improve the efficiency of the dampers and minimize the deck displacements under the action of extreme wave. The results show that the optimized SMA dampers can improve the structural response by decreasing 47.5 percent of deck displacement, 56.5 percent of deck acceleration and finally 28 percent of base shear. In an SMA damper-equipped platform, reduced wave intensity will reduce the damper efficiency.

1. Introduction

Undesired vibrations of offshore jacket platforms increase the destructive effects of fatigue in joints, risers, and mechanical equipment on the deck, disrupt the operations of the platform drilling equipment, reduce the personnel comfort feeling and endanger their long-term health by the deck's back-and-forth movements [1]. Hence, jacket platform vibrations should be reduced by control devices.

In recent decades, many smart materials have been invented to be used as energy dissipative devices. Shape memory alloys (SMAs) are materials investigated by researchers for use in aeronautics, automobile, biomedical engineering, and civil engineering, especially vibration control of structures [2]. The main objective of this research is to present an efficient SMA damper to control the vibrations of a jacket platform under the wave and current actions.

Vibration control of offshore structures is much more difficult than that of land based structures because the former should withstand the wave-caused force besides wind and earthquake. Since inspection, repair, and replacement of in-depth dampers are quite costly, it is necessary to use those that are highly durable and do not undergo permanent deformations under relatively large loads. A feature of SMA dampers is their lack of need for replacement or repair after lateral loads and large deformations in jacket platforms of which underwater repair and inspection are difficult.

Vandiver and Mitome [3] were among the early researchers who studied controlling the offshore jacket platforms vibrations and found that liquid-reservoirs on the platform deck can be used as the dynamic absorber. Bargi et al. too have been able to reduce the vibrations of the offshore wind turbine using tuned liquid column gas damper. Their research is all-inclusive because they controlled the vibrations under the simultaneous effects of wind, wave, and earthquake forces [4] [5].

Patil and Jungid [6], analyzed three jacket structures equipped with friction dampers, viscose dampers, and viscoelastic dampers under the action of wave forces. They have concluded that the friction damper is quite efficient in reducing deck displacements and shear forces of jacket levels.

Investigation of dampers' performances and improving the platform dynamic behavior has been a topic of interest of Jafarabad, Kashani, Adlparvar and Golafshani, [7]. They have compared the performance of friction damper and tuned mass damper (TMD) as hybrid dampers aiming at improving the platform dynamic responses under seismic and wave loads.

In offshore structures, as well as land-based structures, isolating the platform and deck is considered as a suitable way to control the vibrations. In the recent study, Zhang has used hybrid SMA-PFD (pall friction damper) dampers to reduce the deck displacement due to seismic and ice-induced excitation [8].

Since passive dampers used on jacket platforms often work for a limited loading range, many researchers have used active and semi-active dampers to control the jacket platform vibrations [9]. Another merit of the SMA dampers is that their stiffness can be adjusted by a source of heat [10].

In this research, some SMA material features are presented in Section 2. The implementation of SMA elements, the structure of SMA damper and dampers installation in the jacket platform are explained in Section 3. In Section 4, first, the vibration equation of un-damped multi-degree of freedom system equipped with SMA dampers is developed. Then, a multi-linear formulation has been presented to develop the constitutive material modeling of the SMA elements. In this research, the linear time history responses of equipped-SMA dampers structure have been estimated using the implicit direct integration alpha-method by MATLAB based computer code [11]. Therefore, at the end of this section, two comparisons are made with reference research and finite element analysis to validate the constitutive modeling of SMA and dynamic responses of jacket platform.

In Section 5, a 90 m height jacket platform is selected as a case study and vibrated under the action of extreme regular wave with 11.8 m height and 7.8 s period. In this section, dynamic properties of MDOF system of jacket platform, dynamic characteristics of wave/current loads and SMA mechanical properties are presented first. Then, an optimization algorithm 'ideal gas molecules movements' (IGMM) is used to find optimal characteristics of SMA elements geometry based on two different objective functions [12]. Finally, numerical results of installing optimized SMA dampers to jacket platform are presented and discussed. At the end of Sec. 5, an offshore platform equipped with optimized dampers has been acted by two other regular waves and the dampers have been studied for their efficiency.

In Section 6, the results of optimized SMA dampers usage in vibration reduction of jacket platform and some recommendations for future studies, are presented.

2. Shape Memory Alloys (SMAs)

Shape memory alloys (SMA) are a class of smart materials that possess unique properties, including shape memory effect (SME), super-elasticity effect (SE), extraordinary fatigue and corrosion resistance and high damping capacity. The shape memory effect of nickel-titanium alloy was recognized by William Buehler and Frederick Wang in 1962. The alloy was named as NiTinol (NiTi stands for nickel-titanium and nol is naval ordnance laboratory).

Micromechanical phase transitions take place during deformation and/or temperature processes, when the SMA crystallographic structure switches from an austenitic phase to a martensitic phase (Figures 1 and 2). Martensite phase of SMA may appear in detwinned arrangement or twinned arrangement. At low temperatures ($T<M_f$), SMAs exhibit the shape memory effect (Figure 1). While, at high temperature ($T > A_f$), SMAs show super-elastic behavior, during loading and unloading steps (Figure 2). At the temperature above (M_d), SMAs suffer plastic deformations with much higher strength in their pure austenitic form.

The mechanical behavior dependence on stress, strain, and the temperature is because of the SMAs' thermo-elastic nature which increases the temperature to decrease the stress in the material. SMAs are primarily austenitic in the super-elastic phase. However, upon loading, stress-induced martensite is formed. Upon unloading, the martensite reverts to austenite at a lower stress level, resulting in the hysteretic behavior [13].

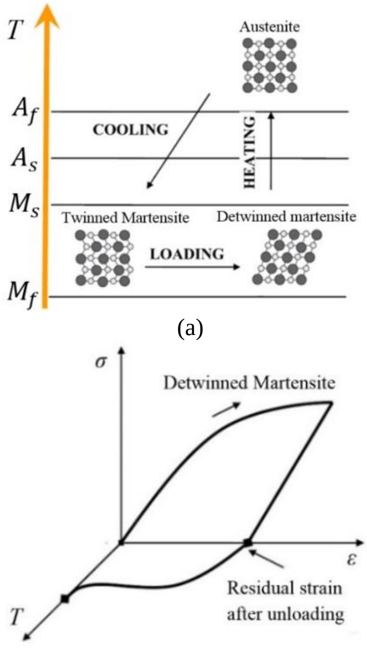

(a)

(b)

Figure 1. SMAs shape memory effect (SME) [13]; (a): crystal arrangement due to changes in loading and heating, (b): SMA's stress-strain-temperature curve

SMAs are excellent candidates for designing dampers and energy dissipation devices because of their intrinsic ability to undergo large deformations, up to 10% without remaining residual strain [14]. SMA materials have numerous combinations such as Ni–Ti, Cu–Al–Ni, Cu–Zn–Al, Au–Cd, Mn–Cu, Ni–Mn–Ga and Fe-based alloys, but most practical ones are Ni–Ti-based alloys [15].

With numerous SMA applications in different fields over the past decades, material modeling of such SMAs peculiar mechanical behavior has been a subject of interest to many researchers. The studies on SMA's behaviors were lead to the development of many constitutive models that describe the thermo-mechanical, thermo-electrical and thermo-chemical behavior; nonetheless, most of them are too complicated to be conveniently used in such practical applications as vibration control problems.

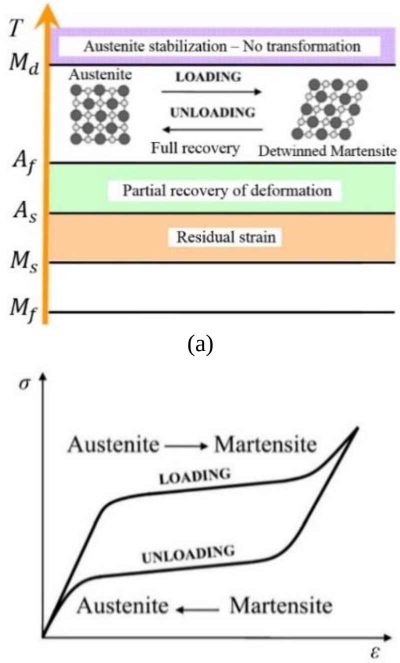

(a)

(b)

Figure 2. SMAs supper elasticity effect (SE) [13]; (a): SMAs crystal arrangement due to loading and unloading, (b): SMAs' stress-strain hysteresis loop

In structural vibration control field, widely used constitutive models for one dimentional isothermal superelastic SMAs can be mainly divided into polynomial constitutive model, idealized multi-linear constitutive model and equivalent linear elastic-viscous damping model. Polynomial constitutive material modeling of SMAs initially developed by Graesser and Cozzarelli (1991), is a development of a rate-independent model for hysteretic behavior proposed by Ozdemir. Differences between hysteresis loops obtained from the polynomial equations and lab results made researchers present more precise constitutive models to express the SMA force-displacement behavior. A highly applicable model is the one presented by Wilde et al. (known also as the modified Graesser-Cozzarelli (2000) model) [16].

In many SMA-based dampers, use is made of idealized constitutive models proposed by Auricchio for faster and simpler analysis. He suggested that a super-elastic SMA-based damper's force-displacement relationship that defines a nonlinear hysteretic model can be expressed as an idealized multi-linear hysteresis loop [17] [18]. The third method of modeling the hysteretic behavior of the SMA-based damper is the transformation of the nonlinear SMA hysteresis loops to equivalent linear elastic stiffness and viscous damping model [19]. So, the damper nonlinear force-displacement behavior can be replaced by an equivalent linear model that has two parameters, namely the effective elastic stiffness and effective viscous damping. In this research, an efficient multi-linear constitutive model has been implemented that will be explained and verified in the following sections.

Research activities of SMAs' applications in civil structures and implementation for field applications found effective [20]. Energy dissipation system and ground isolation system are the two widely used mechanisms by which SMAs could be utilized in an effective manner for the purpose of passive control technique.

3. SMA Damper

In this research, the proposed SMA damper shown in Figure 3 is housed by the extra rigid bracing system (Figure 4).

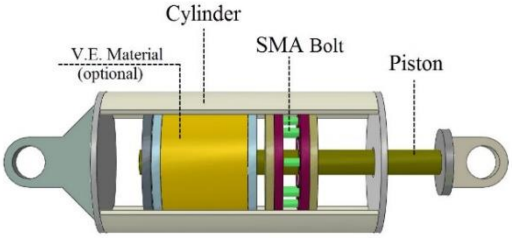

Figure 3. Schematic design of the proposed SMA damper

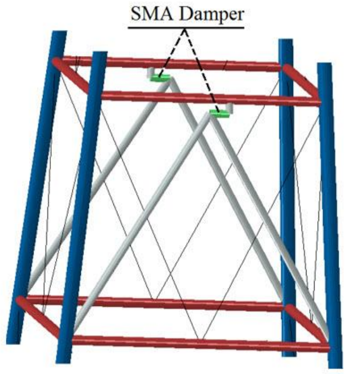

Figure 4. Connection of SMA damper with the jacket platform

As shown in Figure 3, the damper performance is such that SMA bars operate in tension and their buckling limitations are omitted under the piston strokes. In such dampers, the piston stiffness is large enough and its strain is negligible in comparison with SMAs strain. Therefore, the piston stroke is equal to SMA bars deformation, and the damper restoring force is the same as that of the SMAs.

Considering the inherent characteristics of SMA elements, it can be concluded that SMA dampers are quite appropriate options to control the vibrations of jacket platforms. These intrinsic features that distinguish them from other dampers and justify their use in controlling such vibrations are:

- SMAs are quite versatile and have different ductility and damping capabilities; therefore, the versatility of dampers designed with them can be very large too.
- Fabrication of many dampers and vibration control devices is often monopolized by certain companies and they are quite expensive. The advantage of the SMA damper is that if its elements are provided, its other parts can be made and assembled in smithies.
- SMA elements, especially the NiTinol alloys, possess high thermal stability and corrosion resistance and have high ductility and very good fatigue performance; therefore, their use is highly recommended in offshore structures with a condition of large amplitude oscillations and corrosive environments.
- The SMA's elastic modulus is a function temperature; hence, a heat producing source can set its bar stiffness desirably; this feature can be used in the design of active and semi-active dampers.

4. Method and Verification

4.1. Dynamic Formulations

In this research, the responses of the dynamic equations and advanced analytical algorithms of the constitutive modeling of the superelastic SMA have been estimated by a computational MATLAB based computer code wherein use is generally made of the idealized constitutive model. In the developed code, the linear time history analysis is done on a jacket platform structure modeled as a multi-degree of freedom (MDOF) system and equipped with the SMA dampers (Figure 5). The vibration equation of MDOF system and SMA dampers is as follows:

$$[\boldsymbol{M}]\{\ddot{\boldsymbol{v}}\} + [\boldsymbol{K}]\{\boldsymbol{v}\} + \{\boldsymbol{F_{SMA}}\} = \{\boldsymbol{F_{w,c}}\} \tag{1}$$

In Eq. (1), matrices $[\boldsymbol{M}]$ and $[\boldsymbol{K}]$ are mass and stiffness matrices of the jacket structure, and $\{\ddot{\boldsymbol{v}}\}$, $\{\dot{\boldsymbol{v}}\}$ and $\{\boldsymbol{v}\}$ are the acceleration, velocity and displacement vectors, respectively. Vector $\{\boldsymbol{F_{SMA}}\}$ is SMA dampers restoring forces and will be explained in Section 3 and vector $\{\boldsymbol{F_{w,c}}\}$ is the wave and current forces. Due to the object of this research, in vibration control of jacket platform through optimized SMA dampers, structural damping is ignored.

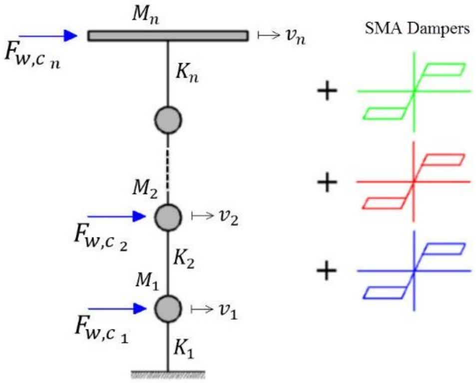

Figure 5. Multi degree of freedom system of Jacket platform equipped with SMA dampers

In this research, the Morison equation is used to estimate the wave and current loads acting on jacket members [21]. This equation is originally developed to compute hydrodynamic forces acting on a vertical cylinder and is given by the following expression.

$$F(z,t) = \rho\,\pi\,\frac{D^2}{4}\,C_m\,\ddot{u}(z,t) + \cdots \cdots \frac{1}{2}\,\rho\,D\,C_d\,|\dot{u}(z,t)|\,\dot{u}(z,t) \tag{2}$$

In Eq. (2), function $F(z,t)$ is the in-line force per unit length acting on the submerged section at position z from the mean water level. Functions $\ddot{u}(z,t)$ and $\dot{u}(z,t)$ are the relative wave acceleration and velocity and can be calculated by the wave theory. Parameter ρ is the density of water usually considered as 1030 kg/m^3. Parameters D, C_m and C_d are cylinder outer diameter, inertia coefficient, and drag coefficient, respectively [22].

4.2. SMAs Constitutive Model

For solving differential equations of the motion presented in Eq. (1), the direct HHT integration method has been implemented. Vector $\{F_{SMA}\}$ is the most important term of Eq. (1), which defines the SMA damper restoring force.

As stated in Sec. 3, in the dynamic analyses, the set of the damper's piston, cylinder, and supports are assumed to be rigid and the total section area of the SMA bolts of each damper is equivalent to that of a 2-DOF axial member the end displacements of which equal those of the platform's lower and upper levels.

Numerical methods of solving vibration differential equations (alpha-method) calculate the structural dynamic responses by integrating in time intervals. Therefore, it is possible, at any forward step, to calculate the changes in the damper force and add it to the one in the previous step.

The SMAs one-dimensional isothermal idealized linear force-displacement constitutive model is shown in Figure 6. In the j^{th} step and due to x_j piston displacement, the damper restoring force $F_{sh\ j}$ can be estimated with the following expressions.

$$x_j \le x_f^{MA}$$
$$F_{sh\ j} = F_{sh\ j-1} + k_1\left(x_j - x_{j-1}\right) \quad (3)$$

$$x_f^{MA} < x_j < x_f^{AM}$$
$$F_{sh\ j} = F_{sh\ j-1} + k_1\left(x_j - x_{j-1}\right) \quad (4)$$

IF: $F_{sh\ j} >$ Upper Plateau
$$F_{sh\ j} = A \times \sigma_s^{AM} + k_2\left(x_j - x_s^{AM}\right) \quad (4a)$$

IF: $F_{sh\ j} <$ Lower Plateau
$$F_{sh\ j} = A \times \sigma_f^{MA} + k_3\left(x_j - x_f^{MA}\right) \quad (4b)$$

$$x_f^{AM} \le x_j$$
$$F_{sh\ j} = F_{sh\ j-1} + k_1\left(x_j - x_{j-1}\right) \quad (5)$$

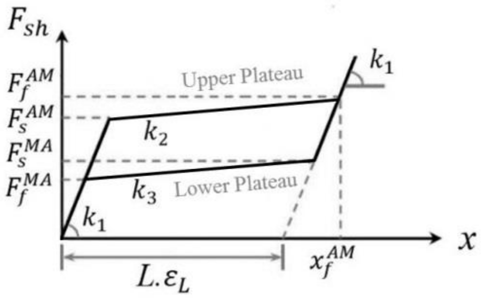

Figure 6. SMAs One-dimensional isothermal constitutive model

Where A, k_1, k_2 and k_3 are SMA bars total section areas, axial stiffness in the elastic region, axial stiffness in the austenite to martensite phase transition stage and axial stiffness in the martensite to austenite phase transition stage, respectively. In x (or ε), F and σ superscript AM stands for the austenite to martensite phase transition and MA stands for the martensite to austenite case. Again, subscript s stands for the starting of the phase transition and f stands for its finishing. Axial stiffness of SMA bars can be estimated through Eqs. (6 to 8).

$$k_1 = \frac{A}{L} \times E_{SMA} \quad (6)$$

$$k_2 = \frac{A}{L} \times \frac{\sigma_f^{AM} - \sigma_s^{AM}}{\varepsilon_f^{AM} - \varepsilon_s^{AM}} \quad (7)$$

$$k_3 = \frac{A \times (\sigma_s^{MA} - \sigma_f^{MA})}{x_j - x_f^{MA}} \quad (8)$$

Parameters L, E_{SMA} and ε_L are the length of SMA bars, the initial modulus of elasticity and full phase transition strain, respectively. The advantage of the above mentioned idealized constitutive model of the SMA element is that it does not need to know the $\dot{x}$ (velocity) information to determine the F_{sh}. As a result, the speed of analysis is increased without causing any changes in the dynamic responses.

4.3. Verifications

The MATLAB code developed in this study has two main output groups: 1) structural time history responses and 2) the SMAs hysteresis loops. To ensure their correctness and accuracy, two different validations have been made.

In comprehensive research, Asgarian and Moradi placed an SMA bar member under the quasi-static deformation loading and found its stress-strain hysteresis loops [23]. Therefore, for the first validation, a comparison has been made between the outputs of the SMA hysteresis loops calculated by MATLAB and the results of Asgarian and Moradi analysis. The SMA hysteresis loops presented in Figure 7 show that the results exactly coincide.

For the second validation, a steel jacket platform modeled as a 5-DOF system has been analyzed by the MATLAB code and the finite element analysis (ABAQUS). In the three dimensional ABAQUS model of the jacket, all the members considered as beam element (B32). The jacket platform geometrical and mechanical characteristics, wave dynamic properties and other considerations are explained in the next section (Section 5). Comparison of the dynamic responses shown in Figure 8, confirm an acceptable precision of developed MATLAB code.

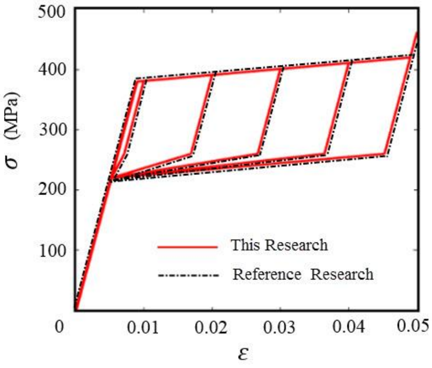

Figure 7. SMA stress-strain hysteresis loops by MATLAB based computer code (this research) and reference research [23]

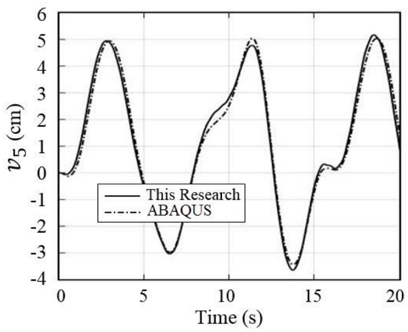

Figure 8. Time history deck displacement responses (v_5) of steel jacket platform with MATLAB based computer code (this research) and finite element analysis (ABAQUS)

5. Case Study

5.1. MDOF system characteristics

To perform the final analysis and obtain the efficiency of SMA dampers in vibration control, a steel jacket platform has been selected as a case study. These types of platforms are quite common and are even similar to real ones [24]. The total height of the structure is 90 m and is symmetrical in the plan. The Jacket has 4 legs and its dimensions on the sea floor and deck level are 32 m × 32 m and 20 m × 20 m, respectively. The deck's total dead and live load is 4800 tons. To take into account the effects of the soil-pile interaction, use has been made of the column-base clamping rule at a height equivalent to 8 times the pile's diameter [25]. The elevation view of the jacket is shown in Figure 9 and geometrical and mechanical specifications of the members are presented in Table 1.

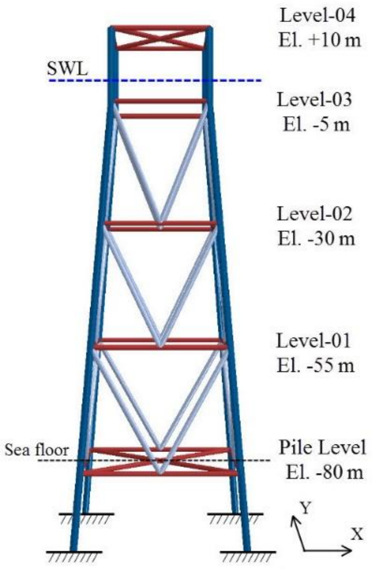

gure 9. Elevation view of steel jacket platform [24]

Table 1. Mechanical and geometrical characteristics of jacket platform members

Mechanical		
Steel modulus of elasticity		200 GPa
Poisson's ratio		0.3
Yield stress		320 MPa
Ultimate stress		405 MPa
Mass of the deck		4800 ton
Steel density		7800 kg/m^3
Geometrical		
	Diameter (mm)	Thickness (mm)
Horizontal bracings	1000	12
Vertical bracings	1100	12
Legs	1500	25

Dynamic characteristics of waves and current velocity have been so selected that the platform can have relatively large displacements under wave loads and, at the same time, may not enter its nonlinear region. Jacket platform members' entering the nonlinear region and experiencing large deformations will cause damage to drilling equipment, risers, and the related structural connections. Therefore, to analyze the SMA dampers' effects on the jacket platform vibrations, an extreme wave 11.8m high and 7.8sec period has been considered. The water depth, wave height, its period, and in-depth current velocity have been shown in Table 2.

To calculate the wave and current forces acting on the jacket members, the inertia and drag coefficients of the Morison equation (Eq. (2)), are 2.0 and 0.8 (constant in depth), respectively [7]. To estimate the wave acceleration and velocity, the 5th order stokes theory was selected after checking the wave theory validation. In this research, a side plan has been developed where the platform members are divided into 20 elements. The wave velocity and acceleration are calculated at the elements' beginning and end joints where the wave horizontal velocity is added to that of the current (current velocity variation in depth is considered linear). The forces applied on the elements are assembled and finally transferred to the members' beginning and end joints. Therefore, the force applied to each degree of freedom is the sum of the current and wave forces acting on the horizontal beams and half of the member forces above and below the beams. Regarding Eq. (1), the dynamic characteristics of the 5-DOF system of jacket platform are shown in Table 3.

Table 2. Wave and current dynamic characteristics

Wave Dynamic Characteristics	
Water depth	80 m
Wave height	11.8 m
Mean period	7.8 second
Current speed, Storm generated, Tides included	
Near surface	0.83 m/s
Middle depth	0.27 m/s
Near bottom	0.16 m/s

Table 3. Dynamic characteristics of 5-DOF system of jacket platform

	Level Pile	Level 01	Level 02	Level 03	Level 04
Mass (ton)	220	200	195	130	4850
Stiffness (MN/m)	90	350	210	115	42
$F_{w,c}$* (kN)	28.615	133.35	529.27	825.82	111.23

*Maximum amplitude of wave and current forces.

As shown in Fig. 9, each of the platform's peripheral frames has four vertical levels. The SMA dampers have been installed in the 1st, 2nd, 3rd and 4th levels through rigid link supports (Figure 4). To control the platform's vibrations along the x and y axes, it is necessary to have 8 dampers along each (totally 16). The mechanical properties used for SMA, based on DesRoches studies in 2004 [26], are presented in Table 4. Next, the lengths of each damper's SMA bolts and their required total section area will be found through optimization analyses.

Table 4. Mechanical properties of SMA [26]

	E_{SMA}	ε_L	σ_s^{AM}	σ_f^{AM}	σ_s^{MA}	σ_f^{MA}
Values	55	6	420	520	310	240
Units	GPa	%	MPa	MPa	MPa	MPa

5.2. Optimization Analysis

Stiffness and damping are the two main characteristics of an SMA damper and have significant effects on the dissipation of the applied energy and damping efficiency. Hence, bars lengths and areas should be so selected that: 1) the alloy phase transmission from austenite to martensite is achieved and 2) deck displacements are reduced.

To achieve the platform's optimal dynamic responses, use has been made of the 'ideal gas molecule movement' optimization algorithm presented by Varaee and Ghasemi in 2017 [27]) which is a new, efficient, population-based and intelligent algorithm and uses the principles and relationships that govern the molecular movement of ideal gases for optimization. This algorithm offers excellent precision and speed in complicated, single/multi-objective optimization problems.

Here, the potential solutions of an optimization problem could be considered equivalent to the gas molecules that are moving and exploring in their chamber i.e. the problem space. The behavioral properties of the gas molecules allow them to rapidly spread throughout the chamber and navigate and search all potential spaces for optimal solutions. During their movement in the problem space, these molecules collide with one another with a certain probability due to which they interact and exchange information. Such information exchange is reflected in the molecules' velocity variations after they collide and position in a new position at different time steps. Those molecules that do not enter the collision process at any time step, will participate in the general problem search space as free molecules and increase the chance of exploring new spaces and finding suitable solutions. Now, if the information on motions and molecular collisions is used properly (i.e. in the form of an algorithm), it is possible to find the optimal range during these surveys and collisions. The design variables and constraints can be defined after checking how the optimization algorithm operates.

Design variables:
1) L
2) A

Constraints:
1) $L \geq 40$ mm
2) $x_{max} \leq x_f^{AM}$

Parameters L, A, and x_f^{AM} are the SMAs length, SMAs area, and austenite to martensite finish displacement, respectively.

The main objectives of the optimization of the proposed SMA damper are to minimize the displacements of the deck, reduce the tensions in the jacket members and reduce the SMA's volume. An SMA damper has both the elastic and damping properties and if the length and area of its SMA alloys are not selected correctly, the damper elasticity may increase and its dissipation capability may decrease. Since the objective functions of this problem cannot be determined easily, optimization has been done based on two different objective functions.

Objective functions:
1. Minimizing v_5
2. Maximizing $A_{hysteresis\ loops}$

Parameters v_5 and $A_{hysteresis\ loops}$ are the displacement of the deck and total area under hysteresis loops of all dampers, respectively. To find the optimal solution, the maximum number of the optimization process cycles (N) and the number of molecules per cycle have been considered to be 100 and 20, respectively. Figures 10, and 11 show the values of each selected objective function and SMA bars total volume calculated in each optimization iteration.

Figure 10 shows the problem optimization solution with the objective of minimizing the deck displacements. As shown, the IGMM method has been able to converge to a displacement of 2.82 cm after 65 cycles (1300 analysis). Figure 11 show the problem optimization solution with the objective of maximizing the area under hysteresis loops of all dampers.

The optimized SMAs geometrical characteristics are presented in Table 5. The SMA dampers are classified to "Design 1" (based on minimizing v_5 objective function) and "Design 2" (based on maximizing $A_{hysteresis\ loops}$ objective function).

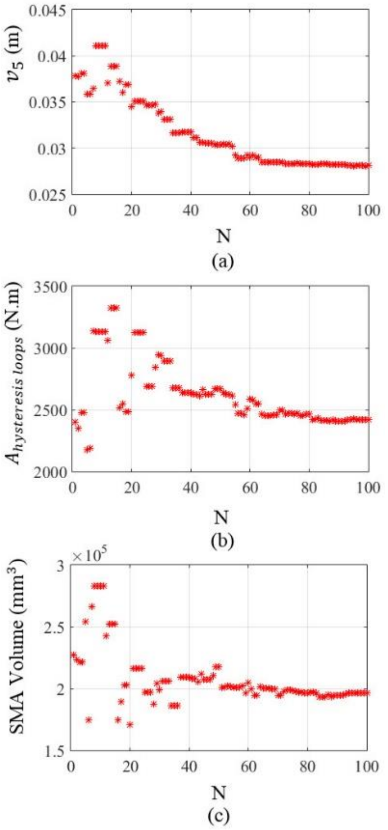

Figure 10. Optimization results based on "minimizing v_5" objective function; (a): v_5 (deck displacement), (b): $A_{hysteresis\ loops}$, (c): SMA bars total volume

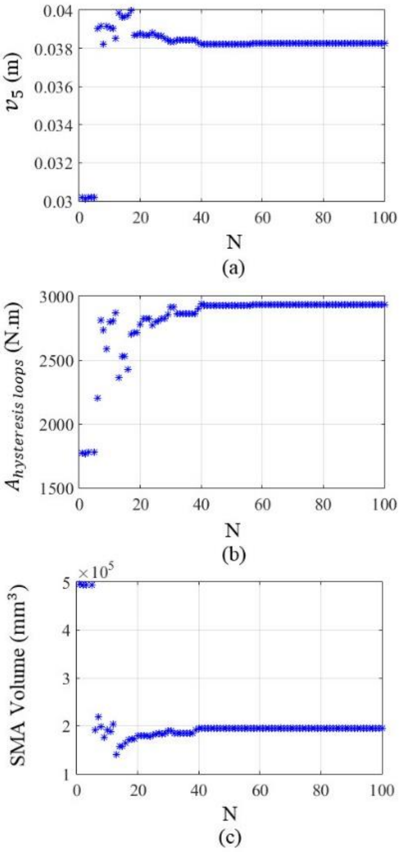

Figure 11. Optimization results based on "maximizing $A_{hysteresis\ loops}$" objective function; (a): v_5 (deck displacement), (b): $A_{hysteresis\ loops}$, (c): SMA bars total volume

Table 5. SMA bars geometrical characteristics based on optimization analysis

	Objective Functions			
	Minimize v_5		Maximize $A_{hysteresis\ loops}$	
	"Design 1"		"Design 2"	
	A (mm^2)	L (mm)	A (mm^2)	L (mm)
Level-04	370	40	100	96
Level-03	1300	40	530	103
Level-02	1890	40	1220	65
Level-01	1360	40	1150	45

5.3. Numerical Results and discussions

The optimization analysis results, based on two mentioned objective functions, and dynamic responses of the jacket platform equipped with optimized dampers are presented in Table 6. As is clear, optimization analysis with minimizing v_5 objective function has acceptable results in minimizing deck displacements.

Table 6. Results of optimization analysis and jacket platform dynamic responses

	Objective Functions	
	Minimize v_5	Maximize $A_{hysteresis\ loops}$
v_5 (mm)	28.1	37.8
$A_{hysteresis\ loops}$ (N.m)	2420	2935
SMA volume (mm^3)	196430	194600
$\ddot{v}_5$ (mm.s^{-2})	59.6	57
Level-01 shear force* (kN)	1644	1720

* Base shear

The time history dynamic responses of jacket platform equipped "Design 1" SMA dampers are displayed in Figures 12 and 13. The results indicate that optimized SMA dampers have significant effects on vibration suppression of jacket platform.

The maximum reduction in the jacket structure dynamic responses and comparison of the two controlled and uncontrolled platform states are presented in Table 7. As is clear, installing "Design 1" SMA dampers on the steel jacket platform can reduce deck displacement and deck acceleration by 47.5 and 56.5 percent, respectively. Furthermore, dampers high efficiency in the dissipation of wave's energy entry to the jacket structure, cause 59 and 28 percent reduction in level-04 and level-01 shear forces, respectively.

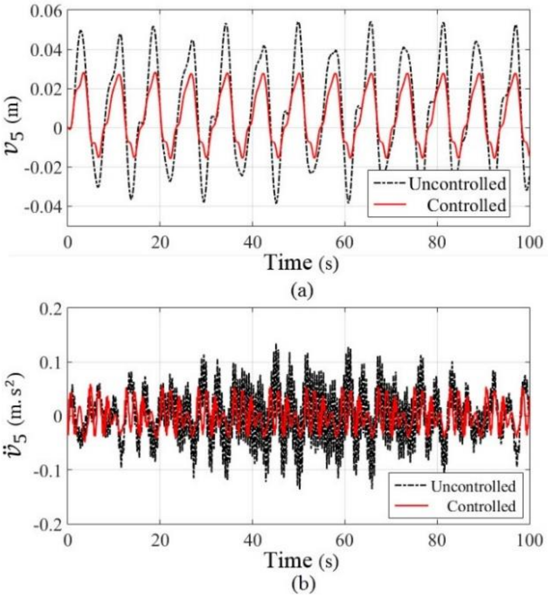

(a)

(b)

Figure 12. Time history responses of the controlled (with "Design 1" dampers) and uncontrolled states; (a): v_5 (deck displacement), (b): $\ddot{v}_5$ (deck acceleration)

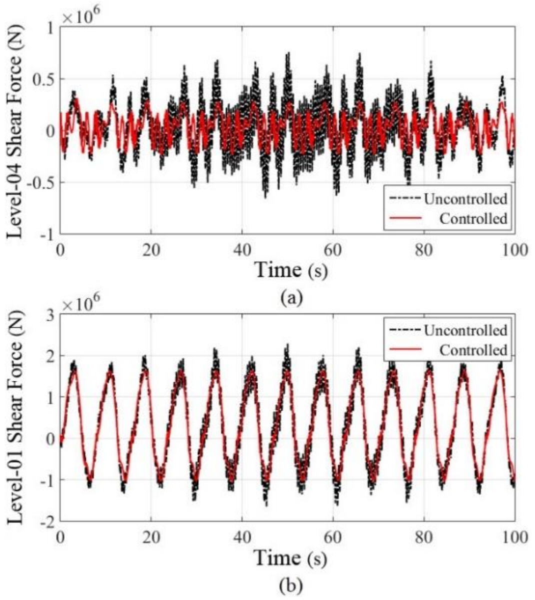

(a)

(b)

Figure 13. Time history responses in the controlled (with "Design 1" dampers) and uncontrolled states; (a): level-04 shear force, (b): level-01 shear force (base shear)

Table 7. Maximum dynamic responses of controlled (design 1 dampers) and uncontrolled jacket platform

	Uncontrolled	Controlled	Reduction
v_5 (mm)	54	28.3	47.5 %
$\ddot{v}_5$ (mm.s^{-2})	136.5	59.6	56.5 %
Level-04 shear force (kN)	755.5	311.6	59 %
Level-01 shear force (kN)	2290.6	1644	28 %

According to the performed optimization analysis and dynamic responses of equipped-SMA dampers jacket platform, the following results could be achieved:

1. In comparison with the uncontrolled jacket platform, both mentioned optimization analysis has significant effects on deck acceleration and base shear (Level-01) suppression (Tables 6 and 7).
2. In the above two optimized cases, the differences between deck displacements are significant and the difference between SMA bars total volume is negligible. Therefore, it can be concluded that the optimization of minimizing deck displacement, according to mentioned constraints, has had acceptable results (Table 6).
3. To perform a more realistic comparison, the hysteresis loops of optimized SMA dampers are shown in Figures 14 and 15. Maximum restoring forces of "Design 2" dampers are less than "Design 1" dampers and make them easier to install on the jacket platforms. This characteristic is of great importance in retrofitting projects of aging jacket platforms.

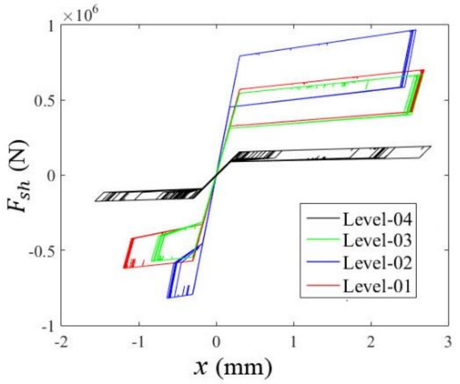

Figure 14. Hysteresis loops of "Design 1" SMA dampers

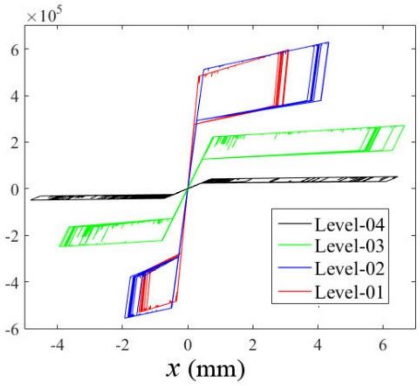

Figure 15. Hysteresis loops of "Design 2" SMA dampers

4. Hysteresis loops of optimized SMA dampers shown in Figures 14 and 15, indicate that SMAs displacements did not reach to x_f^{AM}. Hence, full phase transition from austenite to martensite does not lead to optimum responses.

5.4. Different Sea States

To check the efficiency of the optimized SMA dampers in Table 5 ("Design 1" dampers), the platform was placed under two other regular waves the dynamic characteristics of which are; Case I: wave height 10 m, wave period 7.3 s and Case II: wave height 8.4 m, wave period 6.8 sec and the water current velocity is the same given in Table 2. Compared to the initial selected wave, these two waves are less intense and cause less displacement in the platform deck and vertical levels. Figures 16 and 17 show the dynamic responses of the deck displacements and SMA dampers hysteresis loops in the controlled and uncontrolled state.

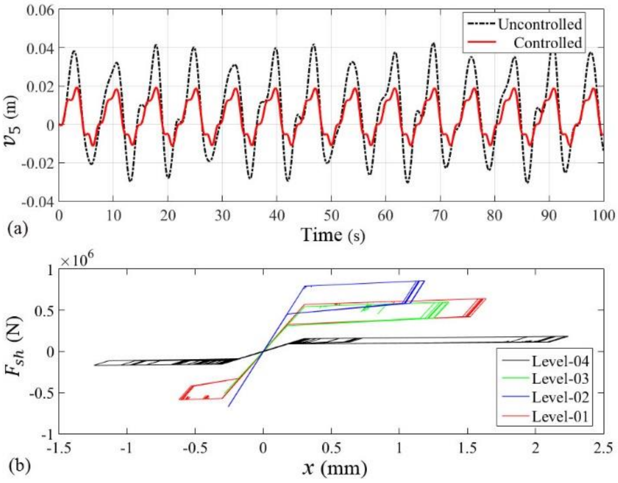

Figure 16. Dynamic response of jacket platform in controlled and uncontrolled state (Case I); (a): Deck displacements, (b): SMA dampers hysteresis loops

As shown in Figure 17, SMA dampers of level-02 and level-03, work linear with zero area in their hysteresis behavior. Decrease in the wave energy decreases the jacket drifts and hence the SMA dampers phase transition does not occur. To eliminate this limitation, use can be made of semi-active dampers capable of adjusting the stiffness of the SMA bolts.

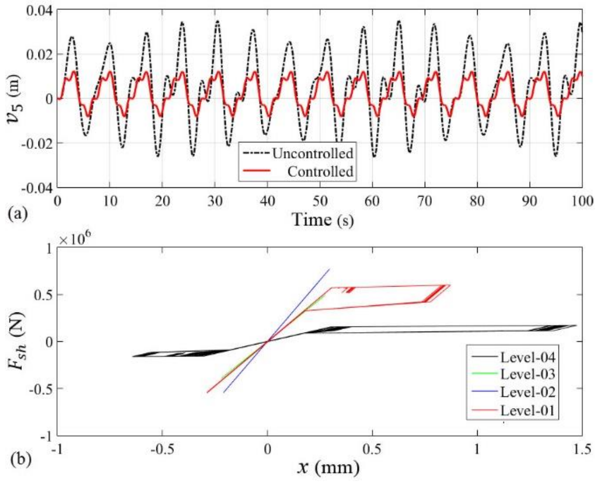

Figure 17. Dynamic response of jacket platform in controlled and uncontrolled state (Case II); (a): Deck displacements, (b): SMA dampers hysteresis loops

6. Conclusions

In this study, effort has been made to evaluate the effects of mounting optimized SMA dampers on the improvement of the dynamic behavior of no-damper jacket platforms under the action of regular sea waves. As a case study analysis, the dynamic responses of a 90 m height jacket platform equipped with SMA dampers and modeled as an equal 5-DOF system has been carried out.

To optimize the SMA elements geometry and obtaining the optimum dynamic responses of jacket platform under the action of extreme wave, an optimization analysis was done with two different objective functions. In the optimization analysis performed with the IGMM algorithm, the best results ("Design 1" SMA dampers) were obtained with use of the "deck displacements minimization" objective function. Although, joining optimized "Design 1" SMA dampers to jacket platform caused a significant reduction in deck displacement by 47.5 percent, deck acceleration by 56.5 percent and base shear of the structure by 28 percent, these two important results were obtained:

- SMA dampers hysteretic behavior was unsymmetrical in two states of tension and compression. Hysteresis loops area in the negative region was much less than positive region. Therefore, in the opposite direction of sea wave, an appropriate energy dissipation didn't occur in platform oscillations.
- In jacket platforms equipped with optimized SMA dampers, a decrease in the wave intensity will decrease the damper efficiency. Therefore, it is proposed to use active or semi-active SMA dampers with tunable stiffness SMA elements in the vibration suppression of jacket platforms induced by different waves and sea states.

7. References

1. Gupta, S., Shabakhty, N., VanGelder, P., (2006), *Fatigue damage in randomly vibrating Jack-up platforms under non-Gaussian loads*, Applied Ocean Research, Vol. 28(6), p. 407-419.

2. Song, G, Ma, N., Li, H.N., (2006), *Applications of shape memory alloys in civil structures*, Engineering Structures, Vol. 28, p. 1266–1274.

3. Vandiver, J.K., Mitome, S., (1979), *Effect of liquid storage tanks on the dynamic response of offshore platforms*, Applied Ocean Research, Vol. 1(2), p. 67-74.

4. Bargi, K., Dezvareh, R., Mousavi S.A., (2016), *Contribution of tuned liquid column gas dampers to the performance of offshore wind turbines under ind, wave, and seismic excitations*, EARTHQUAKE ENGINEERING AND ENGINEERING VIBRATION, Vol. 15(3), p. 551-556.

5. Dezvareh, R., Bargi, K., Mousavi, S.A., 2016. *Control of wind/wave-induced vibrations of jacket-type offshore wind turbines through tuned liquid column gas dampers*, Structure and Infrastructure Engineering, Vol. 12(3), p. 312-326.

6. Patil, K.C., Jungid, R.S., (2005), *Passive control of offshore jacket platforms*, Ocean Engineering, Vol. 32, p. 1933–1949.
7. Jafarabad, A., Kashani, M., Adlparvar, M.R., Golafshani, A.A., (2014), *Hybrid damping systems in offshore jacket platforms with float-over deck*, Journal of Constructional Steel Research, Vol. 98, p. 178-187, 2014.
8. Jigang, Z., Zhehao, M., Feifei, L., Chunwei, Z., (2017), *Seismic performance and ice-induced vibration control of offshore platform structures based on the ISO-PFD-SMA brace system*, Advances in Materials Science and Engineering, Vol. 2017.
9. Kandasamy, R., Cui, F., Townsend, N., Foo, C.C., Guo, J., Shenoi, A., Xiong, Y., (2016), *A review of vibration control methods for marine offshore structures*, *Ocean Engineering*, Vol. 127, p. 279–297.
10. Rustighi, E., Bernnan, M.J., Mace, B.R., (2005), *Real-time control of a shape memory alloy adaptive tuned vibration absorber*, Smart Materials and Structures, Vol. 14, p. 1184-1195.
11. Hilber, H.M., Hughes, T.J.R., Taylor, R.L., (1977), *Improved numerical dissipation for time integration algorithms in structural dynamics*, Earthquake Engineering and Structural Dynamics, Vol. 5, p. 283–292.
12. Ghasemi, M.R., Varaee, H., (2017), *Damping vibration-based IGMM optimization algorithm: fast and significant*, Soft Computing, Vol. 2017, p. 1-31.
13. Mohd Jani, J., Leary, M., Subic, A., Gibson, M.A., (2014), *A Review of Shape Memory Alloy Research*, *applications and opportunities*, Materials and Design, Vol. 56, p. 1078–1113.
14. Qian, H., Li, H., Song, G., Guo, W., (2013), *Recentering shape memory alloy passive damper for structural vibration control*, Mathematical Problems in Engineering, Vol. 2013.
15. Zhang, Y., Zhu, S., (2007), *A shape memory alloy-based reusable hysteretic damper for seismic hazard mitigation*, Smart Materials and Structures, Vol. 16, p. 1603–1613.
16. Wilde, K., Gardoni, P., Fujino, Y., (2000), *Base isolation system with shape memory alloy device for elevated highway bridges*, Engineering Structures, Vol. 22(3), p. 222–229.
17. Auricchio, F., Taylor, R.L., Lubliner, J., (1997), *Shape-memory alloys: macro-modeling and numerical simulations of the superelastic behavior*, Computers Methods in Applied Mechanics and Engineering, Vol. 146(3–4), p. 281-312.
18. Motahari, S.A., Ghassemieh, M., (2007), *Multilinear one-dimensional shape memory material model for use in structural engineering applications*, Engineering Structures, Vol. 29, p. 904–913.
19. Ghodke, S., Jangid, R.S., (2016), *Equivalent linear elastic-viscous model of shape memory alloy for isolated structures*, Advances in Engineering Software, Vol. 99, p. 1–8.
20. Dutta, S.C., Majumder, R., (2019), *Shape Memory Alloy (SMA) as a Potential Damper in Structural Vibration Control*, Springer Nature Switzerland AG 2019, p. 485–492, 2019. (https://doi.org/10.1007/978-3-319-99353-9_51)
21. Paul, S., Datta, T.K., Kapuria, S., (2009), *Control of fixed offshore jacket platform using semi-active hydraulic damper*, Journal of Offshore Mechanics and Arctic Engineering, Vol. 131(4).
22. Nasseri, T., Shabakhty, N., Afshar, M.H., (2014), *Study of fixed jacket offshore platform in the optimization design process under environmental loads*, International Journal of Maritime Technology, Vol. 2, p. 75-84.
23. Asgarian, B., Moradi, S., (2011), *Seismic response of steel braced frames with shape memory alloy braces*, Journal of Constructional Steel Research, Vol. 67, p. 65-74.
24. Nguyen, D.D., Sinsabvarodom, C., (2015), *Nonlinear behavior of a typical oil and gas fixed-jacket offshore platform with different bracing systems subjected to seismic loading*, 20th National Convention on Civil Engineering Conference, Thailand 2015.
25. Zaaijer, M.B., (2006), *Foundation modelling to assess dynamic behavior of offshore wind turbines*, Applied Ocean Research, Vol. 28, p. 45-57.
26. DesRoches, R., McCormick, J., Delemont, M., (2004), *Cyclic properties of superelastic shape memory alloy wires and bars*, Journal of Structural Engineering, Vol. 130(1), p. 38 – 46.
27. Varaee, H., Ghasemi, M.R., (2017), *Engineering optimization based on ideal gas molecular movement algorithm*, *Engineering and Computers*, Vol. 33, p. 71–93.

INTERNATIONAL JOURNAL OF
COASTAL & OFFSHORE ENGINEERING

IJCOE Vol.4/No. 4/ Winter 2019 (37-46)

Available online at: http://ijcoe.org/browse.php?a_code=A-10-201-1&sid=1&slc_lang=en

Comparison between Homotopy Analysis Method (HAM) and Variational Iteration Method (VIM) in Solving the Nonlinear Wave Propagation Equations in Shallow Water

Mohsen Soltani[1], **Rouhollah Amirabadi**[2*]

[1]Ph.D. Student, Department of Civil Engineering, University of Qom; M.Soltani1@stu.qom.ac.ir
[2] Assistant Professor, Department of Civil Engineering, University of Qom; r.amirabadi@qom.ac.ir

ARTICLE INFO

Article History:
Received: 3 Feb. 2019
Accepted: 17 Mar. 2019

Keywords:
Homotopy Analysis Method (HAM)
Variational Iteration Method (VIM)
Shallow water equations

ABSTRACT

This study aims to investigate the capability of two common numerical methods, Homotopy Analysis Method (HAM) and Variational Iteration Method (VIM), and to suggest more efficient approximate solution method to the governing equations of nonlinear surface wave propagation in shallow water. To do so, semi-flat, moderate, and sharp slope of shore which are connected to an open ocean with a uniform depth are exposed to a solitary wave with initial wave height H=2 and stationary elevation d=20. Then, the surface elevation and velocity curves for these profiles are determined and compared by HAM and VIM. To verify the numerical modeling, two slopes i.e. semi-flat and moderate slope are considered and modeled in Flow-3D. Afterwards, the results of surface elevations are compared to each other by using correlation coefficient. The correlation coefficients for the slopes represent that the results coincide well. Ultimately, although the results of both methods are quite similar, using HAM is highly recommend rather than VIM since it makes solution procedure fast-converging and more abridged.

1. Introduction

Tsunamis are sea surface gravity waves generated by large-scale underwater disturbances. There are several stimuli that instigate these long waves: seismic displacement of seabed, volcanic eruptions, landslides, impact of large objects (such as astronomical objects) into the sea surface, and underwater explosions. As a result of these impulsive disturbances, water column—from the bottom to the free surface—is set in motion [1]. During the past era, waves like Tsunamis have imposed lots of irrevocable damages. Therefore, proposing numerical solutions for governing equations of waves has become a common practice in order to forecast waves more accurate [2-3]. For this purpose, several solution methods have been suggested, which Variational Iteration Method (VIM) and Homotopy Analysis Method (HAM) are almost the most common ones among them.

The concept of VIM stems from the studies performed by He in 1990s. According to these studies, VIM is an iterative based approach which does not need the presence of small parameters in the differential equation and is widely used for solution of nonlinear ordinary and partial differential equations. Therefore, this method has frequently been used and known as a reliable tool for solving linear and nonlinear wave equations [4]. In 2006, Yusufglu et al applied VIM in order to regularized long wave equation [5]. In 2007, Hemeda used VIM for the wave equations in different forms i.e. first-order of wave equation in one- and two-dimension and second-order of wave equation in one- and two-dimension. Then, the results showed the effectiveness of this method [6]. In 2011, Mohyud-Din et al used the modified form of VIM to assess propagation of solitary wave by solving seventh order generalized Kdv (SOG-Kdv) equations [7]. In 2012, Younesian et al solved nonlinear wave propagation in shallow water media by VIM [8].

The ideas of HAM in topology was presented by Liao in 1992 in response to nonlinear wave problems. According to this study, it was claimed that the advantages of HAM outweighed other classical methods. The major advantage of this method is being independence of any small or large quantities. Therefore, HAM can be applied to governing equations and boundary/initial conditions containing whether small or large quantities. In addition, apart from providing more accurate and optimized solution without any physical and unrealistic assumptions, the numerical solution of HAM always becomes convergent since this method provides a family of solution expressions in the auxiliary parameter of $\hbar$

which makes the convergence region and rate of each solution convenient[9-16].

There are a lot of attempts made by means of HAM to solve waves equations with different aims. In 2004, Wu et al applied HAM to solve solitary waves governed by Camassa-Holm equation and provided a new analytical approach to solve soliton waves with discontinuity at crest [17]. In 2009, Yusufoglu et al performed HAM to solve Modified Equal Width Wave (MEW) equation and proposed this method as an efficient method for solving MEW equation [18]. In 2013, Shaiq et al recommended HAM as an accurate and reliable algorithm for time-fractional nonlinear wave-like equations which are significantly important in engineering issues [19]. In 2013, Araghi et al used HAM to solve Schrodinger equation with a power law nonlinearity [20]. In 2014, Izadian et al utilized a new approach with a fast and global quadratic rate of convergence for solving nonlinear wave equations by HAM and Newtown method [21]. In 2015, Yin et al used a modified form of HAM for solution of fractional wave equations and proposed this method as a powerful tool to adjust and control the convergence region of infinite series solution by using an auxiliary parameter [22].

According to the previous studies, it is claimed that both HAM and VIM could be used as efficient approaches in solving nonlinear equations. Therefore, this study aims to discuss the procedure of HAM approach and compare this method to VIM in order to investigate which method is more efficient. To do so, three different slopes: semi-flat, moderate, and sharp slope are firstly considered, and governing equations are solved by two algorithms. Secondly, the results of HAM are compared to the results of VIM approach. Then, the examples which are solved by both methods are verified by Flow-3D. Finally, although the responses obtained by HAM and VIM are similar, comparing the time lapse of both methods reveals that HAM reaches to convergent state with a lower computational load and never discretizes.

2. Governing Equations of nonlinear wave propagation

Tsunamis are generally classified as long waves. Solitary waves or combinations of negative and positive solitary-like waves are often used to simulate the run-up and shoreward inundation of these catastrophic waves.

The following equations display the specific case of the run-up of 2D long waves incident upon a uniform sloping beach connected to an open ocean with a uniform depth (Figure 1). The related classical nonlinear shallow-water equations are shown as Eq. (1):

$$\begin{aligned} &\eta_t + (u(h+\eta))_x = 0 \\ &u_t + uu_x + g\eta_x = 0 \end{aligned} \tag{1}$$

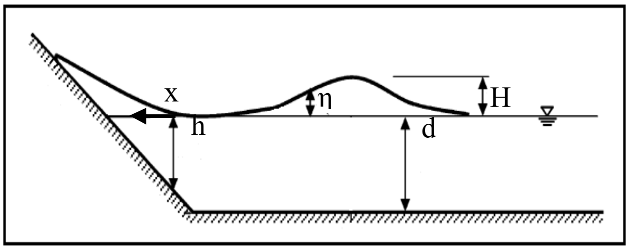

Figure 1. Definition Sketch for solitary wave run-up

where η is wave amplitude, u is depth averaged velocity, h is variable depth, and g . is acceleration of gravity. In addition, the initial condition of these wave is generally represented by Eq. (2):

$$\begin{aligned} &\eta(x,0) = H\,\mathrm{sech}^2\sqrt{\frac{3H}{4d^3}}x \\ &u(x,0) = \frac{\eta}{d}\sqrt{gd} \end{aligned} \tag{2}$$

where H and d denote the initial wave height and stationary elevation, respectively [1,8].

2.1. The basic idea of Homotopy Analysis Method (HAM)

To show the basic idea of HAM, the following procedure is considered. At first, differential equation is considered as Eq. (3):

$$\mathcal{N}[\omega(x,t)] = 0 \tag{3}$$

Where $\mathcal{N}$ is a nonlinear operator, x and t represent the independent variables, and ω is an unknown function. Then, all boundaries or initial conditions are ignored for simplicity, and the deformation equation which is so-called zeroth-order deformation equation is constructed Eq. (4).

$$(1\text{-}q)\mathcal{L}\left[\phi(x,t;q)\text{-}\omega_0(x,t)\right] = q\hbar\mathcal{N}[\phi(x,t;q)] \tag{4}$$

Where $q \epsilon [0,1]$ is the embedding parameter, $\hbar \neq 0$ is an auxiliary parameter, $\mathcal{L}$ is an auxiliary linear operator, $\phi(x,t;q)$ is an unknown function, $\omega_0(x,t)$ is an initial guess of $\omega(x,t)$, and $\phi(x,t;q)$ is an unknown function. It is obvious when q, the embedding parameter, is equal to 0 and 1, Eq. (4) becomes Eqs. (5):

$$\begin{aligned} &\phi(x,t;0) = \omega_0(x,t) \\ &\phi(x,t;1) = \omega(x,t) \end{aligned} \tag{5}$$

respectively. Thus, as$q$ increases from 0 to 1, the solution varies from the initial guess $\omega_0(x,t)$ to the solution $\omega(x,t)$. Expanding $\phi(x,t;q)$ in Taylor series when q is equal to 1 will be Eq. (6):

$$\phi(x,t;q)=\omega_0(x,t)+\sum_{m=1}^{\infty}\omega_m(x,t)q^m \tag{6}$$

Where

$$\omega_m(x,t)=\frac{1}{m!}\frac{\partial^m\phi(x,t;q)}{\partial q^m}\bigg|_{q=0} \tag{7}$$

The convergence of the series in Eq. (6) depends upon the auxiliary parameter $\hbar$. If it is convergent at $q=1$, it will be Eq. (8):

$$\omega(x,t)=\omega_0(x,t)+\sum_{m=1}^{\infty}\omega_m(x,t) \tag{8}$$

Which must be one of the solutions of the original nonlinear equation, as proven by Liao. Then, $\overrightarrow{\omega_n}$ is defined as Eq. (9):

$$\overrightarrow{\omega_n}=(\omega_0(x,t),\omega_1(x,t),\dots,\omega_n(x,t)) \tag{9}$$

Therefore, the following mth-order deformation equation is obtained by differentiating Eq. (3) m-times with respect to q, dividing them by $m!$, and finally setting $q=0$. Then, we have Eq. (10):

$$\mathcal{L}\left[\omega_m(x,t)-\chi_m\omega_{m-1}(x,t)\right]=\hbar R_m(\overrightarrow{\omega_{m-1}}) \tag{10}$$

Where

$$R_m(\overrightarrow{\omega_{m-1}})=\frac{1}{m!}\frac{\partial^{m-1}N[\phi(x,t;q)]}{\partial q^{m-1}}\bigg|_{q=0} \tag{11}$$

And

$$\chi_m=\begin{cases}0, & m\le 1\\ 1, & m>1\end{cases} \tag{12}$$

It should be emphasized that $\omega_m(x,t)$ for $m\ge 1$ is governed by the linear equation of Eq. (10) with linear boundary conditions coming from the original problem, which can be solved by the symbolic computation software such as Mathematica or Maple. To perform HAM, the following initial approximations Eqs. (13) are considered:

$$\begin{aligned}&\eta_0(x,0)=\eta(x,0)=H\,\mathrm{sech}^2\sqrt{\frac{3H}{4d^3}}x\\ &u_0(x,0)=u(x,0)=\frac{\eta}{d}\sqrt{gd}\end{aligned} \tag{13}$$

And the linear operator is defined as Eq. (14):

$$\mathcal{L}_i\left[\phi_i(x,t;q)\right]=\frac{\partial\phi_i(x,t;q)}{\partial t},i=1,2 \tag{14}$$

According to Eq. (1) nonlinear operators $\mathcal{N}_1$ and $\mathcal{N}_2$ can be defined as Eqs. (15):

$$\begin{aligned}&\mathcal{N}_1\left[\phi_1(x,t;q),\phi_2(x,t;q)\right]=\frac{\partial\phi_1(x,t;q)}{\partial t}+\\ &\frac{\partial(\phi_1(x,t;q)\phi_2(x,t;q))}{\partial x}+\frac{\partial(h(x)\phi_2(x,t;q))}{\partial x}\\ &\mathcal{N}_2\left[\phi_1(x,t;q),\phi_2(x,t;q)\right]=\frac{\partial\phi_2(x,t;q)}{\partial t}+\\ &\phi_2\frac{\partial\phi_2(x,t;q)}{\partial x}+g\frac{\partial\phi_1(x,t;q)}{\partial x}\end{aligned} \tag{15}$$

Then, zeroth-order deformation equations are constructed as Eqs. (16):

$$\begin{aligned}&(1-q)\mathcal{L}_1\left[\phi_1(x,t;q)-\eta_0(x,t)\right]=q\hbar_1\mathcal{N}_1\left[\phi_1(x,t;q),\phi_2(x,t;q)\right]\\ &(1-q)\mathcal{L}_2\left[\phi_2(x,t;q)-u_0(x,t)\right]=q\hbar_2\mathcal{N}_2\left[\phi_1(x,t;q),\phi_2(x,t;q)\right]\end{aligned} \tag{16}$$

Obviously, when $q=0$ and $q=1$, we have Eqs. (17):

$$\begin{aligned}&\phi_1(x,t;0)=\eta_0(x,t),\ \phi_1(x,t;1)=\eta(x,t)\\ &\phi_2(x,t;0)=u_0(x,t)\ \phi_2(x,t;1)=u(x,t)\end{aligned} \tag{17}$$

Thus, as the embedding parameter q increases from 0 to 1, $\phi_1(x,t;q)$ and $\phi_2(x,t;q)$ vary from the initial approximations of $\eta_0(x,t)$ and $u_0(x,t)$ to $\eta(x,t)$ and $u(x,t)$ solutions, respectively. By expanding $\phi_1(x,t;q)$ and $\phi_2(x,t;q)$ in Taylor series with respect to q, we have Eqs. (18) and Eqs. (19):

$$\begin{aligned}&\phi_1(x,t;q)=\eta_0(x,t)+\sum_{m=1}^{\infty}\eta_m(x,t)q^m\\ &\phi_2(x,t;q)=u_0(x,t)+\sum_{m=1}^{\infty}u_m(x,t)q^m\end{aligned} \tag{18}$$

Where

$$\begin{aligned}&\eta_m(x,t)=\frac{1}{m!}\frac{\partial^m\phi_1(x,t;q)}{\partial q^m}\bigg|_{q=0}\\ &u_m(x,t)=\frac{1}{m!}\frac{\partial^m\phi_2(x,t;q)}{\partial q^m}\bigg|_{q=0}\end{aligned} \tag{19}$$

If the auxiliary linear operator, the initial approximations, and the auxiliary parameters $\hbar_1$ and $\hbar_2$ are so properly chosen, the above series converge at $q=1$. Then, we have Eqs. (20):

$$\begin{aligned}&\eta(x,t;q)=\eta_0(x,t)+\sum_{m=1}^{\infty}\eta_m(x,t)\\ &u(x,t;q)=u_0(x,t)+\sum_{m=1}^{\infty}u_m(x,t)\end{aligned} \tag{20}$$

Which must be one of solutions of original system. Afterwards, the following vectors Eqs. (21) are defined:

$$\overrightarrow{\eta_n} = (\eta_0(x,t), \eta_1(x,t), \ldots, \eta_n(x,t))$$
$$\overrightarrow{u_n} = (u_0(x,t), u_1(x,t), \ldots, u_n(x,t)) \tag{21}$$

And the mth-order deformation equation, Eq. (22), is obtained:

$$\mathcal{L}_1\left[\eta_m(x,t) - \chi_m \eta_{m-1}(x,t)\right] = \hbar_1 R_{1,m}(\overrightarrow{\eta_{m-1}}, \overrightarrow{u_{m-1}}) \tag{22}$$

Now, the solution of the mth-order deformation equation, Eq. (22), for $m \geq 1$ is Eqs. (23):

$$\eta_m(x,t) = \chi_m \eta_{m-1}(x,t) + \hbar_1 \int_0^t R_{1,m}(\overrightarrow{\eta_{m-1}}, \overrightarrow{u_{m-1}}) ds$$
$$u_m(x,t) = \chi_m u_{m-1}(x,t) + \hbar_2 \int_0^t R_{2,m}(\overrightarrow{\eta_{m-1}}, \overrightarrow{u_{m-1}}) ds \tag{23}$$

According to the initial conditions which are initially assumed, we have Eq. (24):

$$\eta_m(x,0) = 0 \ , \ u_m(x,0) = 0 \tag{24}$$

$\mathcal{R}_{1,m}(\overrightarrow{\eta_{m-1}}, \overrightarrow{u_{m-1}})$ and $\int_0^t \mathcal{R}_{2,m}\left(\overrightarrow{\eta_{m-1}}, \overrightarrow{u_{m-1}}\right)$ are:

$$\mathcal{R}_{1,m}\left(\overrightarrow{\eta_{m-1}}, \overrightarrow{u_{m-1}}\right) = \frac{\partial \eta_{m-1}}{\partial t} + \frac{\partial}{\partial x}\left(\sum_{n=0}^{m-1} \eta_n u_{m-1-n}\right)$$
$$+ h(x) \frac{\partial}{\partial x} u_{m-1} \tag{25}$$
$$\mathcal{R}_{2,m}\left(\overrightarrow{\eta_{m-1}}, \overrightarrow{u_{m-1}}\right) = \frac{\partial u_{m-1}}{\partial t} + \left(\sum_{n=0}^{m-1} u_n \frac{\partial u_{m-1-n}}{\partial x}\right) + g \frac{\partial}{\partial x} \eta_{m-1}.$$

Obviously, the solution of the mth-order deformation equations, Eq. (22), for $m \geq 1$ becomes:

$$\eta_m = \chi_m \eta_{m-1} + \hbar_1 \mathcal{L}^{-1}[\mathcal{R}_{1,m}\left(\overrightarrow{\eta_{m-1}}, \overrightarrow{u_{m-1}}\right)]$$
$$u_m = \chi_m u_{m-1} + h_2 L^{-1}\left[R_{2,m}\left(\overrightarrow{\eta_{m-1}}, \overrightarrow{u_{m-1}}\right)\right] \tag{26}$$

To make the solution method more simple, *h1* and *h2* are assumed equal to h.

2.2. The basic idea of Variational Iteration Method (VIM)

To show the procedure of VIM, the correction functional is constructed at first as Eq. (27) and Eq. (28) [8]:

$$u_{n+1}(t) = u_n(t) - \int_0^t \left(\dot{u}_n + E_n(\tau)\right) d\tau \tag{27}$$

$$\eta_{n+1}(t) = \eta_n(t) - \int_0^t \left(\dot{\eta}_n + F_n(\tau)\right) d\tau \tag{28}$$

Where E_n and F_n are :

$$E_n = u_n u_n' + g\eta_n' \tag{29}$$

$$F_n = (u_n(\eta_n + H))' \tag{30}$$

The corresponding first-order iterations are obtained by Eq. (31) and Eq. (32):

$$u_1 = u_0(t) - \int_0^t \left(\dot{u}_n + u_0 u_0' + g\eta_0'\right) d\tau =$$
$$u_0 - \left(u_0 u_0' + g\eta_0'\right)t \tag{31}$$

$$\eta_1 = \eta_0(t) - \int_0^t \left(\dot{\eta}_0 + (u_0(\eta_0 + H))'\right) d\tau =$$
$$\eta_0 - (u_0(\eta_0 + H))' t \tag{32}$$

The second-order approximations are:

$$u_2 = u_0 - \left(u_0 u_0' + g\eta_0'\right) - \int_0^t \left(\dot{u}_1 + u_1 u_1' + g\eta_1'\right) d\tau =$$
$$u_0 + t[-\left(u_0 u_0' + g\eta_0'\right] + \frac{t^2}{2}[u_0\left(u_0 u' + g\eta_0'\right) + u_0' \times$$
$$\left(u_0 u_0' + g\eta_0'\right) + g(u_0\left(\eta_0 + H\right))''\right] + \frac{t^3}{3} \times$$
$$\left[-\left(u_0 u_0' + g\eta_0'\right)\left(u_0 u_0' + g\eta'\right)'\right] \tag{33}$$

$$\eta_2 = \eta_0 - (u_0(\eta_0 + H))' t - \int_0^t \left(\dot{\eta}_0 + (u_0(\eta_0 + H))'\right) d\tau -$$
$$\int_0^t \left(\dot{\eta}_1 + (u_1(\eta_1 + H))'\right) d\tau = \eta_0 + t[-u_0'\left(\eta + H\right) -$$
$$u_0\left(\eta' + H'\right)] + \frac{t^2}{2}[u_0'(u_0\eta_0 + H))' + \left(\eta_0 + H\right)\left(u_0 u_0' + g\eta_0'\right)'$$
$$+ u_0\left(u_0\left(\eta_0 + H\right)\right)'' + \left(\eta_0' + H'\right)\left(u_0 u_0' + g\eta_0'\right)']$$
$$+ \frac{t^3}{3}\left[-\left(u_0 u_0' + g\eta_0'\right)(u_0\left(\eta_0' + H'\right))' - (u_0 u_0' + g\eta_0')(u_0\eta_0 + H))''\right)] \tag{34}$$

Then surface elevation and velocity profiles are obtained after substituting the general initial conditions (Eq. (2)) into Eq. (35) and Eq. (36).

$$u_2 = B\,\text{sech}^2 \alpha x + 2t \times (B^2 \alpha\,\text{sech}^5(\alpha x)\sinh^2(\alpha x)$$
$$- gA\alpha \sinh\alpha\,\text{sech}^3(\alpha) \times \frac{t^2}{2} - 2B^3\alpha^2\,\text{sech}^8(\alpha x)\cosh^2(\alpha x)$$
$$+ 22gAB\alpha^2 \sec\alpha x)\sin(\alpha x) - 6gAB\alpha^2\,\text{sech}^6(\alpha x)$$
$$\cosh^2(\alpha x) - 2gB\alpha^2 H \cosh^2(\alpha x)\,\text{sech}^4(\alpha x) + 6gB\alpha^2 H$$
$$\text{sech}^4(\alpha x) \times \sinh^2(\alpha x) \times BgH''\,\text{sech}^2(\alpha x) + 8g\alpha^2$$
$$AB\sinh^2(\alpha x) + \text{sech}^6(\alpha x) - 4\alpha BH' \sinh(\alpha x)\,\text{sech}^3(\alpha x)$$
$$+ \frac{t^3}{3}[-8\alpha^3 B^4 \sinh^3(\alpha x)\,\text{sech}^{11}(\alpha x) - 8g\alpha^3 AB^2 \sinh^2(\alpha x)$$
$$\text{sech}^9(\alpha x) + 4B^4\alpha^4\,\text{sech}^9(\alpha x)\sinh(\alpha x) - 12B^4\alpha^4$$
$$\text{sech}^{11}(\alpha x)\sinh^2(\alpha x) + 8g\alpha^3 AB^2\,\text{sech}^7(\alpha x)\sinh(\alpha x) -$$
$$24g\alpha^3 AB\,\text{sech}^9(\alpha x)\sinh^2(\alpha x) + 4Ag^2\alpha^3$$
$$\text{sech}^7 \alpha x \sinh(\alpha x) - 12g^2\alpha^3 A^2\,\text{sech}^5(\alpha x)\sinh(\alpha x)] \tag{35}$$

And

$$\eta_2 = A\,\mathrm{sech}^2(\alpha x) + t\times[-4\alpha AB\sinh(\alpha x)\mathrm{sech}^5(\alpha x)$$
$$-2\alpha ABH'\sinh(\alpha x)\mathrm{sech}^3(\alpha x) + BH'\mathrm{sech}^2(\alpha x) + t^2\times$$
$$[\left(-8\alpha^2AB^2 - 16\alpha^2AB^2\alpha^2 - 12AB^2\alpha^2 - 6\alpha^2AB^2\right)$$
$$\mathrm{sech}^8(\alpha x) + \left(36\alpha^2AB^2 - 20\alpha^2B^2g - 10\alpha^2A^2g\right)$$
$$\mathrm{sech}^6(\alpha x) + \left(16\alpha^2B^2 - 6Ag\alpha\right)H\,\mathrm{sech}^4(\alpha x) +$$
$$\left(-20\alpha^2B^2H'\right)\mathrm{sech}^6(\alpha x) - 8\alpha B^2H'\mathrm{sech}^5(\alpha x)\sinh(\alpha x)$$
$$-2A\alpha gH'\mathrm{sech}^3(\alpha x)\sinh(\alpha x) + 4\mathrm{HA}\alpha^2\mathrm{gsech}^2(\alpha\mathrm{x})] \tag{36}$$

3. Numerical experiments

Now that the procedures of HAM and VIM have been discussed, three different examples with different profile shores (i.e. semi-flat, moderate, and sharp slopes) are modeled as follow by aforementioned approaches. Then, the following examples are exposed to a solitary wave with initial wave height $H = 2$ and stationary elevation $d = 20$ [8]. Then, the results which are determined by HAM are compared to those obtained by VIM [23].

3.1. Semi-Flat Shores

For modeling a semi-flat shore, the below shore profile is firstly considered Eq. (37):

$$h(x) = 0.2x - 20 \tag{37}$$

Then, the elevation profile Eq. (40) and surface elevation Eq. (41) are obtained by the following analytical expressions for HAM after initial amounts of $\eta_0(x,t)$ and $u_0(x,t)$ are determined by Eq. (38) and Eq. (39):

$$\eta_0(x,t) = 2\ \mathrm{sech}[0.0137x]^2 \tag{38}$$

$$u_0(x,t) = 1.4007\ \mathrm{sech}[0.0137x]^2 \tag{39}$$

$$\eta_1(x,t) = -0.1534t\ (-1.8257\hbar sech^2[0.0137x] -$$
$$5\hbar sech^2[0.0136x]tanh[0.0137x] + 0.05x\ \hbar$$
$$sech^2[0.0137x]tanh[0.0137x] + \hbar sech^4[0.0137x]$$
$$tanh[0.0137x]) \tag{40}$$

$$u_1(x,t) = -0.0537t\ (10\hbar\ \mathrm{sech}^2[0.0137x]$$
$$\tanh[0.0137x] + \hbar\ \mathrm{sech}^4[0.0137x]\ \tanh[0.0137x]) \tag{41}$$

The rest of the components of the iteration formulas by HAM can easily be obtained by symbolic computation software. Subsequently, the following approximate solutions in term of a series up to 4th-order for $\eta = \sum_{i=0}^{4}\eta_i$ and $u = \sum_{i=0}^{4}u_i$ are obtained. The series solutions contain the auxiliary parameter $\hbar$. The validity of the method is based on assumption that the series of Eq. (6) converges at $q = 1$. In a essence, It is the auxiliary parameter $\hbar$ which ensures that this assumption can be satisfied. As it was pointed out by Liao, in general, by means of the so-called $\hbar$-curve in Figures 2 and 3, it is straightforward to choose a proper value of $\hbar$ which results in convergence of the series. In addition, Liao mentioned that the valid region of $\hbar$ is a horizontal line segment [13]. So, $\hbar = -1$ is chosen in following computational works.

After the series become converged in HAM, the equations are solved on the bases of VIM approach as follows, and the results are shown in figures 4-7.

The solutions of VIM for $u_2(x,t)$ and $\eta_2(x,t)$ can be obtained by the following analytical expressions Eq. (42) and Eq. (43):

$$u_2 = 1.400714sech^2(0.013693x) + 2t\times$$
$$(0.2686566\sinh(0.013693x)\mathrm{sech}^3(0.013693x)$$
$$+0.02686566\sinh(0.013693x)\cosh^5(0.013693))$$
$$\times t^2(-0.00367014sech^8(0.013693x) - 0.07407 \tag{42}$$

$$\eta_2 = 2sech^2(0.013693x) + t[0.15336\times$$
$$\sinh(0.013693x)sinh^5(0.013693x) - 0.280143 +$$
$$sech^2(0.013693x)0.007672xsinh(0.013693x)$$
$$sinh^3(0.013693x) - 0.7672\sinh(0.013693)$$
$$-0.05373sech^3(0.013693x)\sinh(0.013693x)$$
$$-0.021492sech^5(0.013693x)\sinh(0.013693x)$$
$$-0.00007375xsech^6(0.013693x) - 0.0016186x$$
$$sech^4(0.013693x)] \tag{43}$$

In Figures 4 and 5, graphical solutions of $\eta(x,t)$ and $u(x,t)$ are represented. The elevation and velocity profiles are illustrated versus time and position in Figures 6 and 7. By comparing these figures, it is concluded that HAM and VIM solutions are exactly similar.

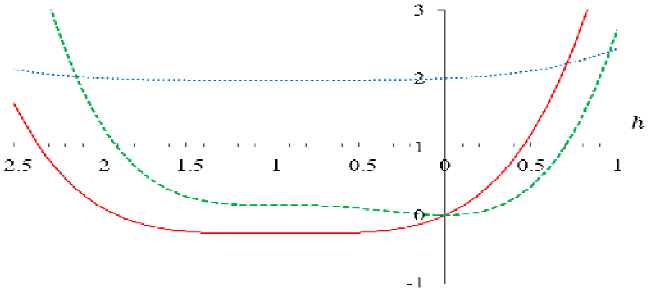

Figure 2. The $\hbar$ -curves according to 4th-order approximation. Dashed point: $\eta(0.1,0.1)$, solid line: $\dot{\eta}(0.1,0.1)$, and dashed line: $\ddot{\eta}(0.1,0.1)$.

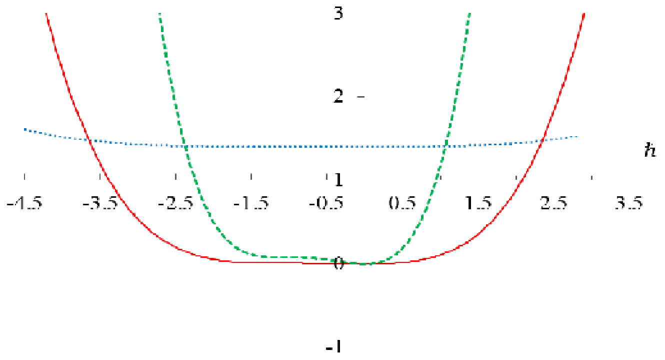

Figure 3. The $\hbar$ -curves according to 4th-order approximation. Dashed point: $u(0.1,0.1)$, solid line: $\dot{u}(0.1,0.1)$, and dashed line: $\ddot{u}(0.1,0.1)$.

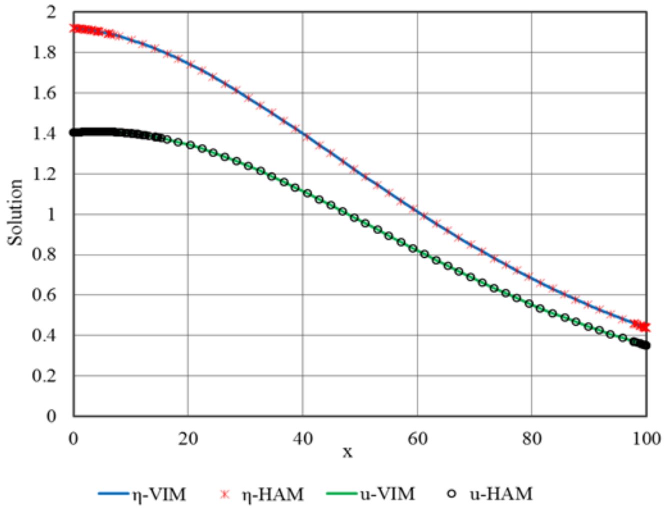

Figure 4. HAM and VIM solutions of $\eta(x,t)$ and $u(x,t)$ for semi-flat shore, $t=0.3$ and $0\leq x\leq100$

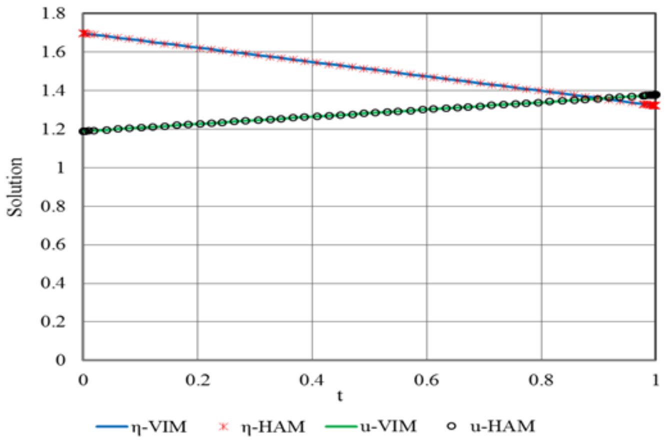

Figure 5. HAM and VIM solutions of $\eta(x,t)$ and $u(x,t)$ for semi-flat shore, $x=30$ and $0\leq t\leq1$.

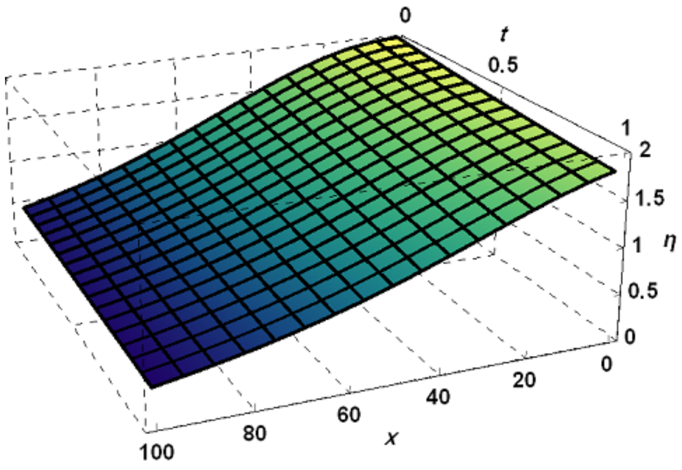

Figure 6. HAM solution of $\eta(x,t)$ for semi-flat shore

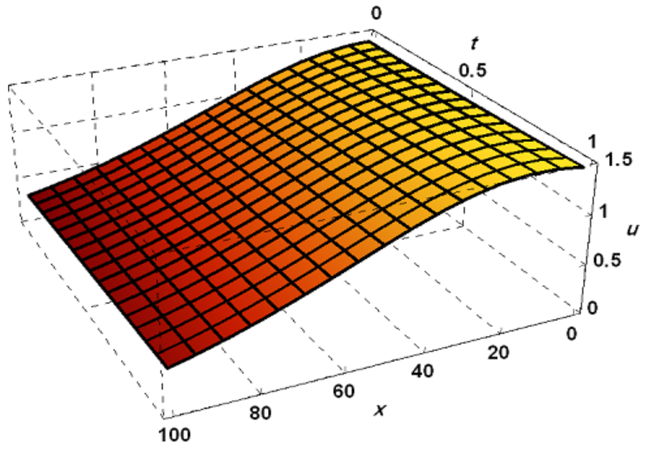

Figure 7. HAM solution of $u(x,t)$ for semi-flat shore

3.2. Moderate-Slope Shores

for modeling a moderate-slope shore, the below shore Eq. (44) profile is firstly considered:

$$h(x)=x-100 \tag{44}$$

Then, the elevation profile Eq. (47) and surface elevation Eq. (48) are obtained by the following analytical expressions for HAM after initial amounts of $\eta_0(x,t)$ and $u_0(x,t)$ are determined (Eq. (45) and Eq. (46)):

$$\eta_0(x,t)=2sech[0.0137x]^2 \tag{45}$$

$$u_0(x,t)=1.4007\ \text{sech}[0.0137x]^2 \tag{46}$$

$$\begin{aligned}\eta_1(x,t)=&-0.1534\ t\times(-9.12871\ \hbar\ \text{sech}^2[0.0137x]\\&-25\ \hbar\ \text{sech}^2[0.0137x]\ \tanh[0.0137x]\\&+0.25\ x\ \hbar\ \text{sech}^2[0.0137x]\ \tanh[0.0137x]\\&+\hbar\ \text{sech}^4[0.0137x]\ \tanh[0.0137x])\end{aligned} \tag{47}$$

$$\begin{aligned}u_1(x,t)=&-0.0537t\ (10\hbar sech^2[0.0137x]\\&tanh[0.0137x]+\hbar sech^4[0.0137x]\\&tanh[0.0137x])\end{aligned} \tag{48}$$

The auxiliary parameter of $\hbar$ is considered equal to -1, and the series will be expanded up to 4th-order. After the series become converged in HAM, the equations are solved on the bases of VIM approach by the following analytical expressions Eq. (49) and Eq. (50):

$$\begin{aligned}
&u_2 = 1.400714 sech^2(0.013693x) + 2t \\
&(0.2686566\sinh(0.013693x) sech^3(0.013693x) \\
&+0.02686566\sinh(0.013693x) cosh^5(0.013693x)) \\
&\times t^2(-0.00367014 sech^8(0.013693x) \\
&sech^4(0.013693x) - 0.515287 sech^2(0.013693) \\
&-0.3766313 sech^3(0.013693x)\sinh(0.013693x) \\
&+0.00515288x sech^2(0.013693x) - 0.007729x \times \\
&sech^4(0.013693x)
\end{aligned} \tag{49}$$

$$\begin{aligned}
&\eta_2 = 2 sech^2(0.013693x) + t(0.15336 \\
&\sinh(0.013693x) sech^5(0.013693x) \\
&-1.4007 sech^2(0.013693x) - 3.836 \\
&\sinh(0.013693x) sech^3(0.013693x) + \\
&0.34433 sech^6(0.013693x) + 0.83875 \\
&sech^4(0.013693x) - 0.735 sech^2(0.013693x) \\
&+0.00735x sech^2(0.013693x) - 0.26865 \\
&sech^3(0.013693x)\sinh(0.013693x) \\
&-0.00367875x sech^6(0.013693x) - 0.008093x \\
&sech^4(0.013693x)
\end{aligned} \tag{50}$$

Then, the results are shown in figures 8-11. In Figures 8 and 9, the graphical solutions of $\eta(x,t)$ and $u(x,t)$ are represented. And also, the elevation and velocity profiles are illustrated versus time and position in Figures 10 and 11. By comparing these figures, it is concluded that HAM and VIM solutions are exactly similar.

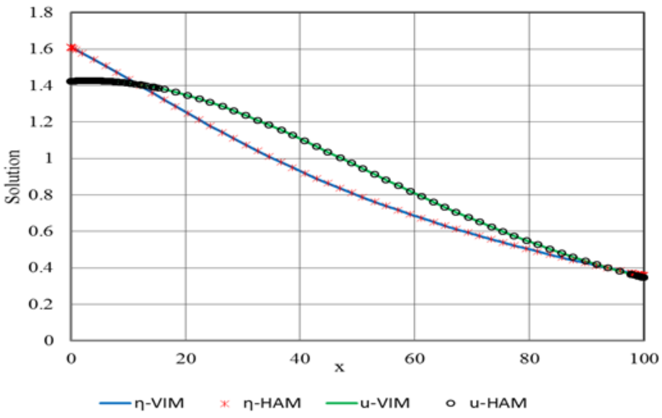

Figure 8. HAM and VIM solutions of $\eta(x,t)$ and $u(x,t)$ for moderate-slope shore at $t = 0.3$ in $0 \le x \le 100$.

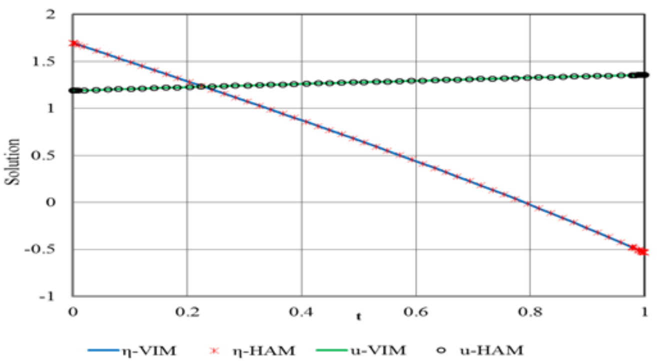

Figure 9. HAM and VIM solutions of $\eta(x,t)$ and $u(x,t)$ for moderate-slope shore at in $0 \le t \le 1$.

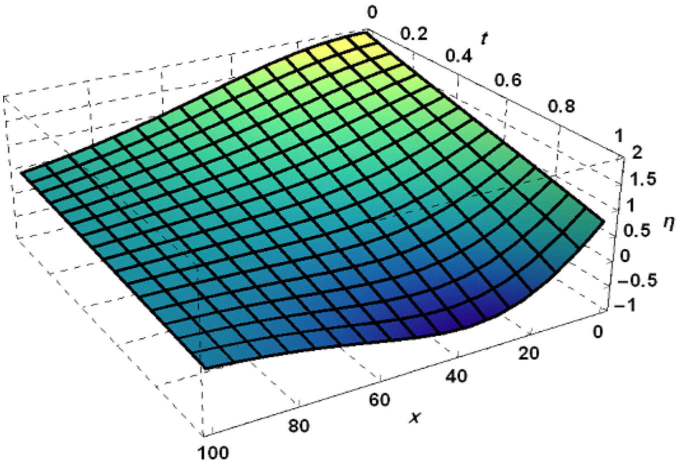

Figure 10. HAM solution of $\eta(x,t)$ for moderate-slope shore

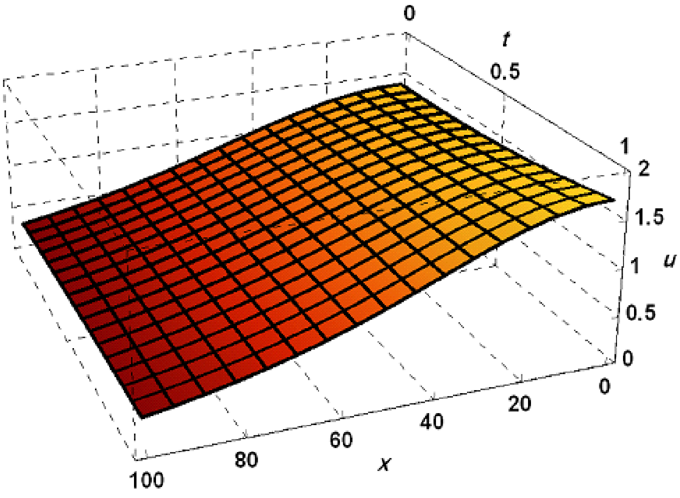

Figure 11. HAM solution of $u(x,t)$ for moderate-slope shore

3.3. Sharp-Slope Shores

For modeling a sharp-slope shore, the below shore profile is firstly considered:

$$h(x) = 5x - 500 \tag{51}$$

Then, the elevation profile Eq. (54) and surface elevation Eq. (55) are obtained by the following analytical expression for HAM after initial aunts of $\eta_0(x,t)$ and $u_0(x,t)$ are determined by Eq. and Eq. (53):

$$\eta_0(x,t)=2\,\mathrm{sech}[0.0137x]^2 \tag{52}$$

$$u_0(x,t)=1.40071\,sech\left[0.0137x\right]^2 \tag{53}$$

$$\begin{aligned}\eta_1(x,t)= -0.1534\, t\, (&-45.6435\,\hbar\,\mathrm{sech}^2[0.0137x]\\ &-125\,\hbar\,\mathrm{sech}^2[0.0137x]\tanh[0.0137x]+1.25\, x\,\hbar\\ &\mathrm{sech}^2\left[0.0137x\right]\tanh[0.0137x]+\\ &\hbar\,\mathrm{sech}^4\left[0.0137x\right]\tanh[0.0137x])\end{aligned} \tag{54}$$

$$\begin{aligned}u_1(x,t)=-0.0537\, t\, (&10\,\hbar\,\mathrm{sech}^2[0.0137x]\\ &\tanh[0.0137x]+\hbar\,\mathrm{sech}^4[0.0137x]\tanh[0.0137x])\end{aligned} \tag{55}$$

The auxiliary parameter of $\hbar$ is considered equal to -1, and the series will be expanded up to 10th-order. After the series become converged in HAM, the equations are solved on the bases of VIM approach by the following analytical expressions Eq. (56) and Eq. (57):

$$\begin{aligned}u_2=&1.400714\mathrm{sech}^2\left(0.013693x\right)+2t\\ &\left(0.2686566\sinh\left(0.013693x\right)\mathrm{sech}^3\left(0.013693x\right)\right.\\ &\left.\right)\times t^2(-0.00367014\mathrm{sech}^8\left(0.013693x\right)-0.07407\\ &\mathrm{sech}^6\left(0.013693x\right)+3.9265\mathrm{sech}^4\left(0.013693x\right)\\ &-2.57643\mathrm{sech}^2\left(0.013693x\right)-1.883156\\ &\mathrm{sech}^3\left(0.013696x\right)\sinh\left(0.013693x\right)+\\ &0.0257644x\mathrm{sech}^2\left(0.01363x\right)-0.0386465x\\ &\mathrm{sech}^4(0.013693x)\end{aligned} \tag{56}$$

$$\begin{aligned}\eta_2=&2\mathrm{sech}^2\left(0.013693x\right)+t(0.15336\\ &\sinh\left(0.013693x\right)\mathrm{sech}^5\left(0.013693x\right)\\ &-7.00357\mathrm{sech}^2\left(0.013693x\right)+0.1918x\\ &\sinh\left(0.013693x\right)\mathrm{sech}^3\left(0.013693x\right)\\ &\quad-0.1918\sinh\left(0.013693x\right)\mathrm{sech}^3\left(0.013693x\right)+\\ &t^2[-0.0101545\mathrm{sech}^8\left(0.013693x\right)+1.81583\\ &\mathrm{sech}^6\left(0.013693x\right)-4.076\mathrm{sech}^4\left(0.013693x\right)\\ &-1.861\mathrm{sech}^2\left(0.013693x\right)+0.03675x\\ &\mathrm{sech}^2\left(0.013693x\right)-1.34325\mathrm{sech}^3\left(0.013693x\right)\\ &\sinh(0.013693x)-0.5373x\mathrm{sech}^5\left(0.013693x\right)\\ &\sinh(0.013693x)-0.018393x\mathrm{sech}^6\left(0.013693x\right)\\ &-0.040465x\mathrm{sech}^4(0.013693x)\end{aligned} \tag{57}$$

Then, the results are shown in figures 10-13. In figures 10, the graphical solutions of $\eta(x,t)$ and $u(x,t)$ are represented. And also, the elevation and velocity profiles are illustrated versus time and position in figures 12 and 13. By comparing these figures, it is concluded that HAM and VIM solutions are similar.

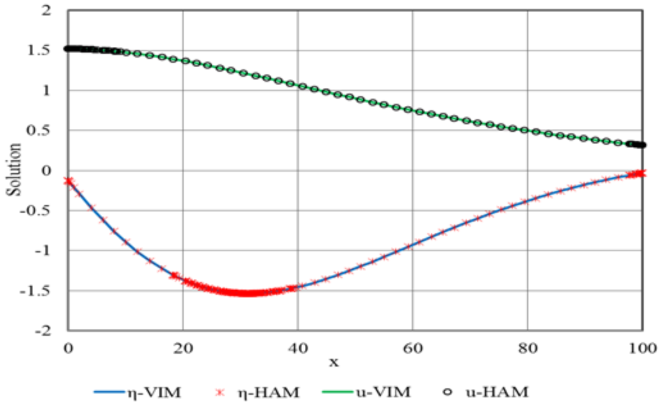

Figure 10. HAM and VIM solutions of $\eta(x,t)$ and $u(x,t)$ for sharp-slope shore at $t=0.3$ in $0\le x\le 100$

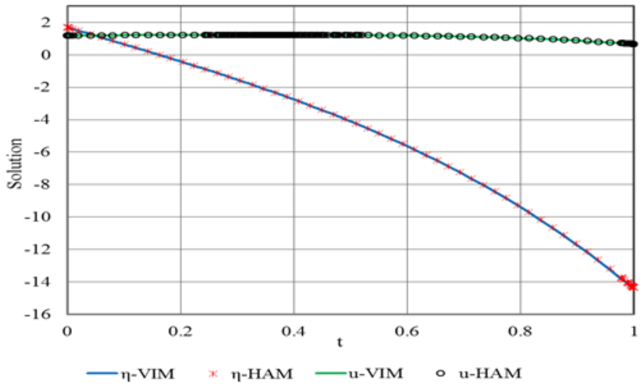

Figure 11. HAM and VIM solutions of $\eta(x,t)$ and $u(x,t)$ for sharp-slope shore at in $0\le t\le 1$.

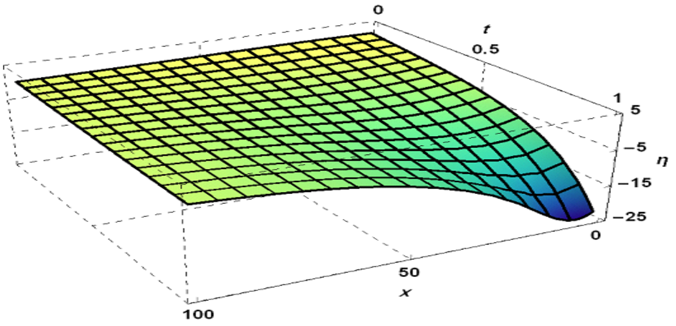

Figure 12. HAM solution of $\eta(x,t)$ for sharp-slope shore

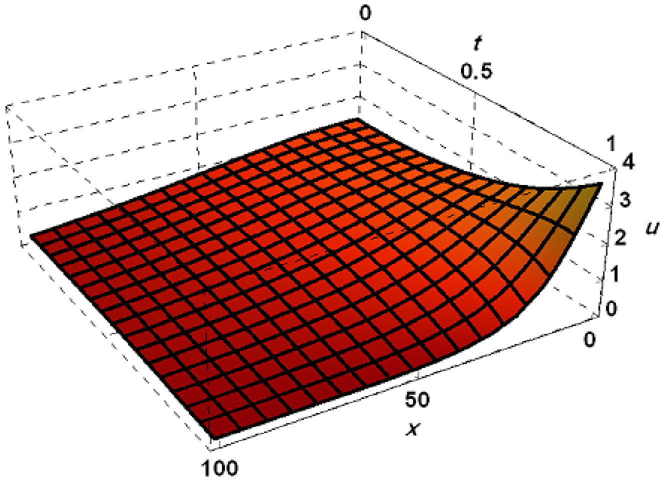

Figure 13. HAM solution of $u\left(x,t\right)$ for sharp-slope shore

4. Model verification

To verify the numerical models, two aforementioned slopes (semi-flat and moderate-slope shore), as examples, are selected and modeled in Flow-3D, and $\eta(x,t)$s are shown in figures 16-17 at t=0.3s for them. To compare the software and numerical results to the numerical results, correlation coefficients for each slope are obtained by Eq. (58) and shown in figures 17-19.

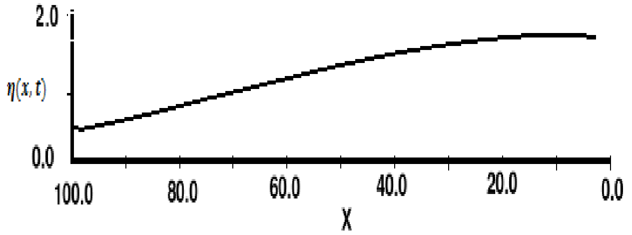

Figure 16. Flow-3D solutions of $\eta(x,t)$ for semi-flat shore at $t=0.3$ in $0\leq x\leq 100$

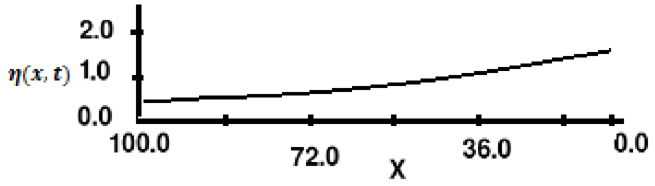

Figure 17. Flow-3D solutions of $\eta(x,t)$ for moderate-slope shore at $t=0.3$ and $0\leq x\leq 100$

$$CC=\frac{\Sigma(x_i-\bar{x})(y_i-\bar{y})}{\sqrt{(x_i-\bar{x})^2(y_i-\bar{y})^2}} \tag{58}$$

Where x denotes the measured values from the numerical model and y is the measured values from flow 3D model. The value of cc=1 shows that two variables are exactly the same.

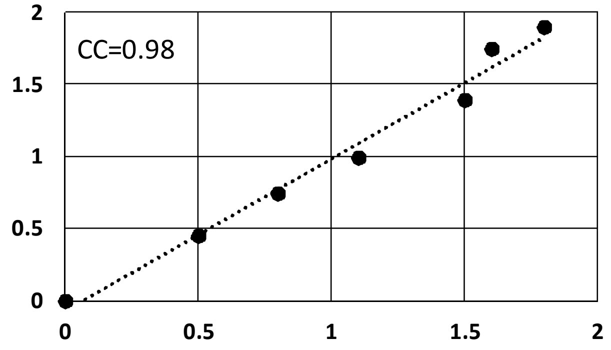

Figure 18. coefficient correlation of $\eta(x,t)$ between Flow-3D and numerical model results for semi-flat shore at $t=0.3$ in $0\leq x\leq 100$.

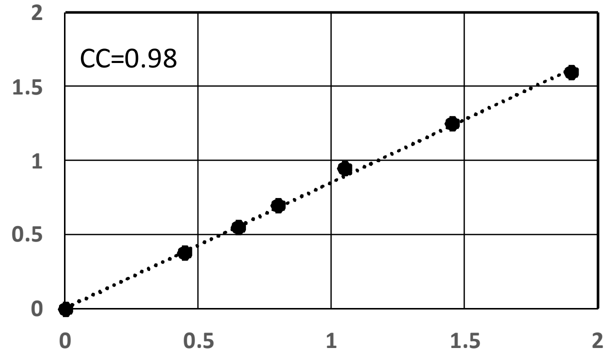

Figure 19. coefficient correlation of $\eta(x,t)$ between Flow-3D and numerical model results for moderate slope shoreat $t=0.3$ in $0\leq x\leq 100$.

Conclusions

In this paper, the Homotopy Analysis Method (HAM) is applied to show the efficiency of this solution method in solving nonlinear surface wave propagation equations in shallow water. For this purpose, three shore profiles including semi-flat, moderate-slope, and sharp-slope shores are modeled by HAM and compared to the results obtained by Variational Iteration Method (VIM). The comparison represents that the results of both methods well coincide. However, it is remarkable to mention that HAM approach never discretizes, and using HAM rather than VIM provides a convenient solving method to control the convergence of approximation series, which is shown and observed during the solution process. Furthermore, as it is represented in the procedure of HAM, this method is more abridged and is not affected by computation round off errors. Ultimately, since the advantage of HAM outweighs VIM, HAM is highly recommended for solving the governing equation in shallow water in order to hind cast surface elevation and velocity of tsunami events at desired time and location.

6. References

1- N. Gedik, E. Irtem, S. Kabdasli, (2001), *Laboratory investigation on tsunami run-up*, Ocean Engineering vol. 32, p. 513-528.

2-Dezvareh, R., Bargi, K., & Moradi, Y, (2012), *Assessment of Wave Diffraction behind the Breakwater Using Mild Slope and Boussinesq Theories,* International Journal of Computer Applications in Engineering Sciences, 2(2).

3-Keskin, Y., & Oturanc, G, (2010), *Reduced differential transform method for solving linear and nonlinear wave equations*, Iranian Journal of Science and Technology (Sciences), 34(2), 113-122.

4-O. Kiymaz, A. Cetinkaya, 2010, *Variational Iteration method for class of Nonlinear Differential Equations,* international journal of contemporary mathematics sciences Vol.5, p.1819-1826.

5-E. Yusufoglu, A. Bekir, 2006, *Application of the variational iteration method to the regularized long wave equation,* an international journal computers & mathematics with applications, p. 1154-1161.

6- A. Hemeda, 2007, *Variatinal iteration method for solving wave equation*, an international journal computers and mathematics with applications, p. 1948-1953.

7- S. Mohyud-Din, M. Noor, F. Jabeen, 2011, *modified variational iteration method for traveling wave solutions of seventh-order generalized KdV equations*, p. 107-113.

8- Younesian, M., Askari, H., Saadatnia, Z. and Yildirim, A., (2012), *Analytical solution for nonlinear wave propagation in shallow media using the variational iteration method,* Waves in Random and Complex Media, vol. 22, no. 2, p. 133-142.

9- S.-J. Liao, (1992*), The proposed homotopy analysis technique for the solutions of nonlinear problems, Ph.D. thesis*, Shanghai Jiao Tong University, Shanghai, China.

10- S.-J. Liao, (1995), *An approximate solution technique not depending on small parameters: a special example*, International Journal of Non-Linear Mechanics, vol. 30, no. 3, p. 371–380.

11- S.-J. Liao, (1997), *A kind of approximate solution technique which does not depend upon small parameters—II: an application in fluid mechanics*, International Journal of Non-Linear Mechanics, vol. 32, no. 5, p. 815–822.

12- S.-J. Liao, (1999), *An explicit, totally analytic approximate solution for Blasius' viscous flow problems*, International Journal of Non-Linear Mechanics, vol. 34, no. 4, p. 759–778.

13- S.-J. Liao, K. F. CHEUNG, (2003), *Homotopy analysis of nonlinear progressive waves in deep water,* Journal of Engineering Mathematics, vol. 45, no. 2, p. 105-116.

14- S.-J. Liao, (2004), *Beyond Perturbation: Introduction to the Homotopy Analysis Method*, vol. 2 of CRC Series:Modern Mechanics and Mathematics, Chapman & Hall/CRC, Boca Raton, Fla, USA.

15- S.-J. Liao, (2004), *On the homotopy analysis method for nonlinear problems*, Applied Mathematics and Computation, vol. 147, no. 2, p. 499–513.

16- Rashidi M.M., Ganji D.D., Dinarvand S., (2008), *Approximate traveling wave solutions of coupled Whitham-Broer-Kaup shallow water equations by homotopy analysis method*, Differential Eq Nonlinear Mechanics, p. 1-8.

17- W. Wu, S. Liao, 2005, *Solving solitary waves with discontinuity by means of the Homotopy Analysis Method,* chaos solitons & fractals, p.177-185.

18-E. Yusufoglu, C. Selam, 2009, *the homotopy analysis method to solve the modified equal width wave equation,* numerical methods for partial differential equations.

19- M. Shaiq, Z. Iqbal, S. Mohyud-Din, 2013, *Homotopy Analysis Method for time-fractional wave-like equations*, computational mathematics and modeling, Vol.24, NO. 4.

20-Araghi, F., & Naghshband, S, (2013), *On convergence of Homotopy Analysis Method to solve the Schrodinger equation with a power law nonlinearity*, International Journal of Industrial Mathematics, 5(4), 367-374.

21-Izadian, J., Abrishami, R., & Jalili, M, (2014), *A new approach for solving nonlinear system of equations using Newton method and HAM*, Iranian Journal of Numerical Analysis and Optimization, 4(2), 57-72.

22- X. Yin, S. Kumar, D. Kumar, 2015, *A modified Homotopy Analysis Method for solution of fractional wave equations*, Advances in mechanical engineering, Vol. 7, p. 1-8.

23- S. Waewcharoen, S. Boonyapibanwong, and S. Koonprasert, (2008), *Application of 2D-Nonlinear Shallow Water Model of Tsunami by using Adomian Decomposition Method*, AIP Conf. Proc. 1048, p. 580–584.

INTERNATIONAL JOURNAL OF
COASTAL & OFFSHORE ENGINEERING

IJCOE Vol.4/No. 4/ Winter 2019 (47-57)

Available online at: http://ijcoe.org/browse.php?a_code=A-10-119-1&sid=1&slc_lang=en

Application of Soft Computing in the Design and Optimization of Tuned Liquid Column–Gas Damper for Use in Offshore Wind Turbines

Reza Dezvareh[1*]

[1*] *Assistant Professor, Faculty of Civil Engineering, Babol Noshirvani University of Technology, Iran; rdezvareh@nit.ac.ir*

ARTICLE INFO

Article History:
Received: 15 Feb. 2019
Accepted: 18 Mar. 2019

Keywords:
offshore wind turbine
tuned liquid column gas damper
soft computing
neural network
Simulink model

ABSTRACT

Tuned liquid column gas damper is a new type of energy absorber that can mitigate the vibrations of structures if their frequency and mass parameters are well tuned. Since this damper has recently been introduced and its behaviour in certain structures such as offshore oil platforms and wind turbines has already been tested, a suitable and accurate method is required to identify these optimal parameters. Therefore, considering the complexity of loads exerted on wind turbines in seas (wave and wind loads), in present study attempts are made to use a new artificial neural network approach to obtain optimal tuned liquid column–gas damper (TLCGD) parameters for mitigation of wind turbine vibrations. First fixed offshore wind turbines at various depths are designed in the MATLAB coding environment. After obtaining the stiffness, damping and mass matrices of the structures, the program enters the Simulink, and the wind turbine structure along with the TLCGD is exposed to different wave-wind load combinations within reasonable range of damper parameters. The neural network training is launched based on available statistical data of the offshore wind turbine with different heights as well as different frequency and mass ratios of the damper. According to this method, the percentage of errors found in the neural network outputs was negligible compared to the actual results obtained from the analysis in Simulink (even for inputs that stood outside the training range of the neural network). The mean error percentage, the standard deviation and the effective value of the neural network with actual values are below 10% for all three types of the structure. Finally, the method presented in this study can be used to obtain optimal parameters of the TLCGD for all kinds of offshore wind turbines at different depths of the sea, which leads to the optimal design of this damper to reduce the vibrations of wind turbines under wave and wind load pressures.

1. Introduction

Wind energy provides an environmentally friendly option .It can also provide sustainable development security when fossil fuels are reduced [1]. Nowadays, offshore wind turbine is one of the sources of wind energy in the world. Offshore wind turbines (OWTs) are one of the structures continuously under dynamic loads during their lifetime. It is also important to locate these turbines in the wind farm and calculate the optimum locations [2]. By installing the wind turbines in the sea, new issues arise when installing these structures on land, which are due to additional loads of the sea environment and special features of the design of this structure [3]. The vibration control devices have been invented and used to reduce the vibrations caused by wind, earthquake, and any other dynamic load in a variety of structures. The tuned dampers, including TMD, TLCD, and TLCGD are one of the vibration reduction tools that are used passively. These dampers are of inactive (passive) type and their parameters are designed once according to the structure's characteristics, which remain constant throughout the exploitation time [4]. Moreover, recently semi-active damper (SALCGD) also assessed [5]. In other words, in addition to being permanently induced by vibrations and stimulations due to the wind loads, the loads resulting from the sea environment such as the wave load, sea flows, etc. are applied to the wind turbines. This led Lackner and Rotea (2011) [6] to study the inactive control of the vibrations of the offshore wind turbines. Lackner and Rotea (2011) [7] also examined the control of the floating wind turbines vibrations. Later in 2011, Stewart and Lackner studied the effect of dynamic stimuli on the active control of the offshore wind turbines [8]. These studies have examined a variety of tuned dampers, including the tuned mass damper (TMD), the tuned liquid dampers (TLD), the tuned liquid column dampers (TLCD) and the active mass dampers (AMD) for two types of single-pile and floating wind turbines. Since, among the marine conditions, the load caused by the wave have a higher-lasting o effect on the marine structures, the offshore wind turbines were controlled under the simultaneous stimulations of wave and wind in the latest research by the TLCGD damper and its vibrations decreased [9]. Then, the effect of this damper on the reduction of forces caused by the earthquake was evaluated in the offshore wind turbine with the template support platform [10]. However, two recent studies have shown that the TLCGD damper parameters should be properly optimized for this structure given the complex dynamic conditions of the offshore wind turbine, especially due to the wind turbulence that cannot be equated with sine stimulation and the effects of gust, wind cutting, and turbulence as well as the pitch controlling and the stall dynamic system of the turbine should be considered. In other words, it should be possible to estimate the reduction rate of responses during the presence of the damper with the changes in the main parameters of the damper. Therefore, since it was found in the research that no regular process and definite relationship can be achieved for this issue, in this research, we used the artificial neural networks method to estimate the reduction rate in the response rate of the offshore wind turbine in case of employing the TLCGD damper with changes in its main parameters. We used an offshore wind turbine with three different supporting platforms at different depths of the sea instead of a one- degree of freedom structure in this paper to reduce the uncertainties in the optimal parameter relationships. Also, a set of s simultaneous combination of wind and wave loads was used to find these parameters. By applying the above, these conditions can be brought into reality as much as possible so that the outputs would be more reliable.

2. Governing Equations of OWT with TLCGD

Energy absorbers reduce the response of the structure under dynamic loads by absorbing some of the energy input to the structure. The above explanation is based on energy, although it can also be explained based on force. The energy absorbers have a vibrational mass called the secondary mass. The secondary mass applies force to the main structure with its vibration. If the energy absorber frequency is tuned (set), this force acts in a way to reduce the response of the original structure. Simply put, when the main structure moves to the right, this force enters the main structure in the left direction, and vice versa, when the main structure moves to the left, the power is applied to the right. The above force is the result of two forces: The force resulting from the total inertia of the TLCGD due to the absolute acceleration of the structure (the acceleration of a point of the structure where the TLCGD is installed) and the force generated by the inertia of fluid movement inside the horizontal column of the TLCGD. It should be noted that in the case of the second force, only the motion of the fluid in the horizontal column is raised as the movement of fluid in the vertical columns causes the applied vertical forces, which do not affect the lateral response of the structure. If the first force is represented by F_1 and the second force with F_2, we would have:

$$F_1 = m_f \ddot{x} \quad , \quad F_2 = \rho B A_b \lambda \ddot{y} = \rho B A_h \ddot{y} \tag{1}$$

It's worth noting that in the above equation, only F_2 reduces the response of the main structure and F_1 actually raises the responses since the force F_1 in the direction of the inertia force of the main structure but the force F_2 is in the opposite direction. However, the values of these two forces are such that their outcome leads to reduced responses. In other words, the absolute value of F_2 is greater than the absolute value of F_1 (in the circumstance that the damper parameters are optimal). With the algebraic summation of the two above-mentioned forces, the force applied by the TLCGD to the structure is obtained as follows.

$$F = m_f(\ddot{x} + \bar{k}\ddot{y}) \quad , \quad \bar{k} = \frac{B}{2h + B/\lambda} \tag{2}$$

In the above equation, the fluid weight inside the TLCGD is shown with mf, x also represents the local displacement of the structure where the TLCGD is located and the above force is applied at the same point to the main structure. It should be noted that the mass of the TLCGD pipes is usually ignored or their mass is considered in the mass of the main structure. Also, the equation of the fluid flow (movement) in the damper, based on which, the acceleration values of the fluid are obtained in the horizontal $\ddot{x}$ and vertical $\ddot{y}$ columns to be used in Eq. (2), is described in details in [8].

In the end, the motion equation of the multi-degree system of the offshore wind turbine along with the damper can be written in the form of a matrix as follows.

$$[M]\{\ddot{u}\} + [C]\{\dot{u}\} + [K]\{u\} = [F]_{Aero} + [F]_{Hydro} + [F]_{Tlcgd} \tag{3}$$

Wherein: [M]: Structure mass matrix; [C]: The structure intrinsic damping matrix considered as such due to the Cauchy damping factor so that the damping ratio in all modes would be equal to 2%. The complete details of the Cauchy damping method are presented by Chopra (1995) [11]. [K]: Structure hardness matrix; {u}, {u˙}, {u¨}: Vectors of displacement, velocity, and acceleration of the structure response; $[F]_{Aero}$: The vector of aerodynamic forces (These forces are calculated by the FAST program [12] and only enter the turbine system section and are equal to zero on the support platform); $[F]_{Hydro}$: The vector of hydrodynamic forces (These forces are calculated using the modified Morrison equation [13] only enter the turbine system section and are equal to zero on the support platform); $[F]_{Tlcgd}$: The vector of the TLCGD force (This force is calculated using equation 2 and only applies to the NACELLE turbine level and is zero at other levels of the system [14])

It should be noted that due to the use of the centralized mass model and considering that the mass of each level is concentrated in only one point, then, the number of degrees of freedom of the system is the same as the number of the levels considered.

3. Simulation of the OWT -TLCGD in the Simulink

Simulink is a simulation tool equipped with MATLAB software. Simulink has general applications and is not limited to any particular uses like many other engineering simulation software. Using the Simulink, we can dynamically analyze the behavior of a system without the need to build it and only by having the mathematical relations governing that system by saving time and cost [15]. In the present paper, we used this tool for modeling and analysis due to the large volume of computations as well as the interaction and coupling equation between the structure, and damper, and aerodynamic and hydrodynamic loads.

There are two ways to model damper in the Simulink:

1. Considering the location of the TLCGD as a separate alignment (level); In case of using this method, the matrices of mass, stiffness, and damping of the structure will change in the non-TLCGD state.
2. Applying the corresponding TLCGD force into its location; in case of using this method, the structure and TLCGD can be analyzed with their own specifications separately and without any changes.

In this paper, the second method was used for simulation in the Simulink. To use this method, the multiple-degrees of freedom structure is stimulated by a single stage of loading. Therefore, for an n-degrees of freedom structure, we will have:

$$[M]_{n\times n}\{\ddot{u}\}+[c]_{n\times n}\{\dot{u}\}+[k]_{n\times n}\{u\}=\begin{Bmatrix}F_1\\F_2\\\vdots\\F_n\end{Bmatrix}_{n\times 1} \tag{4}$$

Hence, the acceleration at the point of the structure where the TLCGD is placed (usually the highest level of structure) will be obtained. Therefore, the TLCGD is analyzed as a one-degree of freedom system with an absolute acceleration, which is the result of the earthquake acceleration and the acceleration of the level where the TLCGD is placed. The corresponding TLCGD force will be obtained by multiplying the TLCGD mass by its absolute acceleration, which can be applied to the structure at the level where the TLCGD is placed. By applying the force corresponding to the TLCGD to the n-th level of the structure, in Eq. (4), the force term is changed as follows:

$$\begin{Bmatrix}F_1\\F_2\\\vdots\\F_n+F_{TLCGD}\end{Bmatrix}_{n\times 1} \tag{5}$$

According to the description and equations presented above, the block designed in the Simulink for a wind turbine equipped with a TLCGD damper is obtained as shown in Fig. 1. It should be noted that the model is analyzed once as shown below to examine the performance of the damper in reducing vibrations for each load combination applied to the system. Once again, the other model is analyzed by cutting off the damper force path in the Simulink to perform a comparison between the mode with and without the damper.

The numerical algorithm which is used in Simulink model, is Runge–Kutta method. In numerical analysis, the Runge–Kutta methods are a family of implicit and explicit iterative methods, which include the well-known routine called the Euler Method, used in temporal discretization for the approximate solutions of ordinary differential equations.

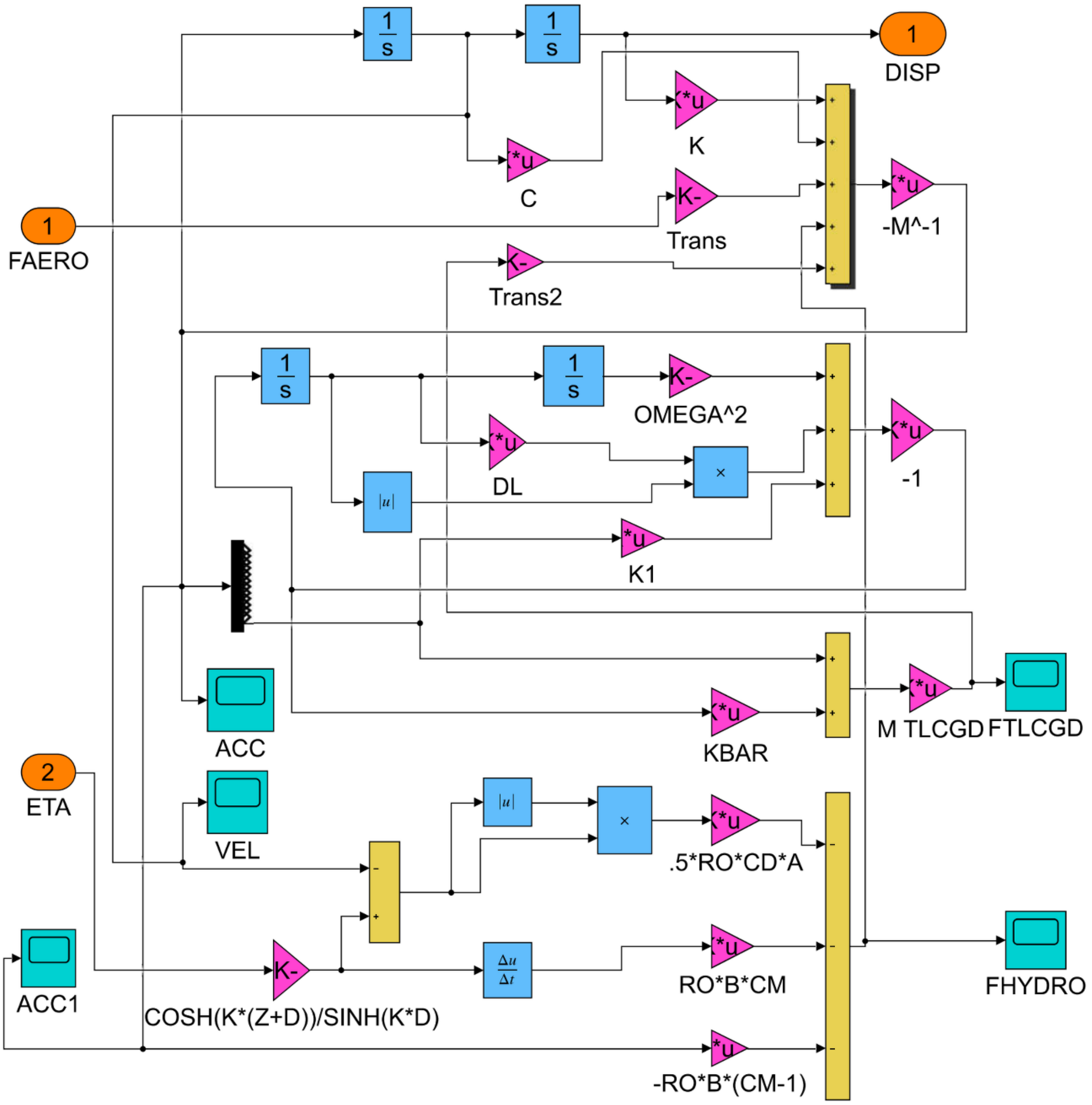

Figure 1. The block designed in the Simulink for an offshore wind turbine equipped with TLCGD

4. Artificial neural network

By observing biological systems and natural systems, the scientists provide some descriptions for them. These mathematical descriptions were then converted into a series of computational blocks. These blocks emerged in the form of neural networks, genetic algorithms, particle swarm algorithms, etc., which are called computational intelligence. The most important feature of these algorithms is to inspire from nature since the nature has chosen almost the best possible solution due to having sufficient time [16].

The artificial neural network, which is a data processing system, has been designed and introduced with inspiring from the human brain in pursuit of faster processing and solving the problems. In the neural networks, data processing is handled by small processors working together in an interconnected and parallel network. The benefits of this artificial network include the high speed and responding as well as the ability to answer unanswered questions based on experience and training. In other words, with more data used to train the neural network, the neural network will be trained more accurately and will experience less error when producing output [16].

Flood and kartam raised the use of artificial networks in civil engineering for the first time. In their paper, they used the popular form of the supervised progressive neural network. In this article, a graphical interpretation of the neural network was introduced for the first time. In fact, the purpose of this paper was to ensure the development of this technology in the civil engineering [17].

In those years, the artificial neural network was developed in areas such as optimization process, seismic hazard prediction, classification of non-destructive evaluation signals, structural value estimation, etc. In recent years, the use of artificial neural networks and the optimization algorithms have drawn much attention in controlling the vibrations. In this regard, Leung et al. (2008) obtained the optimal TMD frequency and damping ratio for a one-degree of freedom structure under the non-fixed basic vibration using the Particle Swarm Fractional Algorithm (PSO) [18]. In another study in 2009, Leung and Zhang used the PSO algorithm to obtain the optimal parameters for a one-degree of freedom structure under external loading and basic vibration modeled with the white Gaussian noise and provided formulas for these values [19]. Also, in 2011, Bekdas and Nigdeli used the Harmony Search (HS) algorithm to find optimal TMD parameters for a 10-story structure under the harmonic basic acceleration [20]. Moreover, in 2019 ANN was used for prediction the wave set-up in Iranian coasts [21].

4.1. Neural network data

In this paper, it will be used the modeling and approximation feature of the neural network functions to estimate the reduction percentage of the response of an offshore wind turbine with TLCGD. This system is under different wave and wind excitations. Finally, frequency and mass of the TLCGD are optimized.

Three offshore wind turbines simulated in the Simulink were placed under simultaneous stimulations caused by wind and wave. To this end, 75 different loadings of wave and wind applied to the offshore wind turbines were used to optimize these parameters as follows.

Table 1. Specifications of simultaneous wind and wave loadings

Parameters	Range
u_{wind} (Average Wind Speed)	$8\frac{m}{s}\xleftrightarrow{2\ Spaced}24\frac{m}{s}$
H_{wave} (Significant Wave Height)	$2m\xleftrightarrow{2\ Spaced}10m$
$T_{p_{wave}}$ (Peak Wave Period)	$8s\xleftrightarrow{4\ Spaced}16s$

The optimization index is the reduction rate of the mean SD (standard deviation) of the structure response displacement at the level of damper placement for 75 different loadings compared to the absence of damper case. To increase the number of data for artificial neural network training as well as reducing the uncertainties, three values of 2%, 4%, and 8% were considered for the ratio of the mass of the damper to the mass of the structure (μ) and three values of 0.6, 0.7, and 0.9 for the ratio of the damper frequency to the frequency of the structure (α).

The data in the neural network is divided into three categories:

1. Training data
2. Validation data
3. Testing data

A total of 2025 data were used to train the neural network. The information was provided based on the outputs of three offshore wind turbines under 75 combinations of loading, which were obtained for the ratios of different masses and frequencies. Of this information, 70% was the share of training data, 15% of the validation data, and 15% of the experimental data share.

The neural network takes a part of the data as questions and answers and teaches the neurons accordingly. Then, during the training, it provides the neurons some of the data unanswered to test the training process and uses a portion of the data in the end for the final test, which is not used in the training and validation processes. The similarity of validation data and experimental data is that for both, the data is given to the neurons unanswered. But the major difference between them is that the validation data is used during the training process to prevent data memorizing by neurons, while the test data is used at the end of the training process to evaluate the system's performance. The following parameters were used as inputs to train the neurons:

- The frequency of the first mode of the offshore wind turbine
- The ratio of the TLCGD mass to the structure mass ($\mu=\frac{m_{tlcgd}}{M_{structure}}$)
- The ratio of the TLCGD frequency to the structure frequency ($\alpha=\frac{\omega_{tlcgd}}{\omega_{structure}}$)

Since the inputs are not of the same type, all the inputs and outputs data were normalized to better assess the performance of the neural network. Also, with trial and error process to get the best answer, finally, three hidden layers were used with each containing 10 neurons and the one output layer was considered. It should be noted that, as shown in Fig. 2, the number of output layers is always equal to the number of outputs of the neural network. The output of the neural network is the percentage of reduction of the structure response in the mode with the damper compared to the mode without the damper. Thus, the user receives the performance rate of the TLCGD in reducing the structure response as output by entering some specifications of the offshore wind turbine and the TLCGD damper installed in it such as the frequency of the structure, the ratio of the damper mass and the ratio of the damper frequency. In other words, this process leads to the optimal design of this damper for a variety of wind turbines with different frequencies. Since if, for example, the percentage of reduction in the structure response, which is the output of the neural network, becomes negative or reduces, it means that the two main parameters of TLCGD, (μ) and (α), are not properly selected. It implies that the damper function has been destructive or has not functioned properly.

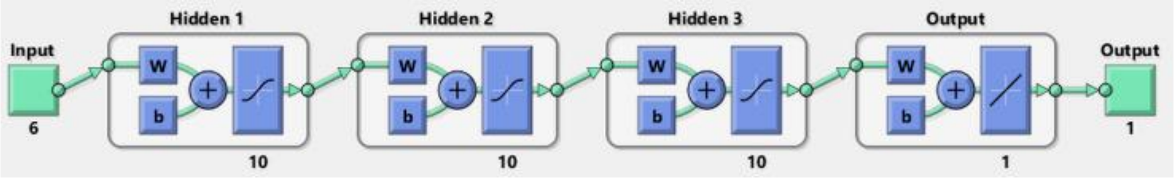

Figure 2. Specifications of the artificial neural network input and output layers

4.2. The results of artificial neural network

Using the artificial neural network, the system could train the neurons well after about 12 iterations. As shown in Fig. 3, aimed at reducing the mean square, the system has well reduced the square errors in the training, validation and testing data.

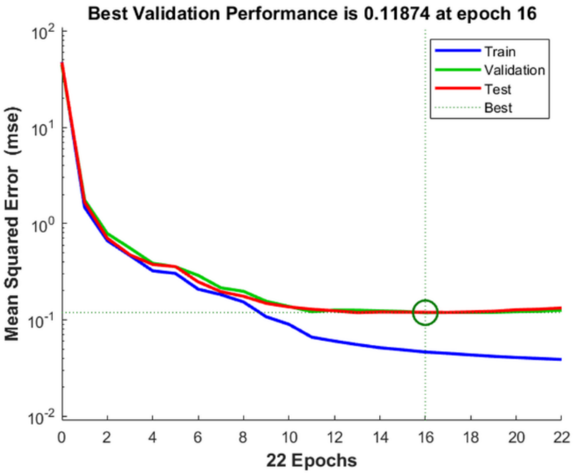

Figure 3. The trial and error process of the neural network for training the neurons

This network is designed in such a way that in the absence of improvement up to six consecutive stages in the neural network training process, the algorithm will stop and the best answer to that stage will be identified. According to Fig. 4, a little improvement is seen in epoch 12 compared to epoch 11; but, after repeat 12, there are three stages of failure to improve compared to step 12. However, at the end of step 16, the system will perform better than the previous steps; and then, the 6 non-improvement steps will stop the training algorithm. Finally, the sixteenth epoch is selected as the best performance. In Fig. 4, mu is the control parameter for the algorithm used to train the neural network. Choice of mu directly affect the error convergence.

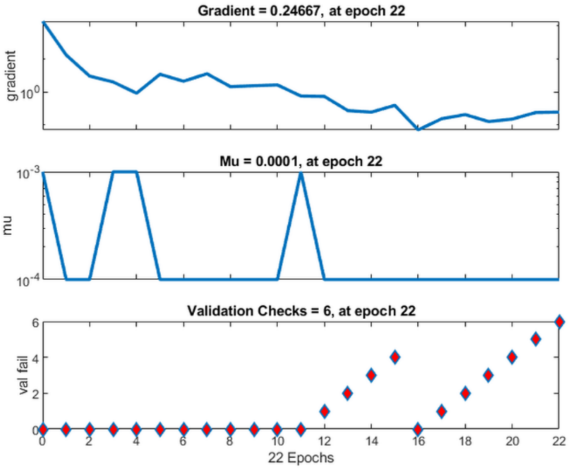

Figure 4. The improvement steps of neural network training

By training the neural network, the target values and the output of the neural network are compared as follows.

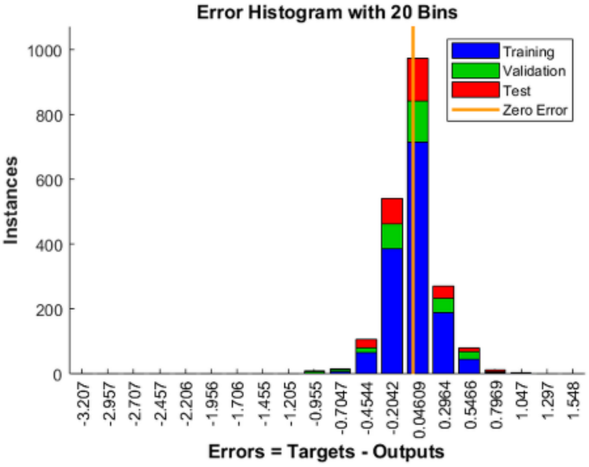

Figure 5. Error Histogram Diagram

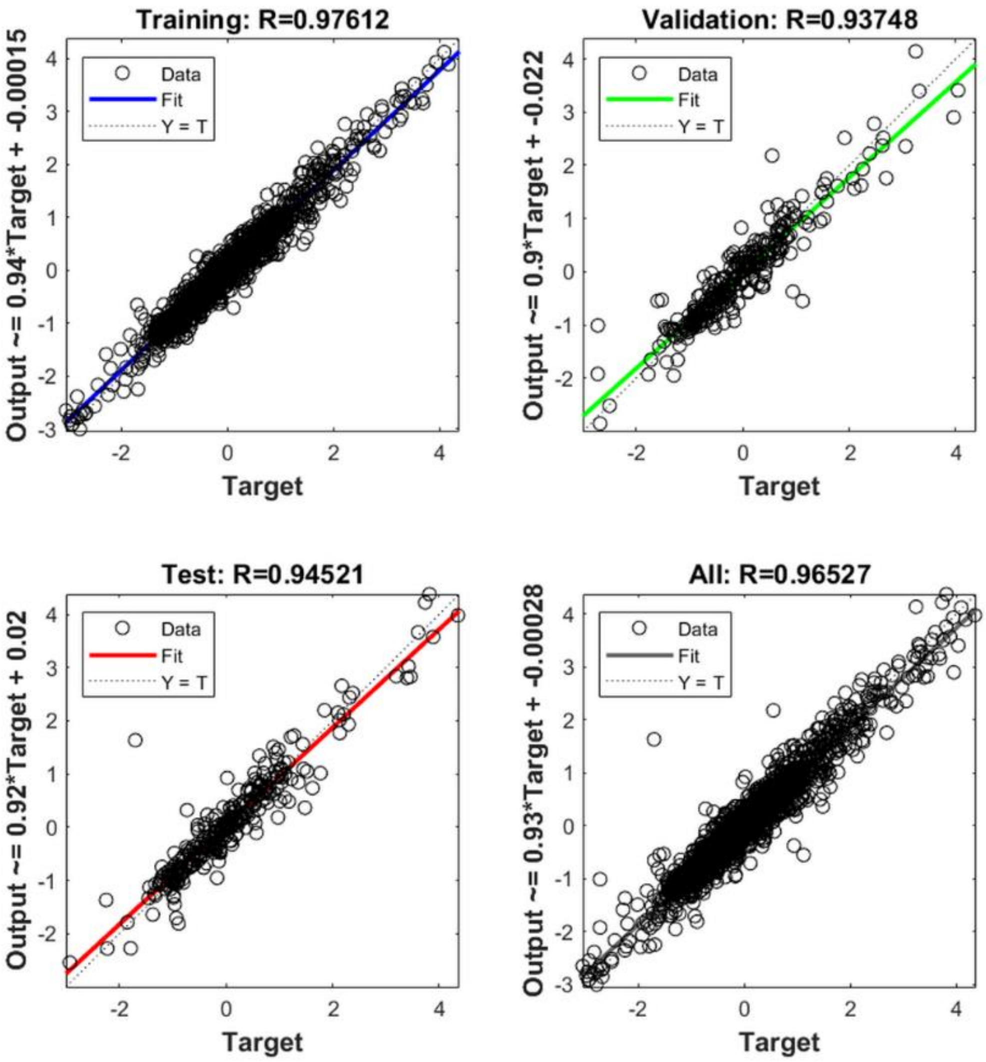

Figure 6. Comparing the correlation between the values of the reduction percentage of the actual response and the values obtained from the neural network

5. The use of ANN to optimize TLCGD performance in OWT

In this section, to control the results obtained by the artificial neural network, an offshore wind turbine associated with a TLCGD damper with the characteristics shown in Fig. 7 were was put under 75 combinations of load in the previous section; then, the results obtained from Simulink were compared with the results of the neural network. It should be noted that the TLCGD specifications in this section were not used in the neural network training. In other words, the ratio of the mass and the ratio of the current damper are not included in the ratios that were given in the previous section as input to the neural network system. In Fig. 7 the gas is located in the vertical column and on the liquid.

TLCGD is rigidly connected to the primary structure and the relative displacement of the primary structure and the secondary structure is zero. So the stroke which is due to the relative displacement of the TMD to the original structure is not the case in the TLCGD. However, in this damper the similar parameter to the stroke of the TMD, is the displacement of the fluid in the vertical column. Therefore, in this research, the height of the fluid in the vertical column is considered to be 1.5 m before the structural vibration. System analysis under wind and wave excitations showed that the maximum amplitude of displacement of the liquid in the vertical column is about 30 cm. Therefore, in designing the damper, it should be noted that the minimum total height of the vertical column of the damper is about 1.80 meters.

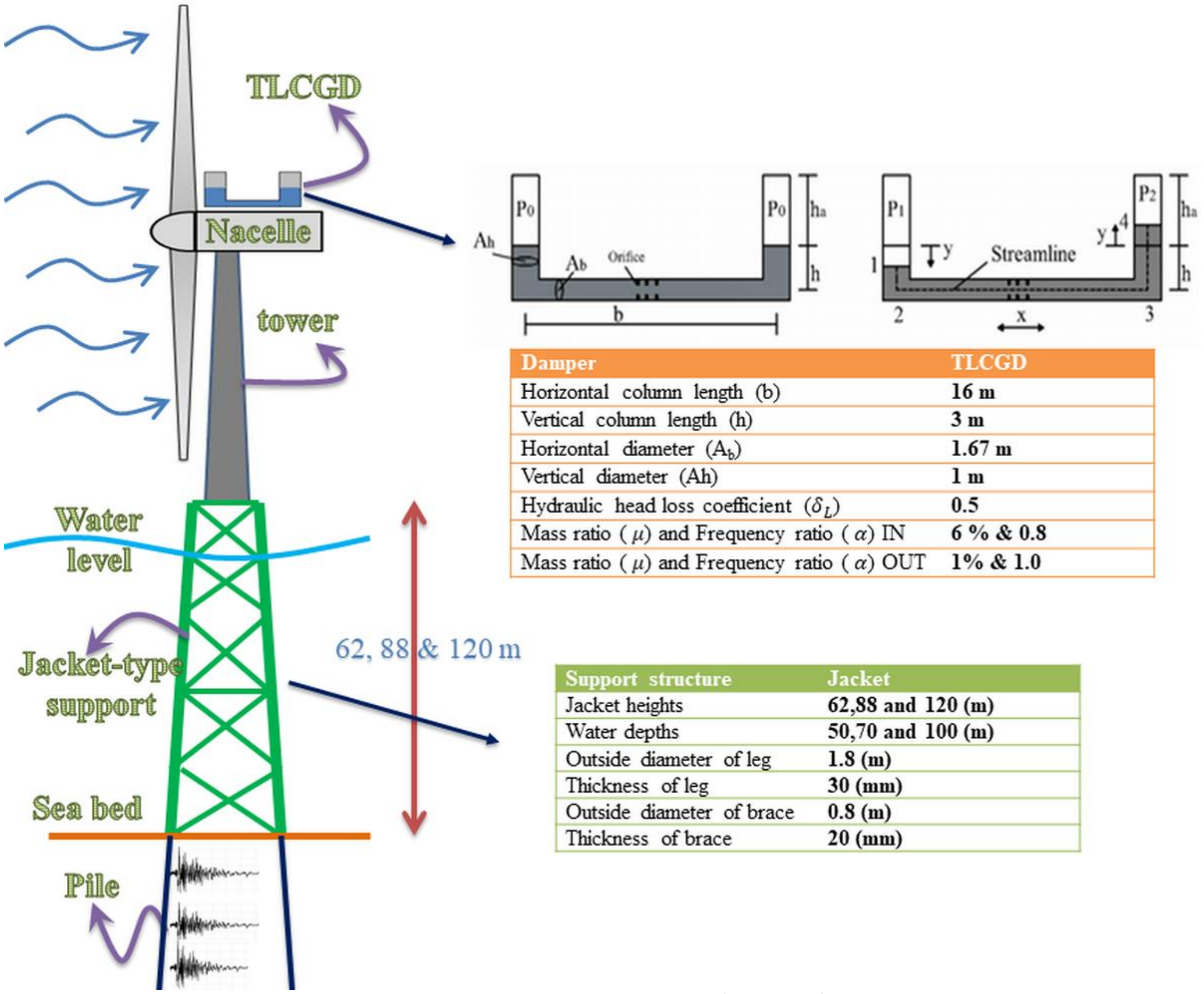

Damper	TLCGD
Horizontal column length (b)	16 m
Vertical column length (h)	3 m
Horizontal diameter (A_b)	1.67 m
Vertical diameter (Ah)	1 m
Hydraulic head loss coefficient (δ_L)	0.5
Mass ratio (μ) and Frequency ratio (α) IN	6 % & 0.8
Mass ratio (μ) and Frequency ratio (α) OUT	1% & 1.0

Support structure	Jacket
Jacket heights	62,88 and 120 (m)
Water depths	50,70 and 100 (m)
Outside diameter of leg	1.8 (m)
Thickness of leg	30 (mm)
Outside diameter of brace	0.8 (m)
Thickness of brace	20 (mm)

Figure 7. The structure characteristics to control the function of the neural network

As seen in the figure above, new inputs (the damper to structure mass ratio and the damper to structure frequency ratio) have been applied in two different types to examine and control the neural network trained in the previous section. Thus, one of them is within the range of the network training inputs (IN) and the other is outside the range of data used as inputs for training the neural network (OUT). This was done to evaluate the performance of the artificial neural network not only for the known data but also for the data outside the network range and make a comparison between its results and the actual results.

To investigate the function of the neural network, the reduction rate in the response of the structure along with the damper obtained from the neural network, which has been under the influence of 75 different loadings for three different types of turbines (in different depths of water) were compared with the actual results obtained from the Simulink model. In Figure 8, this comparison can be seen for 75 different load combinations.

The structure of the offshore wind turbine is in interaction with the soil that can affect its behavior. This effect increases or decreases in the period of the structure. Therefore, since the purpose of the paper is parametric studies, rather than a case study, different types of OWTs with different periods are considered to evaluation the effects of different types of soil which interaction with structure.

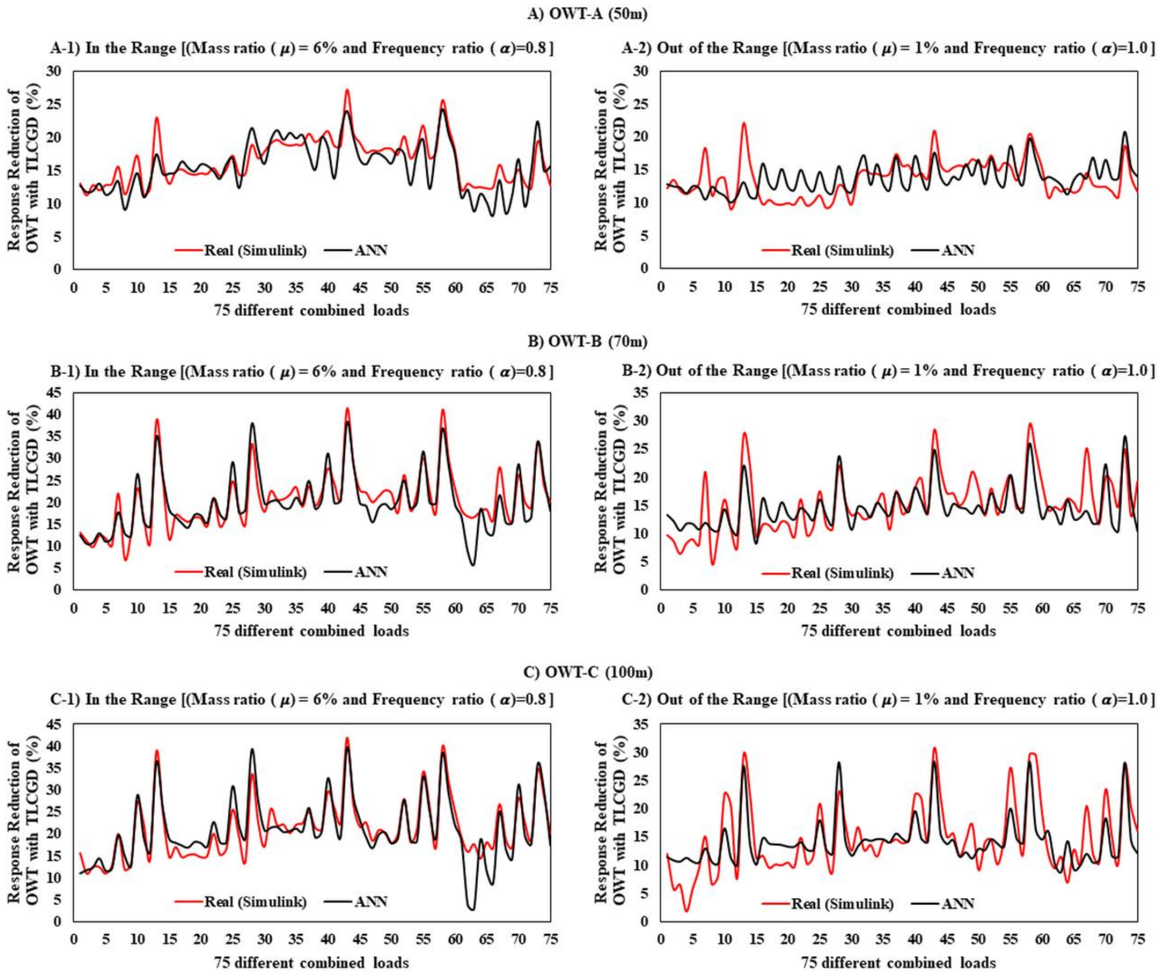

Figure 8. Comparison of the actual percentage reduction of the structure response with the damper with the percentage obtained from the neural network for 75 load combinations of different simultaneous wind and wave

Also, for a better understanding, the mean, standard deviation and the effective value (RMS (root mean square)) of Figure 8 diagrams are presented for two types of parameters inside and outside the neural network training range in Tables 2 and 3 to determine the error percentage of the neural network results compared to the actual results.

Table 2. Comparison of actual results (Simulink output) and artificial neural network for the state within the training range

IN [(Mass ratio (μ) = 6% and Frequency ratio (α)=0.8]									
	Mean of response reduction(%)			St. Dev. of response reduction(%)			RMS of response reduction(%)		
Type of Structure	Real (Simulink)	ANN	Error	Real (Simulink)	ANN	Error	Real (Simulink)	ANN	Error
OWT-A (50m)	16.37	15.68	4.21	3.42	3.71	8.57	16.72	16.11	3.65
OWT-B (70m)	20.53	19.95	2.82	6.76	6.77	0.11	21.60	21.06	2.53
OWT-C (100m)	21.07	20.80	1.29	6.81	7.47	9.70	22.13	22.09	0.21

Table 3. Comparison of actual results (Simulink output) and artificial neural network for the off-range training

OUT [(Mass ratio (μ) = 1% and Frequency ratio (α)=1.0]									
	Mean of response reduction(%)			St. Dev. of response reduction(%)			RMS of response reduction(%)		
Type of Structure	Real (Simulink)	ANN	Error	Real (Simulink)	ANN	Error	Real (Simulink)	ANN	Error
OWT-A (50m)	13.56	13.73	1.19	2.8702	2.2231	22.55	13.86	13.90	0.30
OWT-B (70m)	15.34	14.52	5.37	5.1519	3.6678	28.81	16.17	14.97	7.45
OWT-C (100m)	14.71	14.24	3.25	6.3003	4.3601	30.80	15.99	14.88	6.94

According to the above tables and Fig. 9, we realize that the proposed neural network has yielded very favorable results for a new input within the range of the training input parameters. Thus, the mean error percentage, the standard deviation and the effective value of the neural network with actual values are below 10% for all three types of the structure. But the results are associated with more errors for a new input outside the range of input parameters of the training of the neural network. However, these error values are still below the 10% in case of average percentage error rate and the effective value; but, the mean percentage error related to the standard deviation is about 20 to 30 percent. The noteworthy point here is that the selected input outside the training range has a damper to structure frequency ratio of 1 associated with the resonance phenomenon. Therefore, one can see that the neural network, despite the fact that it does not know the cause of the phenomena occurred, provides acceptable results even in the presence of an unusual phenomenon.

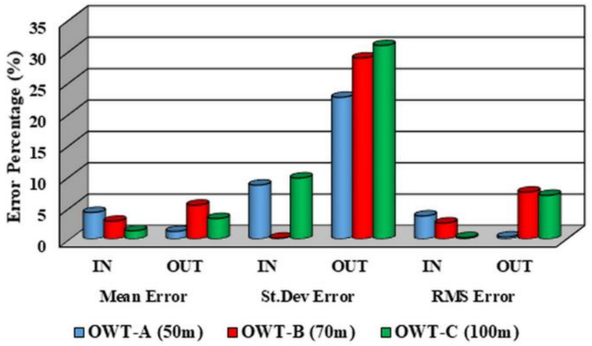

Figure 9. The percentage error rate of the artificial neural network method compared to the actual results obtained from Simulink

6. Conclusions

In this paper, we tried to provide a new method based on artificial neural network for examining the optimal TLCGD damper parameters for an offshore wind turbine under the provocations of wave and wind. By considering offshore wind turbines at different depths and combining different simultaneous wind and wave loads, the uncertainties were reduced in obtaining the optimal parameters. As the forces applied to the offshore wind turbine caused by the wave and the wind (especially the wind due to the PITCH control system inside its rotor) have their own intricacies that the regular trend governing the behavior of this type of structure along with the damper cannot easily be determined, the results showed that the neural network was able to somehow detect this behavior and predict the reduction rate of the structure response in the presence of damper according to this model. This will determine the optimal TLCGD parameters for use in different types of offshore wind turbines with different depths and periods. In fact, the importance of using this template is revealed based on the fact that in defining an analytical or empirical relationship, the impact of some factors has not yet been identified or has been simplified due to the complexity of the behavior. However, by using the neural network, without the need for a complete understanding of the parameters affecting the TLCGD behavior in an offshore wind turbine, these factors are considered indirectly in the prediction of the damper behavior. In this study, to control the accuracy of the neural network performance, two new input categories, including two main parameters of the damper, namely the mass ratio and the frequency ratio, were given to the neural network so that the results can be compared with the actual results of the structure analysis in the Simulink model. These new values were chosen in such a way that, firstly, there will be no recurrent input with the training data of the neural network. Secondly, a bunch of these inputs was outside the range of the neural network training. The results indicated that the neural network has an acceptable error rate compared to the actual results in both categories of inputs. However, this error rate was higher for the category beyond the scope of training, which is normal. Therefore, the method presented in this study can be used practically to determine the optimal parameters of the TLCGD, which will lead to a good design for its use in the offshore wind turbines.

Acknowledgment

The author acknowledges the funding support of Babol Noshirvani University of Technology through Grant program No. BNUT/394097/98.

7. References

[1] Zhang, P., & Huang, S. (2011). Review of aeroelasticity for wind turbine: current status, research focus and future perspectives. *Frontiers in Energy*, *5*(4), 419-434.

[2] Ogunjuyigbe, A. S. O., Ayodele, T. R., & Bamgboje, O. D. (2017). Optimal placement of wind turbines within a wind farm considering multi-directional wind speed using two-stage genetic algorithm. *Frontiers in Energy*, 1-16.

[3] IEC, I. (2009). 61400-3, Wind Turbines-Part 3: Design Requirements for Offshore Wind Turbines. *International Electrotechnical Commission, Geneva*.

[4] Iemura, H., & Pradono, M. H. (2002). Passive and semi- active seismic response control of a cable-stayed bridge. *Journal of Structural Control*, *9*(3), 189-204.

[5] Dezvareh, R. (2019). Upgrading the Seismic Capacity of Pile-Supported Wharfs Using Semi-Active Liquid Column Gas Damper. *Journal of Applied and Computational Mechanics*.

[6] Lackner, M. A., & Rotea, M. A. (2011). Passive structural control of offshore wind turbines. *Wind energy*, *14*(3), 373-388.

[7] Lackner, M. A., & Rotea, M. A. (2011). Structural control of floating wind turbines. *Mechatronics*, *21*(4), 704-719.

[8] Stewart, G. M., & Lackner, M. A. (2011). The effect of actuator dynamics on active structural control of offshore wind turbines. *Engineering Structures*, *33*(5), 1807-1816.

[9] Dezvareh, R., Bargi, K., & Mousavi, S. A. (2016). Control of wind/wave-induced vibrations of jacket-type offshore wind turbines through tuned liquid column gas dampers. *Structure and Infrastructure Engineering*, *12*(3), 312-326.

[10] Bargi, K., Dezvareh, R., & Mousavi, S. A. (2016). Contribution of tuned liquid column gas dampers to the performance of offshore wind turbines under wind, wave, and seismic excitations. *Earthquake Engineering and Engineering Vibration*, *15*(3), 551-561.

[11] Chopra, A. K., & Chopra, A. K. (1995). *Dynamics of structures: theory and applications to earthquake engineering* (Vol. 2). Englewood Cliffs, NJ: Prentice Hall.

[12] Jonkman, J. M., & Buhl Jr, M. L. (2005). FAST user's guide. *National Renewable Energy Laboratory, Golden, CO, Technical Report No. NREL/EL-500-38230*.

[13] Laya, E. J., Connor, J. J., & Sunder, S. S. (1984). Hydrodynamic forces on flexible offshore structures. *Journal of engineering mechanics*, *110*(3), 433-448.

[14] Dezvareh, R. (2019). Evaluation of turbulence on the dynamics of monopile offshore wind turbine under the wave and wind excitations. *Journal of Applied and Computational Mechanics*.

[15] MATLAB, (2008). *User Guide, Simulink*, MathWorks Inc., Version 7.6.0.

[16] Haykin, S. (1994). *Neural networks* (Vol. 2). New York: Prentice hall.

[17] Flood, I., & Kartam, N. (1994). Neural networks in civil engineering. I: Principles and understanding. *Journal of computing in civil engineering*, *8*(2), 131-148.

[18] Leung, A. Y., Zhang, H., Cheng, C. C., & Lee, Y. Y. (2008). Particle swarm optimization of TMD by non- stationary base excitation during earthquake. *Earthquake Engineering & Structural Dynamics*, *37*(9), 1223-1246.

[19] Leung, A. Y. T., & Zhang, H. (2009). Particle swarm optimization of tuned mass dampers. *Engineering Structures*, *31*(3), 715-728.

[20] Bekdaş, G., & Nigdeli, S. M. (2011). Estimating optimum parameters of tuned mass dampers using harmony search. *Engineering Structures*, *33*(9), 2716-2723.

[21] Dezvareh, R. (2019). Providing a new approach for estimation of wave set-up in Iran coasts. *RESEARCH IN MARINE SCIENCES*, *4*(1), 438-448.

[22] Dezvareh, R., Bargi, K., & Moradi, Y. (2012). Assessment of Wave Diffraction behind the Breakwater Using Mild Slope and Boussinesq Theories. *International Journal of Computer Applications in Engineering Sciences*, *2*(2).